UCLA
UCLA Electronic Theses and Dissertations

Title
In vivo terahertz imaging of tissue edema for burn wound and flap assessment

Permalink
https://escholarship.org/uc/item/4fm2m9rt

Author
Bajwa, Neha

Publication Date
2016

Peer reviewed|Thesis/dissertation

eScholarship.org Powered by the California Digital Library
University of California

UNIVERSITY OF CALIFORNIA

Los Angeles

In vivo terahertz imaging of tissue edema for burn wound and flap assessment

A dissertation submitted in partial satisfaction of

the requirements for the degree Doctor of Philosophy

in Biomedical Engineering

by

Neha Bajwa

2016

© Copyright by

Neha Bajwa

2016

ABSTRACT OF THE DISSERTATION

In vivo terahertz imaging of tissue edema for burn wound and flap assessment

by

Neha Bajwa

Doctor of Philosophy in Biomedical Engineering
University of California, Los Angeles, 2016
Professor Warren Grundfest, Chair

Edema, or tissue swelling, is a characteristic component of the tissue response to cutaneous injury and, therefore, a potentially useful diagnostic target for assessing wound severity and viability *in vivo*. Currently, there is no widely available pre-clinical or clinical technique that can identify the extent and distribution of tissue water content (TWC), the primary indicator of edema, early and accurately. We have previously shown that reflective terahertz (THz) imaging can rapidly and non-invasively generate native, pathology-specific contrast in superficial tissue based on hypothesized variations in TWC. TWC-based contrast and the sensing depth of THz imaging, however, have yet to be verified with a well-established TWC-sensing technique. Moreover, early and repeatable visualization of TWC in pre-clinical wound models may further support THz imaging as an emerging diagnostic tool in patients sustaining severe burns, surgical trauma, or other conditions leading to tissue edema.

This work details the iterative development, characterization, and pre-clinical testing of THz TWC imaging in phantom, *ex vivo,* and *in vivo* wound models for early wound and tissue viability assessment. First, the sensitivity of a novel, reflective THz system to variation in water concentration was calibrated through the use of gelatin phantoms for quantitative comparison of

THz imagery of targets. Second, the ability of reflective THz imaging to track TWC changes was correlated with depth-resolved magnetic resonance imaging (MRI) in both an *ex vivo* porcine burn model and *in vivo,* burn-induced model of edema in rats. This work offers the first *in vivo* correlative assessment of mobile TWC as a major contributor to THz imaging contrast. Third, improved THz imaging methodologies were developed and implemented *in vivo* to acquire reproducible THz-TWC maps of burn wounds and interpret these results in the context of burn edema pathophysiology. These advancements included 1) an image registration method to reliably compare THz-TWC measurements with histological wound outcome; 2) a reproducible contact-burn induction technique; and 3) the use of multiple dielectric windows. Finally, the first *in vivo* pilot study was performed to investigate the utility of reflective THz TWC imaging for early assessment of tissue flap viability, the most significant determinant of tissue survival in reconstructive surgery. Collectively, these results demonstrate important implications of THz imaging in edema monitoring of wounds and skin evaluation and the potential use of this technology as an augmentation to the standard clinical assessment of superficial tissue.

The dissertation of Neha Bajwa is approved.

Zachary D. Taylor

Daniel B. Ennis

Dan Ruan

Maie A. St. John

Albert Thomas

Warren S. Grundfest, Committee Chair

University of California, Los Angeles

2016

This dissertation is dedicated to my loving parents and younger brother, Herman. Your unwavering support and encouragement made this work possible. Thank you for believing in me.

TABLE OF CONTENTS

LIST OF FIGURES

LIST OF TABLES

LIST OF ACRONYMS

7T – 7 Telsa

B – Basal layer

BCC – Basal cell carcinoma

CW – Continuous wave

ε - Permittivity constant

EFL – Effective focal length

FA - Flip angle

FOV – Field of view

LDI – Laser Doppler imaging

GR – Stratum granulosum

MRI – Magnetic resonance imaging

n – Refractive index

N(h) – proton density

OAP – Off axis parabolic mirror

PCS – Photoconductive switch

SC – Stratum corneum

SD - Standard deviation

SS – Step size

SNR- Signal-to-noise ratio

T_2- transverse proton relaxation time

T_2w MSME- T2-weigthed multislice multiecho

T_E – echo time

T_R – relaxation time

TEWL – Transepidermal water loss

THz – Terahertz

TWC – Tissue water content

ZBSD – Zero Bias Shottkey detector

ACKNOWLEDGEMENTS

Like most PhD efforts, mine was a collaborative one. Several people, including friends, family, and colleagues, were instrumental to both my personal and professional development during the process. Their unwavering support, guidance, and mentorship helped push both me and my work across the finish line. For this, I will forever be grateful.

Foremost, I would like to thank my family for allowing me to realize my full academic potential. And, of course, for refueling, sheltering, and unconditionally loving me during these memorable six years. Amidst all my successes and failures, their single-most concern was, and continues to remain, my happiness. They truly are the greatest gift in my life.

Next, my sincerest gratitude goes to my primary academic advisor, Dr. Warren Grundfest, for placing his confidence in me to lead a project that is so close to heart. His mentorship, advice, and encouragement gave me the footing I needed to take on research questions and tasks that were often outside the scope of my field. From him, I have learned so much about the big picture aspects of biomedical research, and how I can best contribute to the growth of this field. He always supported my decisions and gave me space when I most needed it. I am a better researcher and person because of him.

I would like to also thank my committee members for their time, constructive feedback, and unyielding support. These are some of the most reputed faculty members at UCLA and in their field, so it was a such a pleasure to personally work with and learn from them. Dr. Ennis and Dr. St. John, especially, devoted a great deal of their time to re-working and polishing my final publications at the very last minute. Their suggestions really bolstered my work and its dissemination to greater heights.

My deepest appreciation also goes to Dr. Fishbein, without whom I would not have those beautiful histological images and analyses that are so talked-about. He truly is a one-of-a-kind person at UCLA, in that his immense knowledge of pathology is matched, if not surpassed, by his

kindness. Every time I walked out of his office, I felt so fortunate for having the opportunity to know such a person. I hope to one day inspire my colleagues in the same way.

My sanity and overall well-being are largely intact due to the kindness, assistance, and emotional support I received from my fellow graduate students and colleagues. My deepest appreciation goes to Marko K., Chris W., Pria T., Asael P, Adria S., William Y., Nikan N., and David R. I also wish to offer my most heartfelt thanks to the following people:

To Bryan Nowroozi: There were instances when I really wanted to throw in the towel, but your unparalleled leadership, professionalism, and kindness restored my faith in academia and myself. You really are an exceptional role model who has taught me, and so many others, that hard work, confidence, and perseverance can make a career. It was a privilege working with you.

To Alan Priester: You have seen me transform from the naive, young grad student I was into the “rat lady” I have become. More seriously, your rare talent in both research and the arts has been so inspiring to me. I hope one day to also effortlessly balance my extra-curricular and research interests. You are also single-handedly responsible for introducing me to the most cringe worthy and beautiful films. Thank you.

To Ahmad Abiri: Despite CASIT being the windowless cube it is, you always manage to emanate light into the room with your humor. I am usually fixated on the positive results of my research, but you taught me to see good moments in the bad ones too. I will always be thankful for your encouragement and think fondly of our chats under the da Vinci.

To Jim Garritano: You have been key to the way I now think about research. From our friendship and collaboration, I have learned that it is better not to sugar coat feelings about ambiguous results and that “good’ research is methodical. Your help and advice have really shaped the success of my PhD work, and I will forever be grateful.

To Shahzad Patel and Artemio Navarro: Both of you looked out for me like a younger sister during the highs and lows of my early PhD career. Artemio, you constantly taught me that it is possible to move forward even when you are working alone with minimal resources. Your

friendship, advice, and our drives to the VA will always be with me. Shahzad, your ambition, courage, and kindness push me to better myself. Also, you coined the moniker “rat lady,” so I have that to thank you for.

To Meghedi Babakhanlou, my rock: You are the pillar that kept me standing during my PhD. The Armenian sister who I never thought I would meet in this lifetime. You are beautiful, inside-out, and a source of inspiration to women like me in research. I would never have made it to this “oh so sweet” ending without you. I share all my successes with you.

To Ashkan Maccabi (a.k.a. Little One), my sidekick: Yes, of course you get your own section too. You are the salt to my pepper. The Robin to my Batman. I am so grateful to have you in my life as both a friend and a colleague. Your confidence, talent, drive, and humor are such a breath of fresh air in a lab environment that can often get so monotonous and dry. The number of times that you have made me laugh out loud, to the point where people are shutting their doors, is countless. We both have huge egos, yet, somehow, you are the only one that keeps me grounded. I am indebted to you for your encouragement and infinite kindness. You will forever be family, Little One.

To Shijun Sung (a.k.a. Mom), my fellow foodie and co-pilot: Like Ashkan and Meg, you have become a part of the family, whether you like it not. Of all the students I have crossed paths with, I have never met an individual quite like yourself, who regularly uses analogies found only in an episode of South Park. Yet, my friend, you have such a beautiful mind! If I had to give another person credit for the caliber of my work, that person would undoubtedly be you. You have mentally pushed me to limits like no one else has or can. The reason there are 50+ iterations of each of my manuscripts is due to the endless feedback, edits, data analysis, and time that you have selflessly invested in transforming my research into something memorable and great. You continue to surprise me each day, and I wish I could stay longer just to learn more from you. You really do embody everything that a PhD student should aspire to be: inquisitive, hardworking,

methodical, social, kind, and honest. I have and will continue to look up to you. Now, go eat a burger.

Last, but no least, I would like to express my sincerest gratitude to my extraordinary teacher and post-doc, Zachary Taylor. He was brave enough to take a chance on a chatty Indian girl with little to no expertise in anything imaging-related. I am indebted to him for teaching me almost every research skill and THz fact I know. His tutelage, respect, time, and faith in my abilities kept me steadily steered on the "fast track." Even very early on, he unquestionably supported my interest in scientific writing, allowing me to take the lead on NIH grants and soliciting my help on proposals. That kind of encouragement is unprecedented in most PhD programs. He truly is a one-of-a-kind mentor who is as intelligent as he is good. The first and best piece of advice he ever gave me was "to dominate." I plan to do just that.

Funding for the completion of this work was provided by the National Eye Institute Grant R01EY021590 ("Non-contact, THz Sensing of Corneal Hydration") and the National Institute of Biomedical Imaging and Bioengineering Grant R21EB015084 ("*In vivo* THz Imaging of Acute Burn Wounds") and Grant R21EB016896 ("A Correlational Study of THz and MRI hydration mapping in *in vivo* skin burns").

CURRICULUM VITAE

EDUCATION

University of California, Los Angeles, CA **Sep 2009 - Present**
Expected Doctorate of Philosophy, Bioengineering
Concentration: Terahertz (THz) Medical Imaging

University of California, Los Angeles, CA **Sep 2009 - Sep 2011**
Master of Science, Bioengineering
Concentration: THz Medical Imaging

Johns Hopkins University, Baltimore, MD **May 2008**
Bachelor of Science, Biomedical Engineering
Concentration: Cell & Tissue Engineering
Dean's List (Fall 2004, Spring 2005, Spring 2007, Fall 2007, Spring 2008)

Relevant Courses:
Biophysics, Channels & Membranes, Eng. Principles for Drug Delivery, Human Physiology, Physical Chem. of Biomacromolecules, Signals & Systems, Minimally Invasive Surgical Tools, Laser-Tissue Interaction: Biologic Spectroscopy, Energy-Tissue Interactions, Models & Simulations, Dynamical Systems, Immunobiology, Biomaterials I (II), Biomolecular Materials, Microfabrication, and Biocompatibility

EXPERIENCE

Center for Advanced Surgical and Interventional Technologies (CASIT), UCLA, Dept. of Biomedical Engineering and Surgery **Sep 2009 - Present**
Graduate Student Researcher, PhD Candidate

- Leading *in vivo* terahertz (THz) imaging of tissue water content (TWC) for surgical flap assessment. Published the first THz visualization of differences in flap TWC to enable prediction of flap viability status 24 hr prior to clinical assessment.
- Leading *in vivo* validation studies of THz-TWC imaging for burn assessment using companion magnetic resonance imaging (MRI).
- Conceptualized and performed *in vivo*, parallel T2 weighted multi-slice multi-echo (T2w MSME) 7 Tesla MRI and reflective THz imaging studies. Acquired high contrast imagery of full thickness and partial thickness burns in pre-clinical rat models to investigate the spatiotemporal evolution of THz imaging contrast in wound responses. Published the first *in vivo* evidence of TWC as the primary contrast mechanism of THz imaging and the sensitivity and specificity of MRI for measuring burn TWC *in vivo*.
- Authored and was awarded funding ($407,484) for an R21 application to correlate spatially and temporally resolved THz reflectivity maps of skin burns with mobile water measurements acquired with MRI.
- Authored an R01 application to explore the clinical efficacy of using TWC maps in a pre-clinical model to predict tissue viability earlier than what is currently possible with clinical indication and research diagnostic systems.
- Designed and performed 7T MR-THz feasibility studies in *ex vivo*, porcine skin burn models through collaborations with the Ahmanson-Lovelace Brain Mapping Center (ALBMC), UCLA. Published the first fused image of an MR-THz skin burn and laid the groundwork for future, parallel MRI and THz imaging of *in vivo* rat models to further substantiate the clinical efficacy of reflective THz imaging in burn wound care.
- Worked on the first *in vivo* THz burn trials to demonstrate the feasibility of reflective THz imaging as a clinical diagnostic tool for early and accurate detection of burn severity and corneal hydration. This work resulted in a provisional patent application for corneal hydration sensing and burn sensing, respectively, in which I am listed as a co-inventor.

Mentorship, UCLA, Department of Engineering **Jun 2011 - Jun 2014**
Coordinator and Mentor

- Trained and managed an undergraduate student from Johns Hopkins University in calibrating and optimizing THz system optics for hydration calibration studies. Published a manuscript in SPIE, Terahertz and Ultrashort Electromagnetic Pulses for Biomedical Applications, in which the student is listed as a co-author.
- Mentored students from the Center for High School Summer Research Program (HSSRP). Coordinated lectures and lab tours in minimally invasive technologies.

Howard Hugh's Medical Institute, University of California, San Francisco (UCSF), CA **Feb 2009 - Aug 2009**
Senior Research Associate I

- Worked on the construction of high-throughput genetic interaction maps for the BAR domain superfamily in *Schizosaccharomyces pombe*.
- Developed and performed PEM-2 strategy for systematic double mutant construction to ensure expression of both cycloheximide
  sensitivity and resistance in latter mating steps of h- and h+ *pombe* strains.
- Amplified NAT selective marker using Bioneer designed primers and Iproof pcr reagents, introduced marker via high-throughput NAT switching (96 well plate transformations of KAN marked parents), preformed replica plating to isolate successful transformants, and designed transchromosomal pcr primers to amplify NAT switched domains. Revised strategy to include fusion pcr due to 10% success rates of NAT switching transformations.
- Researched deletion strain libraries and Q-arrays to conduct mating, sporulation, and GC1 and GC2 *pombe* screening tests via an automated Singer robot.

Microfabrication Laboratory, Johns Hopkins University (JHU), Baltimore, MD **Sep 2007 - Dec 2007**
Optical Waveguide Senior Design Project

- Designed an inexpensive, photolithographically patterned optical waveguide in a standard silicon wafer disk that resulted in a 95% signal to noise ratio (SNR).
- Customized and performed wet thermal oxidation protocols, photoresist (S1813) deposition, photomask alignment and exposure, and standard buffered oxide and KOH etch procedures.
- Designed and constructed reflective aluminum mirrors along the channel walls to achieve a high yield of total internal reflection and successful transmission of incident input rays. Incorporated an optical cable into the waveguides to improve upon the original construct.

Allergy and Clinical Immunology, Johns Hopkins Medicine, Baltimore, MD **Sep 2006 - May 2007**
Research Assistant

- Recovered optimal titer concentrations of IgE antibody using ELISA for signal transduction studies in mast cells.
- Designed serial dilutions of standards and varying IgE samples based on absorbance readings of photospectrometer results to successfully recover at least 75% of the original anitobody.
- Performed both large and small scale dialysis procedures using Pierce cassettes and ammonium sulfate purification protocols.

Chemistry Laboratory I and II, JHU, Baltimore, MD **Sep 2006 - May 2007**
Teaching Assistant

- Managed and trained Freshman students in the Chemistry lab room in performing experiments that supplemented their curriculum, including electrochemistry, kinetics, and equilibrium protocols.
- Organized help sessions to provide one-on-one feedback for students and graded all laboratory reports.

Lab Vision Corporation, Fremont, CA **Jun 2005 - Aug 2005**
Marketing and Product Development Intern

- Participated in the development of antibodies for tissue staining and quality control of reagents in the immunohistochemistry lab. Developed techniques, including fixation of tissues, microtoming, H & E staining, and analysis using an optical microscope. Programmed and operated an auto-stainer and PT module, and prepared antibodies and reagents.
- Researched patents and patent applications for instruments and methods relating to novel digital imaging of blood cells and mechanical mechanisms for microscope slide handling.
- Collaborated with the Lab Vision marketing team on the annual catalogue to include new antibodies and reagents, reviewed datasheets for company products, and catalogued product information.

Johns Hopkins BME Group, Baltimore, MD **Sep 2004 - May 2005**
Design Team Member

- Developed an accurate, inexpensive and user friendly computer interface controlled by changes in eye movement to facilitate paraplegic patients.
- Combined a sensor unit consisting of two infrared sensors and an LED, all mounted onto a flexible and comfortable head apparatus, to non invasively translate eye motion into cursor movement.
- Enhanced the prototype's sensitivity to varying light conditions through the inclusion of an auto-calibration feature.
- Participated in the Hopkins Business Plan Competition and received $1500 for second place, and qualified for the semifinals in Moshpit competition.

CHAPTER 1: INTRODUCTION

Wounds are a serious public health issue. The worldwide burden of surgical wounds and burn injuries is estimated to be ~40-50 million and ~7-10 million people, respectively [1]. In the United States alone, cutaneous wounds cost over $25 billion annually [2]. Early and accurate assessment of a wound and/or its healing potential are the most important determinants of the therapeutic management of patients sustaining a cutaneous injury. The difficulty lies in distinguishing wounds or surgical tissue replacements, especially at the early stages, that will heal well without clinical intervention from those that require excision and/or surgical re-exploration to prevent necrosis. A false negative assessment has important clinical consequences: slower healing times, greater chances of infection, increased length of hospital stay, higher treatment costs, as well as a reduced functional and aesthetic outcome.

In the case of both burns and tissue flaps, which have become essential for the surgical reconstruction of patients with large soft tissue defects like burns, the difficulty with their evaluation stems from the traditional diagnostic markers of wound severity and/or viability: the appearance of the wound and sensitivity of the wound to touch. This method, which relies on the experience of a surgeon, has a poor diagnostic accuracy and can only be applied to assess the severity of burn wounds that have reached their final healing state (i.e. very deep and very shallow burns) and the viability of tissue flaps that immediately show gross signs of necrosis. Inaccurate clinical inspection can often result in unnecessary operations or delay of grafting/flap procedures. More quantitative, adjunct methods for both burn wound and tissue viability assessment primarily include tissue perfusion measurements.

Perturbation in tissue perfusion that follows a thermal or surgical (i.e. tissue flap) insult to the skin is preceded by the immediate, rapid accumulation of fluid in tissue, clinically termed edema. Laser Doppler imaging (LDI) is a useful technique for studying and estimating perfusion

characteristics of burn wounds as well as tissue flaps *in vivo* only after edema has completely subsided [3]–[5]. This is typically ~ 48 hours in advance of clinical judgment, indicating clinical experience alone requires at least 3 – 4 days of elapsed time to arrive at sufficient prediction accuracy. Although the overall accuracy of burn depth and flap viability assessment using LDI techniques has been reported to be as high as 92% compared to histology, it is still significantly confounded by the presence of edema in the wound bed during the acute stages (i.e. the first 24hrs) of injury [3]–[5]. Excess tissue water content (TWC) in the wound affects wound temperature by increasing tissue heat capacity and heat conductivity, which can alter flow readings and perturb laser illumination fluence and the detection of Doppler shifted signals. Because edema is a characteristic component of the tissue response to injury and precedes microvascular changes associated with tissue perfusion, detection and monitoring of TWC - the primary indicator of edema - could provide more early and useful diagnostic information for both burn wound and flap viability assessment.

Early evidence suggests that visualization of TWC changes in superficial tissues may be possible with reflective terahertz (THz) imaging [6], [7]. The THz band refers to non-ionizing electromagnetic waves in the 100 GHz to 10 THz frequency range. Reflection imaging of biological tissue at THz wavelengths has shown high contrast in rapidly and efficiently distinguishing abnormal tissue from healthy tissue in cornea and in skin injuries [8]–[14]. Reflective THz imaging is unique in that it: I) offers distinct advantages over earlier transmission-based systems for *in vivo* applications due to the high THz absorption in tissue; II) probes the dielectric properties of tissues using simple optical components; and III) is minimally perturbed by surface characteristics like hair and tissue surface roughness. Unlike depth-resolved images of tissue acquired with magnetic resonance imaging (MRI), THz images of tissue are 2D reflection maps representing an aggregate tissue property. Because water constitutes ~70% of the weight of soft tissue, and the THz frequency dielectric constant of water is significantly higher than that of non-water constituents, the aggregate reflected signal observed with *in vivo* THz imaging is

interpreted as TWC [15]. However, liquid water displays broad absorption bands rather than *narrow* absorption signatures in the THz band. Consequently, this observation does not identify TWC as the primary source of contrast in THz imaging. Therefore a companion imaging modality that relies on TWC to generate image contrast is currently needed to interpret and validate contrast in THz tissue data.

Recent results show that magnetic resonance imaging (MRI) can be used to verify the contributions of TWC to THz imaging of superficial tissues [12]. Despite its limited access and associated costs, MRI can resolve depth information and provide comprehensive, layer-specific anatomical and physiological data on TWC in a single setting [16], [17]. Correlating THz-TWC contrast with MRI is the first step towards investigating the potential of THz imaging to track edema in superficial tissue such as tissue flaps and burn wounds. Though our group has previously reported extensive work on THz burn imaging, the pathogenesis of fluid shifts secondary to thermal injury is not completely understood. Characterization and advancement of the current reflective THz system, as well as improvements in the experimental burn methodology *in vivo*, may offer more repeatable and clinically relevant THz measurements of fluid shifts in burn wounds. Insights gleaned from these THz imaging developments can be further implemented in unexplored wounds models in medical THz imaging, such as tissue flaps.

The aim of this thesis is to investigate TWC-based THz imaging contrast, develop advancements in reflective THz imaging for more repeatable tracking of TWC *in vivo,* and demonstrate the potential of this emerging technology for the assessment of burn wounds and tissue flap viability. This task first entails characterization of the hydration sensitivity of the current THz imaging system with tissue mimicking phantoms. Second, THz image contrast must be explored with a TWC sensing technique, specifically T_2-weighted MRI, in *ex vivo* and *in vivo* models. MRI imaging sequences and experimental groundwork developed in these preliminary studies can be implemented *in vivo* in correlational THz-MRI imaging of burn-induced edema in pre-clinical rat models. The ability to track fluid shifts immediately following injury may further

support THz imaging as an emerging method to enhance the standard assessment of burn wounds and tissue viability. Next, improved THz imaging methodologies must be developed and implemented *in vivo* to acquire reproducible THz-TWC maps in burn wounds and interpret these results in the context of burn edema pathophysiology. These advancements will include 1) an image registration method to reliably compare THz-TWC measurements with histological wound outcome; 2) a reproducible contact-burn induction technique; and 3) the use of multiple dielectric windows. Differences in THz burn contrast will be further substantiated by image intensity histograms. Finally, insights into edema pathogenesis in burn injuries will be implemented in the first *in vivo* pilot study to investigate the utility of reflective THz TWC imaging for early assessment of flap viability. Reflective THz imagery will compare 3 bipedicled flaps (i.e. survival model) and 3 excised flaps (i.e. failure model) in the dorsal skin of rats over a 7-day period to investigate the practical potential of THz TWC sensing to accurately detect flap failure earlier than clinical examination.

Collectively, this thesis sheds more light on THz imaging contrast and builds upon the *in vivo* THz imaging work previously reported by the University of California, Los Angeles (UCLA) Biophotonics group. This research effort began as a collaboration with the Center for Advanced Surgical Interventional Technology (CASIT) to develop a non-invasive imaging tool for monitoring tissue fluid shits in edema provoking processes.

CHAPTER 2: BACKGROUND

2.1 TERAHERTZ (THz) WAVES

Terahertz (THz) radiation is electromagnetic radiation whose frequency lies between microwaves and infrared regions of the spectrum. Although we cannot see THz radiation, plenty of THz radiation sources fill the space of our everyday life, from cosmic background radiation to blackbody radiation from room temperature objects. Most of these THz sources are incoherent and can hardly be utilized. Until recently, this region of the electromagnetic section remained largely unexplored due to the technical challenges involved in developing efficient and compact THz sources and detectors. Advances in both optical and microwave technologies, however, have diminished this "THz gap." This chapter offers a brief description of the basic properties of THz radiation and its interaction with materials to lay down the foundation for investigating the origin of contrast in THz imaging *in vivo.* An understanding of THz contrast mechanisms is key in accurately interpreting *in vivo* THz surface maps of tissue for medical diagnoses, including surgical and burn wound assessment.

2.1.1 What is The "THz Band"?

The THz band, as seen in **Figure 2-1**, refers to the spectral region between 300 GHz and 3 THz (0.1 mm – 1 mm). In the electromagnetic spectrum, radiation at 1 THz has a period of 1 ps, a wavelength of 300 μm, a wave number of 33 cm-1, a photon energy of 4.1 mev, and an

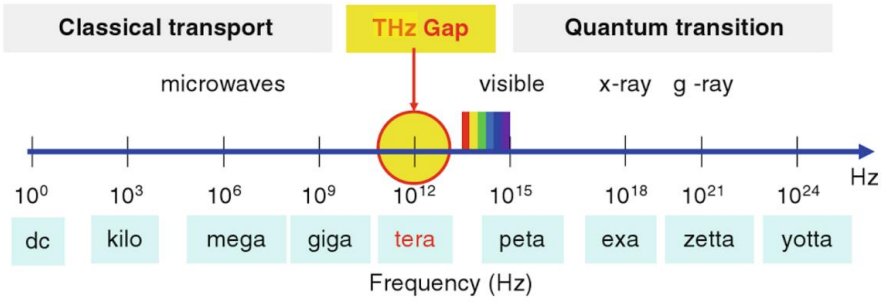

Figure 2-1: The electromagnetic spectrum. The search for potential applications using THz radiation is steadily intensifying as materials research provides improved emitters and detectors [18]

equivalent temperature of 47.6 K [18]. In the same way that visible light can create a photograph and X-rays can be used to see shapes in the human body, terahertz waves, also known as "T-rays," can create 2D reflection images of tissue as well as a transmit information.

Terahertz radiation demonstrates several properties that make it an attractive medical imaging technique. For example, terahertz wavelengths are longer than infrared and optical radiation, and, therefore, scattering in biologic tissue is smaller in comparison [19]. THz wavelengths are sufficiently short that a submillimeter lateral resolution of more than 200 μm at 3 THz is readily achievable with an axial resolution of 40 μm [20]. Terahertz radiation is also nonionizing, such that the observed power levels do not cause any known detrimental effects to dividing human cells and are many orders of magnitude lower than those in recommended safety guidelines [21], [22]. The technique has a very high signal-to-noise ratio due to the efficient elimination of the background noise with coherent time-gated detection . Furthermore, the broadband THz frequency content can be used for spectroscopic studies of biomolecules and *in vivo* and *ex vivo* imaging of tissue, including skin cancer, wounds, and corneal pathologies [23].

The key advantage is that the characteristic energy of the hydrogen bond, which is the most dominant bond in biological molecules, lies in the THz frequency range. Therefore, THz waves can directly detect spectral features such as resonances and motions of molecules (**Figure 2-2**). In addition, the dielectric properties of water at THz frequencies yield easily detectable

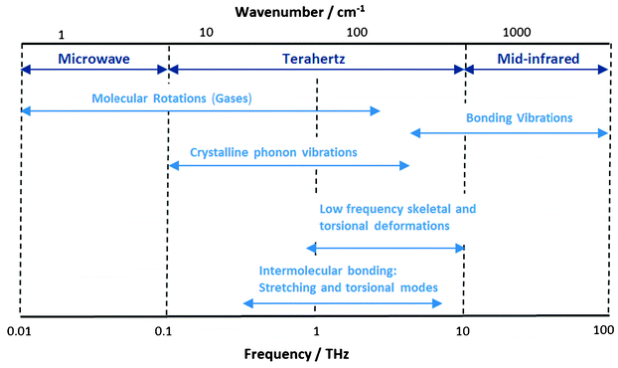

Figure 2-2: Molecular modes and activity in the terahertz region of the electromagnetic spectrum [24]

increases in THz reflectivity for small increases in hydration concentration. Because the absorption of THz waves is sensitive to polar molecules, such as water, unusual reflections from diseased tissue, which has different tissue water content (TWC) levels from normal tissue, can be detected.

2.1.2 THz-Tissue Interactions

Similar to most interactions with tissue, the electric field is the appropriate theoretical framework to describe the relationship between THz energy and biological molecules, cells, and tissue. Electric permittivity (ε), the ability of the medium to be polarized, and bulk conductivity (σ), a measure of the ease of movement of ions through a medium, are two parameters used to characterize THz wave interactions with tissues at the macroscopic level. In this approach, tissue is reduced to a collection of molecules comprised of water and proteins to describe the bulk motion (permittivity and conduction) of the medium. To better understand the microscopic absorption of THz radiation due to transitions between molecular energy states, further insight into molecular and quantum energy levels is required. For diatomic molecules (atomic mass < 20), the energy separation between two consecutive rotational states is $\Delta E \sim 1.602 \times 10^{-22}$ J, corresponding to a frequency of 0.242 THz [25]. This confirms that the absorption of THz radiation is likely to generate variations in the rotational states of simple polar diatomic molecules. This treatment of molecular absorption spectra also suggests that simple polar molecules are likely to yield THz absorption spectra, and these are indeed observed in studies of water.

Groups have investigated water in the terahertz region to both characterize the molecular dynamics of water and to determine the effects of water in biological systems [26], [27]. Measurements of water may be analyzed in terms of the complex dielectric constant $\varepsilon^*(\omega)$ in **equation (1)** , where ω denotes the angular frequency, or the complex refractive index $n^*(\omega)$ in **equation (2)** where

$$\varepsilon * = \varepsilon(\omega) - i\varepsilon'(\omega) \quad \textbf{(1)}$$

$$n * = n(\omega) - iK(\omega) \quad \textbf{(2)}$$

With ε, ε' and n, K denoting the real and complex components of $\varepsilon^*$and n^*, respectively. Simple dielectric relaxation models for permittivity and conductivity, specifically the Double Debye model, agree with the experimentally derived complex dielectric constant of water up to at least 1 THz. Water demonstrates two dielectric dispersions with relaxation times τ and characteristic frequencies such that τ_1 = 8.4 ps (f_{c1}=0.019 THz) and τ_2 = 0.19 ps (f_{c2}=0.84 THz), and corresponding real dielectric constants ε_1=78.36 and ε_2=4.93 [27], [28]. The slower relaxation time is related to the breakage of hydrogen bonds and the fast relaxation time is the reorientation time of a single water molecule with a small moment of inertia. At higher frequencies (6 THz or more), the response of dipolar liquids, including water, to the electric field is no longer overdamped and instead becomes resonant. Liberations, described as periodic motions, are evident as absorptions that are no longer associated with a monotonic decreases in the dielectric constant as the frequency increases. The presence of these resonant bands results in deviations from the dielectric relaxation models, and water has a particularly large and broad vibrational and stretching mode.

2.1.3 THz Imaging of Skin

Studies have focused on the exploration of THz frequency resolved properties of healthy, diseased, and injured skin tissue due to its location on the surface of the body and the limited tissue penetration depth (33 μm to 3000 μm) that render most other *in vivo* applications impossible [6], [9], [12], [13], [13], [29], [30]; this water absorption can mask the characteristic features of samples that lie deep in the body. THz groups at Leeds, Cambridge, and TeraView have published extensively on THz imaging of skin cancer, specifically basal cell carcinoma (BCC), presenting data from both *ex vivo* and *in vivo* specimens [12]–[14]. Wallace et al.

undertook a study on the absorption of excised BCC samples from 19 patients and reported successful discrimination between diseased and healthy tissues [14]. To perform these studies, a tissue specimen is placed in the THz beam and the change in the reflected/transmitted THz waveform, relative to the illuminating waveform, is quantified and used to compute the complex refractive index of the material. Over the frequency range 0.2–2.0 THz, it has been shown that *in vivo* BCC tissue is characterized by both a higher refractive index and absorption coefficient than that of normal tissue. Dielectric relaxation models, including the double Debye model, afford an ensemble of relaxation times that produce good, statistically significant fits to experimental data and support the hypothesis of the presence of a dispersive, polar medium (i.e. water); the Debye model represents the dynamics of water with two relaxation times: 1) the slow relaxation time (in picoseconds) is related to the breakage of hydrogen bonds; and 2) the fast relaxation time (in hundreds of femtoseconds) is the reorientation time of a single water molecule with a small moment of inertia. Therefore, these measurements offer macroscopic information on water dynamics in terms of the complex permittivity or the refractive index.

2.1.4 THz Contrast Mechanism: Unknowns

Unlike depth-resolved images of tissue acquired with magnetic resonance imaging (MRI), THz images of tissue are 2D reflection maps representing an aggregate tissue property. Because water constitutes ~70% of the weight of soft tissue, and the THz frequency dielectric constant of water is significantly higher than that of non-water constituents, it is highly likely the aggregate reflected signal observed with *in vivo* THz imaging is due to variation in TWC [13], [15]. Evidence from PET and MRI studies also indicate that tumors have increased water content compared to normal tissue, which could explain the aforementioned contrast observed in THz reflection images of BCC [31], [32], [33, p. 199], [34]. However, liquid water displays broad absorption bands rather than *narrow* absorption BCC. However, liquid water displays broad absorption bands rather

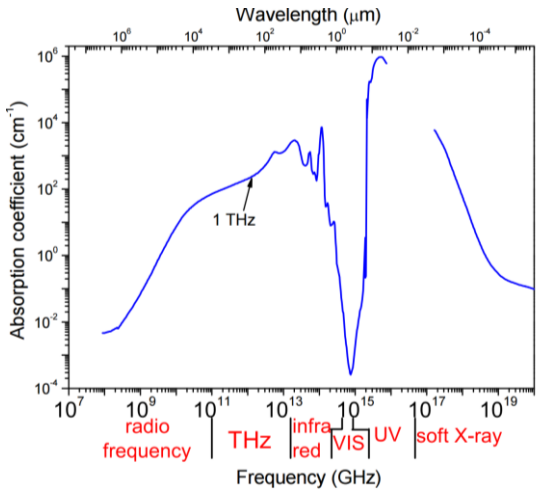

Figure 2-3: Absorption spectra of liquid water

than *narrow* absorption signatures in the THz band (**Figure 2-3**).

Water concentration is not the only likely factor contributing to contrast on terahertz images of BCC tumors. Authors of a number of studies have imaged biologic samples that were fixed in formalin, dehydrated, and embedded in wax for histopathologic examination and still found contrast between tumor and the surrounding normal tissue [35], [36]. For example. Transmission terahertz images of dehydrated and wax-embedded tissue have also shown contrast of liver metastases and human melanoma. This would imply that water, although dominant, might not be the only mechanism responsible for the changes in the properties of cancerous tissue. Other changes, such as increased cell density, may lead to scattering by structures on the same scale as the wavelengths. Further studies are required to determine the effects of structure on terahertz imaging. Also, the increased concentration of certain proteins within BCC, such as actin and amyloid as well as collagen, keratin, and skin lipids, could also be a factor. Proteins in solution change the binding state of water by modulating the hydrogen bonds and hence subtly affect the properties at terahertz frequencies. Collectively, these observations do not identify TWC as the primary source of contrast in THz imaging. Therefore a companion imaging modality is currently needed to interpret contrast in THz tissue data.

Recent results show that MRI can be used to verify the contributions of TWC to THz imaging

of superficial tissues [12]. Despite its limited access and associated costs, MRI can resolve depth information and provide comprehensive, layer-specific anatomical and physiological data on TWC in a single setting. A central aim of this thesis is to I) investigate TWC as the underlying biophysical driver of observed changes in THz reflectivity and II) quantify, for the first time *in vivo,* the tissue depths at which THz imaging can potentially probe fluid shifts following injury. *In vivo* burn wounds are known to severely and acutely perturb TWC and, thus, are selected as the injury model for this correlative study. In addition, previous work in THz wound imaging has also shown that burn wounds of varying severity produce pronounced and distinct spatiotemporal changes in THz image contrast [9]. It is important to note that MRI is only used here for pre-clinical research purposes, as its cost and limited portability make it inappropriate for TWC characterization in patients, especially critical patients. It is hypothesized that MRI TWC-based contrast will: I) exhibit unique signal characteristics for each wound model; and II) agree with trends observed in the companion THz burn imagery. Insights gleaned from these correlational studies are used to demonstrate the potential of THz imaging for assessing and monitoring fluid shifts following burns and surgical wounds, such as flaps, that are commonly used in the reconstruction of wounds.

2.2 SKIN

2.2.1 Skin Physiology

A proper description of burn wound and tissue skin flap assessment requires a basic understanding of the physiology of the tissue involved. In both size and weight, the skin constitutes the largest organ in the body. The functions of skin include 1) protection of the underlying tissues from physical, chemical, and thermal trauma; 2) thermal regulation and control of blood flow; 3) impermeability to both tissue fluids and environmental chemicals; 4) and sensory perception [37]–[40].

The skin consists of a stratified structure with three parallel layers; an outer, thin epidermis; a dense, non-cellular connective tissue termed the dermis; and a thick, subcutaneous fatty tissue, also known as the hypodermis. A cross-sectional anatomy of the skin is shown in **Figure 2-4** [41]. Although a single organ, depending on the location on the body, skin is highly diversified both physiologically and anatomically. These variations result in differing sensitivities to thermal and physical trauma and susceptibility to severe injury.

The epidermis is a stratified, highly cellular membrane measuring 0.06-0.8 mm in thickness depending on location on the body **(Figure 2-5**) [42]. Since the epidermis is devoid of blood vessel, lymphatics, and connective tissue, it relies on the underlying dermis for nourishment. In the innermost stratum of the epidermis is the basal (B) layer from which cells are generated and extend towards the skin surface. The next layer is the stratum granulosum (GR), which has a large, transferable TWC (70%) that is involved in water retention and regulation [40]. The stratum corneum (SC) is the outermost, dead, waterproof layer of fibrous keratin protein that contains about only 15% TWC [40]. The ability of the skin to hold water is primarily related to the

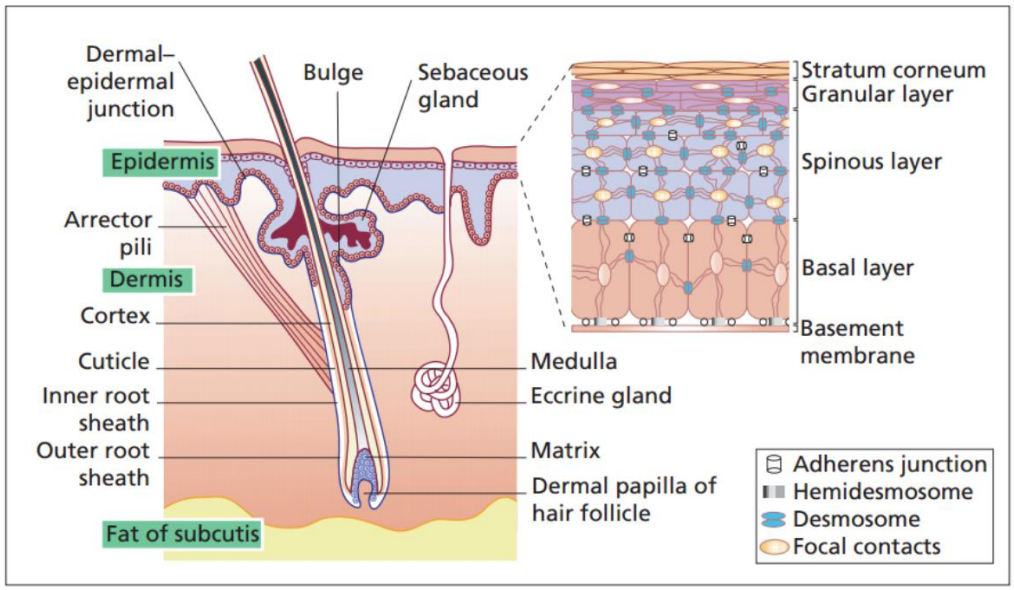

Figure 2-4: Cross-section of skin anatomy [41]

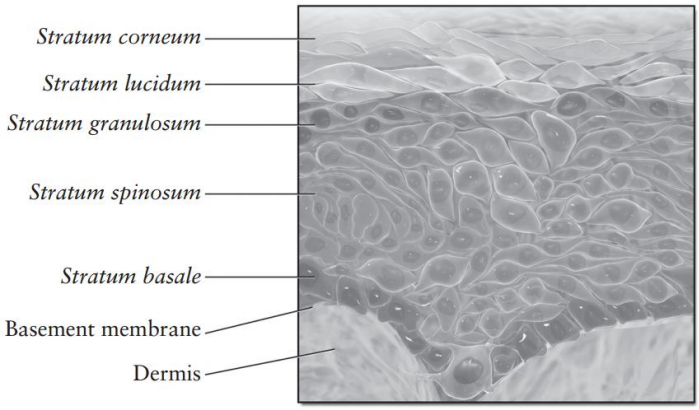

Figure 2-5: Epidermal skin layers [42]

SC, which plays the role of barrier to water loss.

The water content across the epidermis is heterogeneous and is best described by a water concentration profile **(Figure 2-6)** [43]**.** The water content of the SC is known to influence

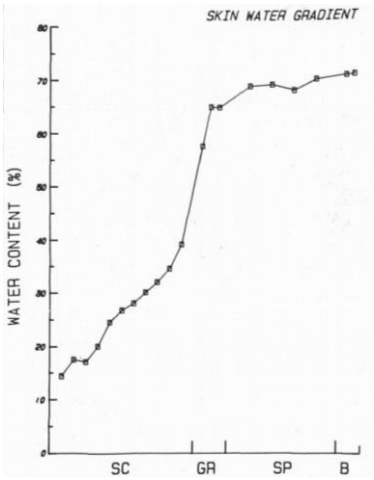

Figure 2-6: Water profile across human skin [43]

1) the brittleness , elasticity, tensile strength, and viscoelasticity;2) barrier characteristics; 3) electrical resistance;4) survival of microorganisms that reach the surface; 5) thermal conductivity; and 6) appearance.

The underlying dermis is 20 to 30 times thicker than the epidermis and contains the vascular, nervous, lymphatic, and supporting structures of the skin [40]. Mastocytes, which release histamine, are found in this skin layer. Damage to these cells initiates the localized

inflammatory response. The papillary layer is the superficial layers of the dermis and contains numerous, highly vascularized protuberances called papillae that play an important role in the tissue response to local and systemic stress.

The subcutaneous tissue comprises of connective tissue and fat which are important in determining the degree of injury for severe thermal or physical insult [40].

2.3 EVALUATION OF TISSUE WATER CONTENT (TWC) IN SKIN

2.3.1 TWC Assessment

TWC uniquely affects physical properties important to the function and appearance of skin such as permeability and flexibility. Therefore, maintaining the appropriate TWC is a key clinical and cosmetic concern. This importance is reflected in the diversity of techniques that have been developed to evaluate TWC in skin. Traditional techniques used to measure skin hydration *in vivo* do not directly monitor TWC, but rather infer its presence as a result of changes in a particular skin parameter, e.g. electrical conductivity or transepidermal water loss (TEWL) [44], [45]. These techniques are invasive and may result in the temporary deficiency of stratum corneum barrier function [46]. Often times, water-holding capacity, or an increase sweat gland activity, might be evaluated as actual skin water content. High-resolution ultrasound and infrared spectroscopy are non-invasive techniques and have been employed to study the skin [47]. The latter gives a mean value of water content, while the former is suitable for delineating skin structure, but not hydration [48].

2.3.2 MRI of Skin

Magnetic resonance imaging (MRI) has a number of advantages over other principal alternative skin imaging techniques. This technique allows direct quantitative and non-invasive measurements in the skin. The most obvious is that it generates a map of water distribution, not degraded by the presence of dense tissue, as is the case with ultrasound imaging. Unlike the other techniques that have limitations in depth measurement and/or measure the mean value of

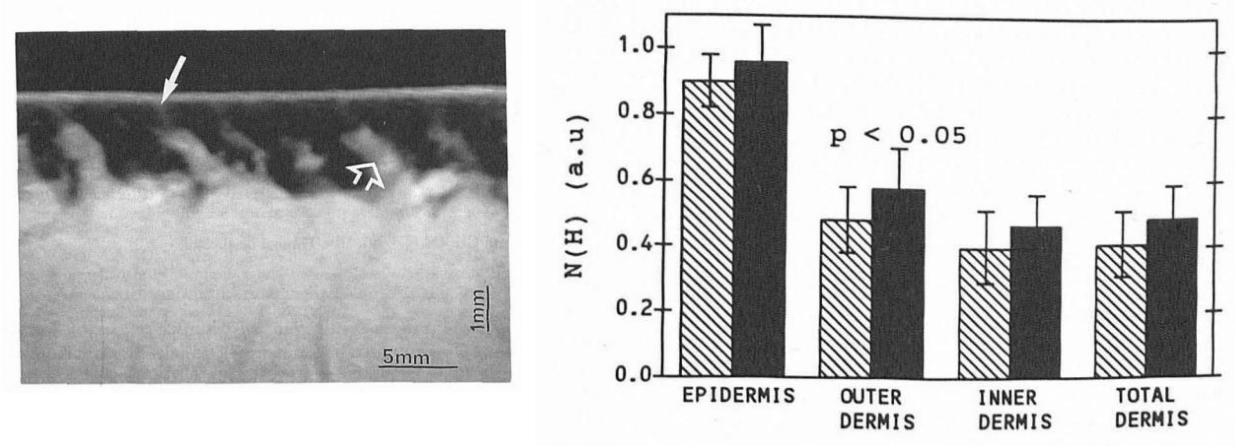

Figure 2-7: (Left) T2-weighted In vivo MRI of skin on thigh. The outer bright thin layer corresponds to the epidermis. Dermis appears as a darker layer. Hypodermis appears as a homogenous bright area. (Right) Proton densities associated with young and old subjects [49]

the water content, MRI gives direct tissue localization through slice selection in any depth of material and shows the spatial water distribution within the selected slice [43], [45], [49]–[55]. By modifying the acquisition parameters, the MRI image contrast can be made sensitive to parameters such as longitudinal proton relaxation time (T_1) and transverse component of the proton relaxation time (T_2) (**Figure 2-7**). Using different MRI techniques, *in vivo* high-resolution images of high quality and contrast can be obtained to differentiate the hydration state of the tissues and highlight particular tissues in different skin layers.

2.3.3 T_2 Relaxation Time and Proton Density

The dependence of MR image intensity upon selectable imaging parameters means that many different types of image contrast can be produced by MRI. The strength of the signal (S) from a given tissue is proportional to the product of three weighting terms as shown here in **equation (3)** for the gradient–echo (GE) acquisition method:

$$S = N(h)\left[1 - \exp\left(-\frac{T_R}{T_1}\right)\right] x \left[\exp\left(-\frac{T_E}{T_2}\right)\right] \quad \textbf{(3)}$$

where N(h) is the proton density, the fraction of mobile water protons available in the tissue; the second term in the product is the 'T_1-weighting' term; and the third term is the T_2-weighting term.

'Weighting' refers to the influence of a given term on image contrast, attributable to differences in tissue parameters N(h), T_1 or T_2. The water content in human soft tissue varies only by about 20%, thus the contrast seen in MR images is often primarily due to T_1 and T_2 variations and only secondarily to proton density variations.

In the above equation, there are two parameters that are set by the user; these are the pulse repetition time (T_R), and the echo delay time (T_E). T_R is the time between successive radio frequency (RF) excitations for a given imaging slice. The intrinsic T_1 value of the tissue determines the rate at which longitudinal magnetization recovers. By choosing T_R appropriately, one can control the extent to which the magnetization is allowed to recover. T_E is the time delay between the RF excitation and the measurement of the signal. Transverse magnetization created by an RF pulse begins to dephase immediately after the pulse due to T_2 and other effects, such as field inhomogeneity effects. A short T_E sequence will measure maximal signal early in the decay, while a long T_E sequence will measure less signal later in the decay.

Among the multitude of sequences available, T_2-weighted (T_2w) MRI has previously been used to generate native, pathology-specific tissue contrast for cerebral, myocardial, as well as skeletal muscle edema assessment [56], [57]. To obtain T_2 contrast between tissues, longer T_E times are used. To minimize the effects of T_1-weighting, T_R is set to be approximately two or three times longer than T1. In T_2-weighted images long-T_2 species appear brighter than tissues with shorter T_2.

The MRI signal, S, for a T_2w image is simplified to **equation (4)**:

$$S = p\left[\exp\left(-\frac{T_E}{T_{2*}}\right)\right] \quad \textbf{(4)}$$

T_2 relaxation time measurements can be performed by acquiring spin echo images only varying TE while keeping TR fixed. T_2 is calculated by fitting to **equation (4)** the signal intensity S from a region of interest (ROI) in each of the spin echo images. From this, can then then quantify

modifications of the mobile water fraction (*N(h))* in tissues of interest.

2.3.4 Background in MRI Skin Imaging

Magnetic resonance imaging (MRI) has been previously used to visualize changes caused by water ingress and egress *in vivo* in skin. The first *in vivo* cross-sectional MR image of skin was reported in 1986 with 100 μm resolution in the depth direction at a magnetic field strength of 0.1 T [58]. There are reports of proton density, T_1- and T_2*-weighting images to observe finger, heel, arm and thigh skin [16], [59]–[61]. Higher spatial resolutions, such as 18 μm × 312 μm × 1000 μm, have been reported for probing micro-architecture of the normal human skin [62]. Regardless of all the successful attempts toward achieving high-resolution MR images in the skin, *in vivo* quantitative work in skin to provide additional information to visual inspection is in the preliminary stage. This is partly because skin has a relatively short T_2 compared with other soft biological tissues, hence short echo time, TE imaging is required. Currently using TE=16 ms, T_2 of the dermis has been measured at 28 ms. Song et al. concluded that 90% of the dermis signal consists of a fast relaxing component with T2*=9.8 ms [63]. From this latter work, it is clear that T_2 relaxation of dermis is multi-exponential, which reflects the fact that water is in a number of environments (i.e. water with different degree of mobility). For example, as is known these range from tightly bound to collagen to being relatively free in the intra-cellular environment. Changes in the proportion of bound to free water may be of importance when either monitoring skin under pathological conditions or in the evaluation of the effects of drug interventions.

THz researchers have suggested that MRI can be used to verify the contributions of TWC to THz imaging of superficial tissues [12]. Despite its limited access and associated costs, MRI can resolve depth information and provide comprehensive, layer-specific anatomical and physiological data on TWC in a single setting. Among the multitude of sequences available, T_2-weighted (T_2w) MRI has previously been used to generate native, pathology-specific tissue contrast for cerebral, myocardial, as well as skeletal muscle edema assessment. Tissue contrast

in T_2w MRI is primarily determined by differences in the T_2 relaxation time, from which relative proton density can be calculated. In fact, relative proton density has been used to distinguish protein-bound water from “free” water (i.e. effusion or edema) in superficial tissues that have also been explored with THz imaging. These tissues include uninjured and diseased skin *in vivo* as well as wounds of increasing severity (superficial, superficial partial, deep partial, and full thickness) *ex vivo*. Among wound models, *in vivo* burn injuries are characterized by the biggest inflammatory reaction and result in substantial and rapid edema formation [64]. Moreover, insights gleaned about THz image contrast in pre-clinical burn wound models can be leveraged to advance burn assessment, a method that still heavily relies on a subjective evaluation of the external features of the wound to diagnose burn patients.

2.4 BURN WOUNDS

2.4.1 Burns: Epidemiology

Burns wounds continue to be a widespread and burdensome critical care problem. Acute thermal injuries affect nearly 500,000 Americans each year, with ~50,000 hospitalizations and 3,400 deaths recorded annually [4] **(Figure 2-8)**. Most of these injuries are preventable, as evidenced by declining burn incidence rates reported by the American Burn Association, and are largely attributed to prevention strategies. Despite these precautions, burns are consistently reported as a leading cause of injury and death among children and adults older than 34 years

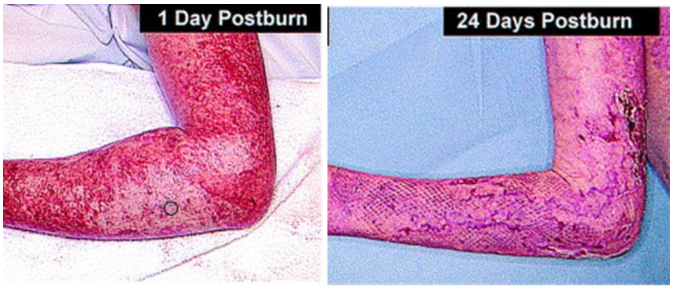

Figure 2-8: Burn wound. Visible images taken at 1 day and 24 days post thermal injury [65]

[66]. The socioeconomic impact of burn wounds is apparent in direct correlations that have been established between burn severity, length of hospital stay, and cost. Lifetime costs per burn death are almost six times those for heart disease and four times those for cancer [4], where the United States government bears ~28% of the direct costs. In addition to cost, burn wounds are associated with a myriad of physical complications due to muscle weakness, hypertrophic scarring, contractures, nervous system injury and psychosocial issues [66].

2.4.2 Burn Depth

Thermal burns account for ~ 80 % of all reported sources of burn wounds and can be classified based on depth of tissue involvement [66]; along with the total surface area burned, this metric describes the severity and assesses the prognosis for burn injury. The following classifications are commonly used:

- *Superficial burns (1st Degree)* — involve only epidermis
- *Superficial partial-thickness burns (Shallow 2nd Degree)*—involve only papillary dermis and epidermis (**Figure 2-9 (a)**)
- *Deep dermal partial-thickness burns (Deep 2nd Degree*)—involve epidermis and dermis to reticular dermis (**Figure 2-9(b)**)
- *Full thickness burns (3rd Degree)*—involve the whole thickness of the skin and possibly subcutaneous tissue (**Figure 2-9(c)**)

(a) (b) (c)

Figure 2-9: Burn wound depth. (a) Superficial partial thickness, (b) Deep dermal partial thickness, and (c) full thickness burn wounds [66].

Burn wound depth is a, if not the most, significant determinant of patient treatment, healing time, and morbidity (**Table 1**) [67]. While superficial partial-thickness burns are generally treated

non-operatively and heal by re-epithelialization, deeper wounds can often times form hypertrophic or contracted scars. This complexity intrinsic to partial-thickness burns is primarily due to the extent of irreversible thermal damage to the microvasculature and epithelium generation sites [67]. Should an insufficient number of epithelium and microvasculature structures survive ensuing thermal insult, the underlying dermis layer will gradually necrose and approach the burn status of a full thickness wound. These require more aggressive clinical interventions in the form of surgical excision and grafting to prevent a suboptimal outcome [66], [67].

Table 1: DESCRIPTION OF CLINICAL CHARACTERISTICS OF BURN WOUNDS OF VARIOUS DEPTHS

Depth / Degree	*Layer of Skin Involved*	*Appearance*	*Pain*	*Healing Time*
Superficial I°	Epidermis only	Pink to red, moist, no blisters	Moderate-Severe	3-7 days
Superficial Partial IIa°	Papillary dermis	Blister, red, moist	Severe	1-3 weeks
Deep Partial IIb°	Reticular dermis	Dry, white, non-blanching	Minimal	3-6 weeks
Deep III°	All skin layers and subcutaneous fat	Leathery, dry, white or red	None	Does not heal by primary intention

Without timely intervention, the likelihood that many superficial burn wounds can convert to deeper wounds grows. Not only is the extent of burn wound depth a determinant in these more severe wounds (>20% of total surface body area), but increased capillary permeability, hydrostatic pressure, and protein and fluid movement from the intravascular space into the interstitial space become central issues [64], [67]. The edema that forms in the interstitial space forms rapidly in the first 8 h following burn injury, and continues to form more slowly for at least 18hr. Reversal of this process forms the basis for current acute treatment regimens, which require aggressive fluid resuscitation to restore intravascular volume and may lead to resultant edema in other areas [64]. As such, the rapid and accurate assessment and monitoring of wound depth and edema is important in treating patients sustaining burn injuries.

2.4.3 Burn Wound Pathophysiology

Burn wound physiology can be divided into three concentric zones based on the severity of tissue destruction and changes in blood flow: the zone of coagulation, zone of stasis, and zone of hyperemia [67]. The localization of these burn zones is depicted in Figure 2-10. The zone of coagulation is at the central focus of injury and undergoes the most protein denaturation, degradation, and coagulation, leading to tissue necrosis. The most peripheral zone is termed the zone of hyperemia and is characterized by vasodilation and inflammatory changes with no structural damage. With an intact vasculature, this zone will typically recover in the absence of infection or other injury. Between these zones lies an intermediate zone of indeterminate prognosis called the zone of the stasis. The zone of stasis represents a region of vascular stasis and ischemia and is most easily identified in mid to deep dermal burns. This tissue has the potential to heal or alternatively to progress to a full thickness wound, and therefore poses the greatest clinical challenge to burn assessment. In this zone, hypoxia and ischemia can lead to tissue necrosis within 48 h of injury in the absence of intervention. If revascularization is stored within a few days, the ischemic area can be salvaged. Early, accurate identification of zones of burn pathophysiology, a feat that remains to be realized, could prevent progressive tissue loss.

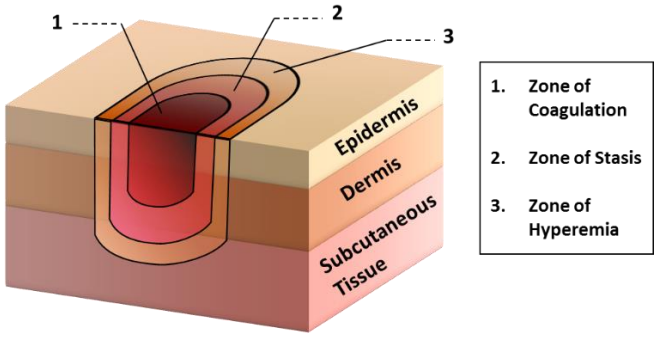

Figure 2-10: Burn wound pathophysiology

2.4.4 Current Burn Wound Assessment

Assessment of burn depth remains an area of wound care still governed markedly by

subjective criteria and intrinsic uncertainty. Numerous clinical indicators include pain, tenderness, presence of blisters, capillary refill times, dermis color palette, and pin prick tests. Despite this armamentarium of classifiers, the clinical estimates of healing time performed by experienced burn surgeons are limited by accuracies between 64% - 76% depending on the study which can further drop to ~ 50% for inexperienced surgeons [4], [68]–[70]. Biopsy, another well-studied and widely accepted method for depth assessment, is not inherently 100% accurate and suffers from high sampling error. Moreover, the structural damage in burned tissue may not necessarily correlate with functional loss, especially for early biopsies when considering the progressive nature of the burn response [66].

Efforts towards increasing objectivity have been widespread and include use of optical technologies given their ability to furnish spatially resolved burn wound assessments. These consist of visible light spectroscopy, fluorescent dye microvascular studies, polarization sensitive optical coherence tomography (PS-OCT), and thermal imaging [71]–[75]. Vital dye techniques are widely known to be adept at detecting necrosis which is a predictor of burn wound depth. However, normal skin controls are necessary for the evaluation of wounds, and the generated images suffer from relatively low intrinsic contrast and spatial resolution [69], [75]. Vital dye contrast is also often unusable in the acute phase of injury due to resultant edema which increases leakage of dyes from damaged blood vessels, perturbing the illumination fluence and emission intensities [69].

PS-OCT systems assess burn depth with depth resolved measurements of polarization rotation induced by collagen denaturation [69], [71], [72]. Similar to the case of vital dyes, tissue edema can perturb polarization rotation sensing as the collagen fibers swell in response to excess water [76], [77]. And such a disturbance changes the polarization resolved signature of bulk tissue. Other notable drawbacks include small imaging fields and limited depth of penetration (few millimeters), deterring use of PS-OCT systems for large scale burn wound assessment. Finally, thermal imaging, which utilizes changes in mid-IR emission induced by variations in blood

perfusion, has not been clinically successful [73], [74]. The presence of blisters and tissue edema in the wound bed can generate enough heat capacity to completely obscure thermal signatures from the vasculature [69].

Laser Doppler Imaging (LDI), the only currently FDA approved technique for burn wound assessment, infers burn wound depth through measurements of blood perfusion in the wound bed [4], [5], [78], [79]. LDI has been shown to determine the need for excision and grafting ~ 48 hours in advance of clinical judgment, indicating that clinical experience alone requires at least 3 – 4 days of elapsed time to arrive at sufficient prediction accuracy [78]. Although the overall accuracy of burn depth assessment using LDI techniques has been reported as 92% compared to histology, it is still confounded significantly by the presence of wound edema and excess fluid in the interstitial spaces of both the dermis and epidermis. Excess TWC in the wound affects wound temperature by increasing tissue heat capacity and heat conductivity, which can alter flow readings and perturb laser illumination fluence and the detection of Doppler shifted signals.

Several key observations can be made on the currently available armamentarium of diagnostic technologies. First, all of the aforementioned techniques, save for PS-OCT, focus on either a direct or indirect measurement of blood perfusion and flow. PS-OCT focuses only on differential changes in the ordered structure of collagen. The physical depth of damage is not explicitly measured but instead inferred from knowledge of the physiology combined with the measured physiologic parameter. Furthermore, many of the studies were correlated with pathology, and researchers have observed that quantitative measurements of depth do not always correlate with time to heal [66]. These findings suggest that physical depth information, while a useful marker in determining the severity and healing viability of burns, is not necessarily the only key determinant in burn wound assessment.

Second, every quantitative diagnostic technique that has been researched for burn applications is confounded by the presence of wound edema [66], [69]. Increased TWC perturbs wound temperature, pressure, blood perfusion, and the properties of light reflected from the

wound bed. If left untreated, wound edema rises significantly in the first 12 hours for both superficial second and deep second degree burns, peaks sometime in the first 24 hours, and then begins to resorb by 48 hours [80]. To this end, many researchers conclude that the dynamic properties of burn wound status and edema prevent quantitative analysis in the first 48 hour following injury [64], [80]. Therefore, more rapid and objective determination of burn depth and healing viability performed within the first 24 hours may result in marked improvements to burn wound care and reduced ambiguity in anticipated burn wound evolution. Moreover, edema by be a potentially useful diagnostic imaging target for assessing burn severity and tissue viability *in vivo*.

2.4.5 Edema Pathogenesis

Profound tissue edema, or swelling, is a well-recognized entity following thermal injury [80]–[87]. Clinical edema, as seen after burns, is an expansion of the interstitial liquid volume [80]. The term interstitium, which refers to the intervening space between vascular and cellular compartments, binds the structural and cellular elements into a tissue, such as observed in the skin dermal matrix [82]. The complications of edema formation in burn patients are mainly the massive losses of intravascular fluid. Hypovolemia will occur after large burns if massive volume resuscitation is not provided, particularly in the first few hours after injury, when edema formation is most rapid [86], [87]. The resultant edema leads to tissue hypoxia and in increased tissue pressure with circumferential injuries, which can result in further injury. Increased interstitial pressure in burned soft tissue compartments often requires escharotomy or even fasciotomy [88], [89]. There also appear to be increasing reports of edema-induced problems such as the compartment syndromes.

Edema is most prominent in or directly surrounding the burned tissues; however, edema formation can also be found in non-traumatized tissues, including non-burned soft tissue, muscle,

intestine, and lung. Some reports indicate that as much as 50% of the extracellular edema observed in large burns is found in surrounding uninjured tissues [90], [91]. Some of the resultant edema is due to intracellular swelling, particularly evident in muscle tissue where a decrease in muscle membrane potential has been measured after thermal injury, allowing excess sodium ion and water to enter these cells [86]. However, the major portion of the edema is caused by fluid collection in the interstitial space of the burn tissue and in the tissue beneath and surrounding the burn. The pathophysiology of both the generalized and local microvascular changes is quite complex.

The quantity and time course of edema formation are based not only on the local capillary and interstitial changes but also on the general status of the vascular space [85], [92]–[95]. Carvajal et al reported that peak burn edema formation after a 10% partial thickness burn occurred at about 3 hours, whereas after a 40% burn, peak edema did not occur until after 12 hours [90]. The total edema usually is less after the larger burn, likely due to the tremendous intravascular volume depletion, which occurs after the larger burn; decreased blood volume and blood flow to the burned tissue results in less edema.

The rate of edema formation is very rapid. Using the noninvasive photon scanning technique, it has been reported that most (90%) of the edema was present by 4 hours after a partial thickness limb burn [80]. The maximum value was present at 12 hours **(Figure 2-11**) [64]. After 12 hours, the rate of production was matched by the rate of fluid clearance. However, this early plateau does not suggest that edema is not continuing to form. In fact, the models using lymph flow indicate that the increased fluid flux persists for several days as does the increased protein permeability. Clearance rate then appears to keeps up with fluid deposition.

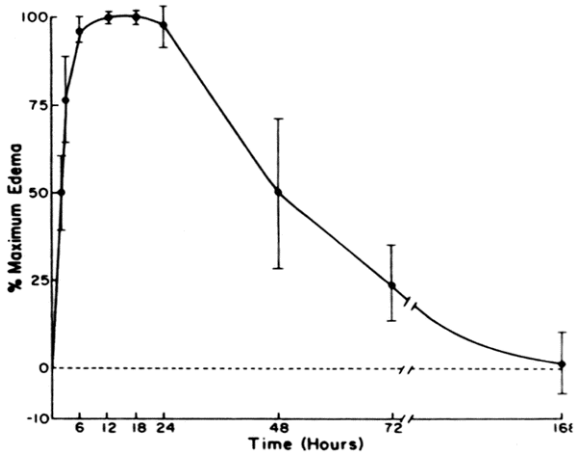

Figure 2-11: Edema formation in a partial thickness burn. Edema is measured by photon scanning. Time course of edema formation and resorption in 10 hind limbs with a partial-thickness burn is shown, comparing mean ± SD of percent fluid content over baseline against time after burn. Maximum edema is present between 12 and 18 hours, with 94% of edema present at 6 hours. Resorption began at 24 hours and is nearly complete by 4 days [64].

Edema occurs much faster in partial thickness compared to full thickness burns, likely due to better vascular perfusion in more superficial burns. In addition, peak edema is greater in partial versus full thickness burns likely due to the same reason; dermal perfusion is markedly decreased in a deep burn. The rate of edema resorption is also much faster after a partial vs a full thickness burn **(Figure 2-12).** Fluid is sequestered in the subdermal space with a deep burn

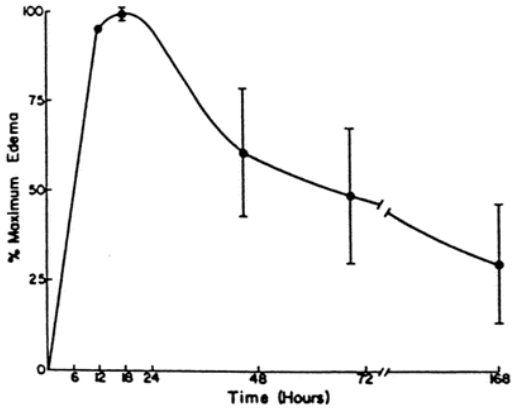

Figure 2-12: Edema formation in deep burn. Time course of edema formation and resorption is shown in 10 hind limb full-thickness burns comparing mean ± SD of percent change in fluid content over baseline against time after burn. Maximum edema occurs at 18 hours after burn inury. Resorption began at 24 hours, and but 25% still remained at 1 week. Resorption is delayed compared with that of a partial thickness burn [64].

and reabsorption is slower than from the dermis as fewer lymphatics are present; dermal lymphatics are destroyed with a deeper burn wound, impairing resorption.

Many have reported a biphasic pattern of edema formation with an immediate increase in fluid flux and edema followed by a second increase, 10-fold greater in magnitude, peaking at 1 to 2 hours and quickly reaching a plateau [84], [96]. These observations correspond with the pathophysiologic changes that are reported to occur. The initial response is likely caused by a marked negative interstitial pressure caused by the release of osmotically active particles. The addition of increased capillary permeability and then the interstitial compliance changes, perpetuate the process [64].

Although the edema process is responsible for the burn patient's large fluid needs during resuscitation and also for local problems, such as a compartment syndrome, there have been no effective modalities introduced into clinical care to accurately assess the degree of edema.

2.4.6 Edema Assessment

One of the major obstacles to improving our knowledge of the pathophysiology of burn edema has been the difficulty in accurately quantifying the edema process. Quantification is essential for the study of edema formation and resorption and, in particular, for the evaluation of therapeutic methods to decrease or prevent edema formation. The vast majority of studies on burn edema are performed in experimental animals because of the lack of noninvasive techniques to quantify clinical edema. The most common techniques being used in these experimental studies are listed in **Table 2** [64].

Table 2: METHODS FOR MEASURING BURN EDEMA [64]

• Tissue lymph flow and lymph protein content
• Tissue biopsy for histology
• Tissue water measured by wet to dry
• Photon Scanning
• Radioisotope distribution
• Plethysmography
• Fluid requirements and changes in body weight

The most common method for evaluating edema is by clinical examination, during which

tissue swelling and turgor are routinely examined. This technique, however, requires considerable clinical expertise and is very difficult to assess, if possible, when deeper tissues are involved.

Lymph flow rate and lymph protein content have been used frequently to monitor microvascular fluid filtration rate and protein permeability characteristics [97]–[99]. Lymph flow rate reflects the degree of fluid flux or transport across the capillary at any given moment, as the lymph channels open very close to the capillary interstitium. Many investigators have used various lymph preparations for the study of burn edema. Lymph flow appears to be a valid means of accurately monitoring partial thickness burns, or non-burned tissue, where capillaries and lymphatics remain patent. Capillary or microvascular occlusion, with a deeper burn, decreases the perfusion of the burn tissue. Therefore, less fluid is likely to enter the interstitium and into local lymphatics. In addition, lymphatic damage will occur, decreasing the efficiency of the lymphatic network. The measured lymph flow rate in deep burns is likely to underestimate the actual degree of injury and the actual edema formation in deeper burns although lymph flow will still be significantly increased above normal.

Serial skin and soft tissue biopsies that measure edema by the wet-to-dry weight are commonly used techniques for quantifying burn edema. Because of the potential for sampling error, this technique must be used with extreme care. It appears to be very important, in animal studies using deep burns, that the superficial muscle, the panniculus carnosus layer beneath the skin, be included in the biopsy sample, because much of the edema is found between this layer and the dermis [90], [91], [100]. The invasive nature of this technique makes it impractical for clinical research.

Plethysmography is a technique used for measuring changes in volume of the body or parts of the body like a limb. Several investigators have used volume plethysmography for measuring burn edema in an extremity. Although the method appears sensitive for measuring changes in total volume, changes in blood volume cannot be distinguished from tissue edema [101].

The quantification of permeability changes can be made by using radioactive macromolecules, such as 131I albumin [102], [103]. Leakage rate to the interstitium reflects the degree of capillary permeability.

Some clinical studies have used the total fluid requirements, during resuscitation, and weight gain as measures of edema. This is not a very accurate method of studying the pathophysiology of edema formation. Given the need for a clinically acceptable, non-invasive, and accurate technique for detecting edema, *imaging* tissue water content (TWC) -the direct indicator of edema- could provide useful spatiotemporal diagnostic and prognostic information not only for burns but also tissue flaps, clinically used for treating skin wounds.

.

2.5 TISSUE FLAPS

2.5.1 Epidemiology

Accurate and early prediction of tissue viability is the most significant determinant of tissue flap survival in reconstructive surgery. As seen in burns, perturbation in TWC is a generic component of the tissue response to such surgeries, and, therefore, may be an important

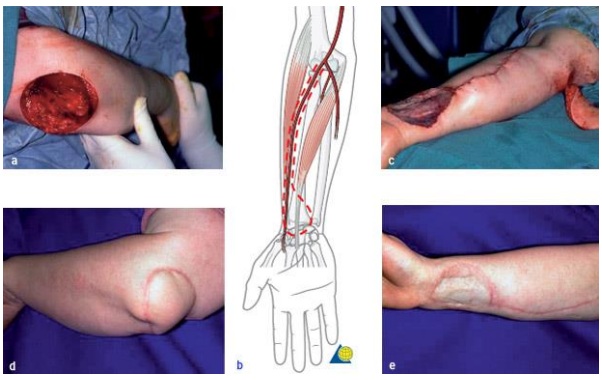

Figure 2-13: Skin flap surgery [104]

diagnostic target for assessing the extent of flap viability *in vivo*.

Tissue “flaps” have become essential for the surgical reconstruction of patients with breast

cancer, head and neck cancer, large soft tissue defects, and wounds [105], [106]. A flap includes the harvested skin, muscle, soft tissue or bone, and their corresponding neurovascular supply. As shown in **Figure 2-13**, this tissue is surgically resected and rotated or transferred from a donor site to a recipient site [107]. Patency of the underlying arteries and veins is vital for flap survival. In cases of vascular occlusion (i.e. thrombosis), flap outcome directly correlates with the rapid restoration of the vessels' patency; if reduced viability can be identified before 6 hr of thrombosis onset, which typically occurs within 72 hr following surgery, 60 - 73% of compromised flaps may be salvaged [108], [109]. Socioeconomic impacts of this result are widespread, including lengthened duration of hospitalization, increased costs, and reoperation in 6% - 25% of patients [106], [110], [111].

2.5.2 Current Flap Assessment

The current gold standard for determining flap viability is clinical examination, in which skin color, capillary refill, turgor, and bleeding patterns are periodically examined [105], [107], [112]. This method, however, is highly operator-dependent, and changes in the appearance of the flap due to microvascular complications are generally delayed by 1 to 2 hours, thus preventing early intervention [107]. Efforts towards achieving more non-invasive and accurate tissue viability measurements have been widespread and include the use of several adjunctive technologies.

One such method is fluorescent angiography that uses exogenous fluorophores to measure tissue perfusion in flaps [113], [114]. Because of physiological shortcomings associated with the tracer substance, specifically a long half-life and diffusion into the interstitium, repeated assessments consistent with current clinical monitoring practice are difficult [113]. Near-infrared diffuse reflectance spectroscopy and visible light spectroscopy have both been investigated for assessing tissue viability by measuring hemoglobin oxygenation and hemoglobin concentration [115]. However, these are all one-point measurements subject to excessive sampling error and are, therefore, not suited to monitor large flap areas. Since the chances of recovery after occlusion

are directly proportional to the rapidity of diagnosis of the entire flap area, rapid, non-invasive *imaging* of a physiological indicator of tissue viability may be more appropriate for flap assessment.

Among the available flap imaging techniques, such as laser Doppler imaging, variation in tissue water content (TWC) - an acute manifestation of injury as well as a significant parameter in the evaluation of skin health- is a major confounder to measurement of flap perfusion during the acute phase following surgery [3], [54], [116]. Early evidence suggests that visualization of TWC changes in superficial tissues may be possible with THz imaging [6], [7], [13].

2.6 THz GENERATION AND DETECTION

The THz system described in this thesis generates pulsed THz radiation with a mode locked laser and photoconductive switch, detects the reflected radiation with a waveguide mounted, 0-bias Schottky diode detector, and operates in the frequency band of ~ 400 GHz - 700 GHz. The motivation for this particular approach is outlined in the following sections and **Chapter 3**.

2.6.1 Active vs. Passive

Among THz imagers, a common distinction is made between passive systems, that measure thermally generated radiation from an object, and active systems that record the contrast in the transmitted, reflected, or scattered radiance from an object when it is illuminated with some type of THz source. The advantages of a passive imaging system are its simplicity – no illumination source is required. However, the total radiated optical power is low and substantially smaller than the thermal energy at room temperature, resulting in noise. Consequently, detectors for passive imaging have to be highly sensitive and with low thermal noise; the steep responsivity and cryogenic operation of superconducting sensors detection systems fulfill these requirements but precludes their use for medical imaging at room temperature. For this reason, passive THz imaging methods have had most success in space, where the detector can be mounted on a satellite, away from the strong thermal background that exits on Earth and directed solely at the

target of interest. The purpose of using active illumination sources is primarily to make the signal-to-noise ratio better. This is analogous to using a flash on a standard optical light camera when the ambient lighting level is too low. Active imaging systems can used pulsed or continuous wave (CW) illumination. Further, one commonly subdivides active systems into those with ranging capability (i.e. radars) and those without it. The latter generally record the total intensity of the scattered radiance, and are termed amplitude-only, active imagers. The great advantage of any active imager, whether ranging or not, is the fact that active illumination greatly reduces the sensitivity requirement on the THz receivers. Many of the most practical imagers developed to date rely on this advantage, by trading receiver sensitivity for other practical benefits such as acquisition speed, format (i.e. number of image pixels), and cost. The pros and cons of both schemes are compared in **Table 3** [117]. A notable characteristic of active imaging is that, if the illuminator produces highly coherent radiation, the scattered waves from the object interfere with each other, and subsequently create coherent artifacts in its image. Despite the complexity associated with image contrast, the aforementioned advantages of active THz imaging make it the best option for *in vivo* medical imaging

Table 3: PROS AND CONS OF ACTIVE AND PASSIVE IMAGING [117]

	Active Imaging	Passive Imaging
Detector sensitivity	Low	High
Sensitivity to environment	Relatively low	High
Detection range	Limited by source-object distance	Relatively long
Image interpretation	Difficult due to coherent artifacts	Easy
Covert operation	No	Yes
Safety concern	None based on testing	No

2.6.2 THz Sources and Detection Schemes

While narrowband THz sources are crucial for high-resolution spectroscopy applications, broadband THz sources are more important for high-speed *in vivo* imaging, and, therefore, are the focus of this thesis. Photoconduction and optical rectification are two of the most common approaches for generating broadband pulsed THz beams [118]. The photoconductive approach

involves creating carriers, termed electron-hole pairs, in a semi-conductor material using an ultrafast laser pulse. Under an electric field, these free carriers accelerate and form a transient photocurrent. Rapid photocurrent rise and decay times are responsible for radiating electromagnetic waves in the THz frequency band. Typical photoconductors include high-resistivity GaAs, InP, and radiation-damaged silicon wafers. Metallic electrodes are typically patterned onto the semiconductor substrate to bias the photoconductive gap and form an antenna. The laser pulse is most commonly provided by femtosecond lasers, such as the Ti:sapphire laser, which is characterized by short enough wavelengths to excite electrons across the antenna gaps. Photoconductive emitters are capable of relatively large average THz powers in excess of 40 μW and bandwidths as high as 4 THz [119], [120].

Optical rectification is an alternative mechanism for pulsed THz generation, and is based on the inverse process of the electro-optic effect [121]. Similar to photoconductive techniques, femtosecond laser pulses are required. These ultrafast laser pulses pass through an optically nonlinear material, which undergoes polarization at high optical intensities. In contrast to photoconducting elements, where the optical beam functions as a trigger, the energy of the THz radiation in optical rectification comes directly from the exciting laser pulse. In other words, no bias voltage is applied. The conversion efficiency in optical rectification depends on the material's nonlinear coefficient and the phase-matching conditions. Optical rectification relies on coupling of the incident optical power to THz frequencies at relatively low efficiency, which, in turn, provides lower output powers than photoconductive antennas. For this reason, the THz system used in this thesis is based on a photoconductive source element.

THz sensors range from superconductor bolometers to heterodyne sensors. Coherent detectors are best suited for biomedical imaging and spectroscopy. The two most commonly used schemes for coherent detection are photoconductive detection and electro-optical sampling. Both detection schemes involve mixing the THz pulse with a part of the original laser pulse. An optical delay line ensures the simultaneous arrival of both pulses.

In photoconductive detection, photoconductive antennas are generally used in conjunction with photoconductive sources. A bias voltage is applied to the antenna, which creates an electric field that, in turn, gives rise to a transient current. This current is amplified and the detected current is representative of the THz field strength. In electro-optical sampling, coupling between a low frequency electric field (THz pulse) and a laser beam (optical pulse) is introduced in the sensor crystal. The change in the optical polarization of the detection pulse caused by bifringence is proportional to the electric field strength of THz. Polarization of the optical probe beam can be further analyzed to provide information on both amplitude and phase of the applied electric field.

2.6.2.1 Pulsed THz Systems vs Continuous Wave THz Systems

Terahertz pulsed imaging and spectroscopy has been widely used for biomedical applications. Terahertz pulsed systems are comprised of a femtosecond laser, THz source, pair of optical transducers, and a detector (**Figure 2-14**). The laser pulse is split into two components – pump and probe. The pump is used to excite the THz source, which is typically either a photoconductive antenna or a non-linear crystal. Using parabolic mirrors, the generated THz pulse is focused onto a target and the reflected beam is collimated and focused into a detector where it is mixed with the laser probe beam. The signal is then amplified, down converted to radio frequency range, and detected. Pulsed THz systems are characterized by both large bandwidths and high signal-to-noise ratios (SNR) and provide depth information.

Unlike pulsed THz imaging, continuous wave (CW) imaging only yields intensity data and does not provide any depth, frequency-domain or time-domain information about the subject when a fixed-frequency source and a single detector are used. In exchange for the loss of depth, time-domain and frequency-domain information, CW imaging affords a compact, simple, fast and relatively low-cost system. Since it does not require a pump– probe system, the complexity of the optics involved can be greatly reduced compared to a pulsed THz system. Furthermore, it does

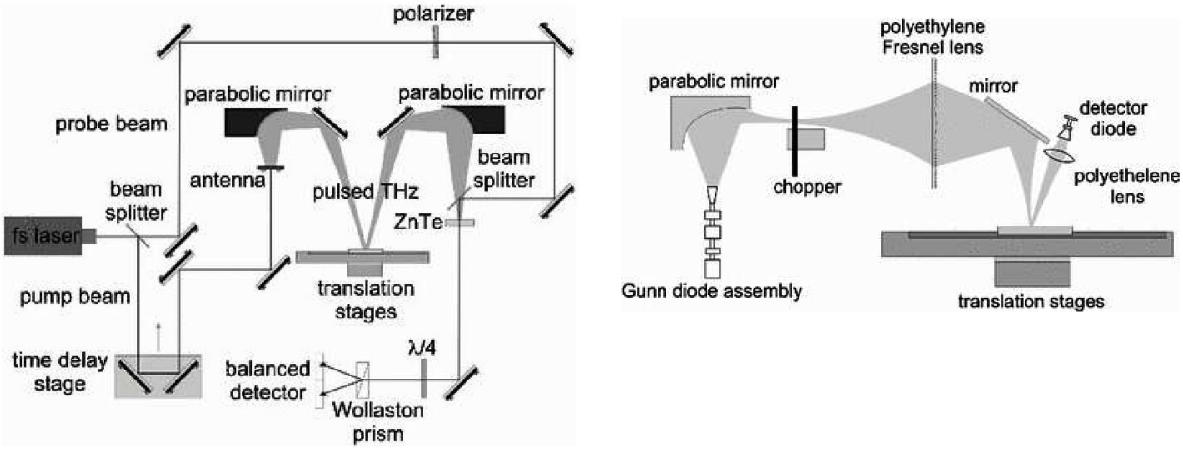

Figure 2-14: Schematic of (left) Pulsed THz imaging system and (right) continuous wave THz imaging system [122].

not require a time delay scan, and, therefore, image formation can take place more quickly. In CW THz imaging, two tunable laser sources operating at different wavelengths are photomixed to generate THz radiation (**Figure 2-14**) [122]. By selecting the operating wavelengths and line widths of the two lasers, the desired frequency in the THz range can be generated. The resultant THz waves have a higher spectral power density at a particular frequency as compared to pulsed generated waves. CW imaging and spectroscopy is best suited for applications requiring resolution of narrow spectral details like molecular signatures. However for biomedical imaging, pulsed systems are preferred since they furnish depth information and broad spectral details.

2.6.3 Why Not Time Domain?

The motivation to not pursue time domain THz imaging necessitates a basic understanding of the system architecture. A typical reflective time domain system is illustrated in **Figure 2-15** [13].

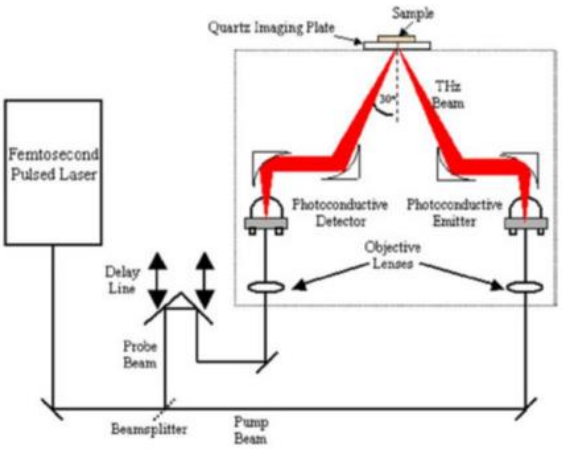

Figure 2-15: THz time domain imaging system block diagram [13]

The receiver and transmitter are usually identical photoconductive switches. A femtosecond pulsed 780 nm laser is split into two arms: 1) a pump beam, which is sent to a biased photoconductive emitter; and 2) a probe beam, which is passed through a variable delay line and then sent to an unbiased photoconductive detector. The biased photoconductive emitter generates THz radiation which is directed to the target and then back to photoconductive detector. The probe pulse modulates the resistance of the photoconductive detector switch for a very short time, allowing optoelectronic sampling of the electric field of the incoming THz pulse in the form of a photo current. The optical delay line is then swept and the entire pulse is sampled as a function of delay line position and hence time. The advantages of this architecture lie in the large amount of data (complex spectrum) that can be acquired per-pixel, which makes this scheme ideal for hyperspectral imaging. However, key disadvantages lie in complexity and image acquisition time. Furthermore, many parts of the lower and higher power spectrum are often not used as this frequency content either blurs the image or is deemed unnecessary. This time intensive approach, though acceptable for research investigations, is clinically impractical.

CHAPTER 3: THz SYSTEM DESIGN

3.1 PHOTOCONDUCTIVE SWITCH

The reflective THz imaging system currently deployed at UCLA employs a photoconductive switch as the source for THz radiation. Photoconductive switches are the most commonly used devices for the generation of broadband THz radiation in a myriad of applications, including THz imaging and spectroscopy [118], [123]. Although not deemed the most powerful of available sources, photoconductive switches demonstrate the highest conversion efficiency amongst conversion and down conversion techniques [124]–[127]. Improvements in their performance are largely attributed to the advent of low-temperature-grown GaAs. GaAs is now the most popular choice for photoconductors due to its high carrier mobility, high breakdown field, and high resistivity [118]. The addition of a composite film of ErAs particles in the semi-insulating GaAs substrate (ErAs:GaAs) further decreases the photocarrier lifetime and increase the breakdown voltage as well as provides a high resistivity necessary for THz generation and propagation. When pumped by a 780 nm laser pulse, the photoconductive switch takes the form of current flowing between the bias pads generated by a bias voltage, and, in turn, gives rise to broadband THz radiation.

The material structure of the photoconductive switch is shown in **Figure 3-1**. The switch is grown on a semi-insulating GaAs substrate starting with an AlAs:AlGaAs reflector and an AlAs heat spreader. This is overlaid with a thin photoconductive carrier generation region comprised of a single-crystal ErAs nanoparticles in GaAs via molecular beam epitaxy (MBE). A gold, square spiral antenna and bias pads are patterned atop the active region and capped with silicon nitride to protect the device from oxidation and provide an anti-reflection coating. The antenna structure serves to effectively radiate THz current into free space once it has been generated in the photoconductive gap.

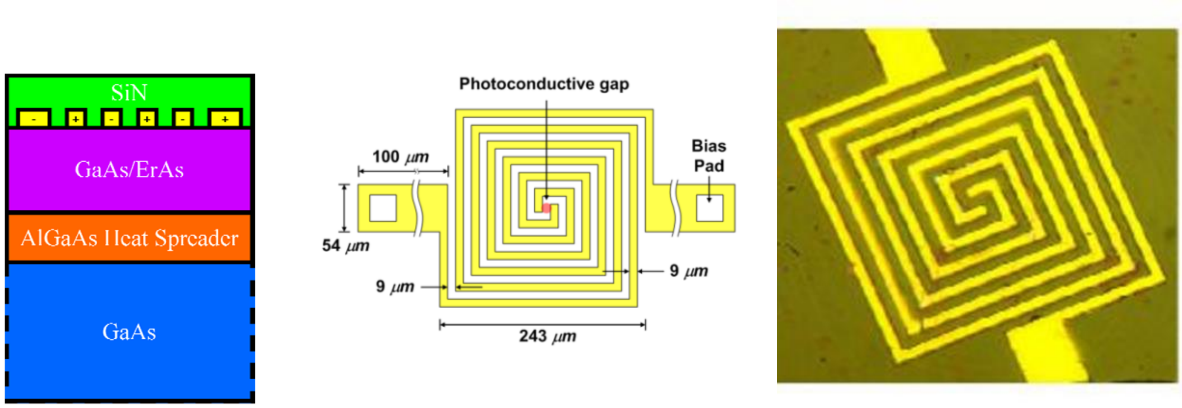

Figure 3-1: (Left) Material structure of photoconductive THz source. (Center) Schematic of square spiral antenna Block diagram of the square spiral antenna patterned atop the photoconductive material. (Right) Image of spiral antenna under a microscope.

The unit cell of the THz source measures 9μm x 9 μm with a 9 μm gap between each adjacent arm. The square spiral acts like a sequence of progressively longer dipoles that results in a high driving point resistance across a large bandwidth and good coupling to the high impedence photoconductive gap. At the termination of the three-turn spiral arms are two bias lines extending 540 μm end to end. The 48 μm width of these lines is wide enough for wire bonding and electrical biasing and has negligible effect on antenna performance. A Golay cell with an optical sensitivity of ~ 10 mV/μW and a specific optical Noise Equivalent Power (NEP) of ~ $2x10^{-10}$ $W/Hz^{1/2}$ at a chopped frequency of 16 Hz is used to perform power measurements. At high DC-bias fields (200 V/9 m gap 222 kV/cm) the source produces an optical to quasioptical (THz) conversion efficiency of 1% yielding average powers of up to 46 uW across 1 THz of bandwidth.

3.2 REFLECTIVE THz IMAGING SYSTEM

Constraints of efficient and practical *in vivo* THz imaging include clinically feasible system geometries, sufficient spatial resolutions, and rapid acquisition rates. Here, it is also important to note that transmission imaging, for obvious reasons, can only be carried out *in vitro*, whereas a reflection geometry set-up allows the possibility of *in vivo* imaging. These considerations have been extensively reviewed in the design and implementation of our novel reflective THz imaging

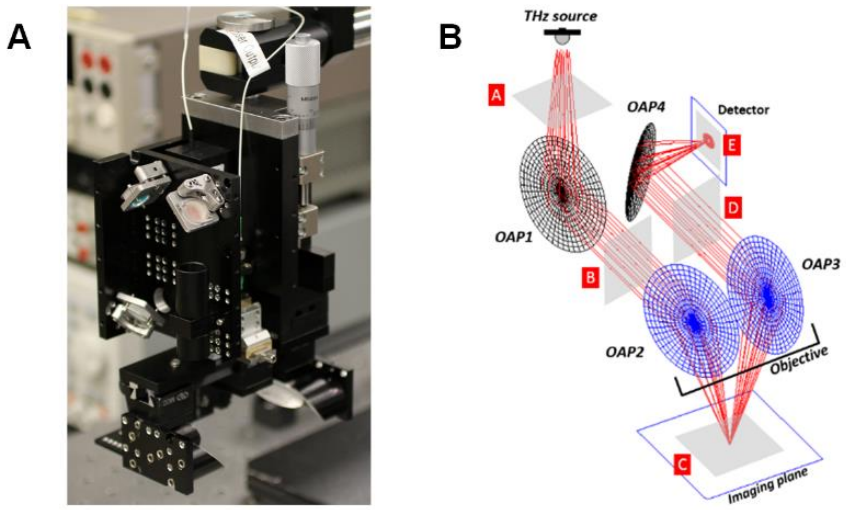

Figure 3-2: In vivo THz imaging system. (a) Visible image of the THz TWC burn imaging system currently deployed at UCLA. (b) Ray diagram of the THz optics and reciever compoenents.

device. A photograph and ray diagram of this THz imager are shown in Figure 3-2**(a)** and Figure 3-2**(b),** respectively.

The THz source, receiver electronics, and system design have been previously reported and are, therefore, summarized below [6], [9], [128]–[134]. The THz system operates in reflection mode at 0.5 THz with ~125 GHz bandwidth. The motivation for selecting this operating frequency is extensively detailed in **Section 3.3**. The photoconductive switch (PCS) based THz source is pumped by a 780 nm pulse train created by a frequency-doubled 1550 nm mode-locked laser with a 230 fs pulse width and 20 MHz repetition frequency. The PCS is mounted on the back side of a high resistivity silicon hyper-hemisphere for the free-space output. The resulting THz source beam is collimated by a 76.2 mm effective focal length (EFL), 25.4 mm clear aperture off-axis 90° parabolic (OAP) mirror. This system employs a novel THz reflective objective where 2 identical OAP mirrors are mounted such that their clear apertures normal vectors are parallel and their focal spots overlap. This objective takes in a collimated source beam and focuses the THz on target, collects the diverging reflection, and outputs a collimated beam towards the detector optics. A front on view of the geometry is displayed in **Figure 3-3,** where f_m is the mirror effective focal length (EFL) and w_d the working distance of the objective assembly. Through clever design

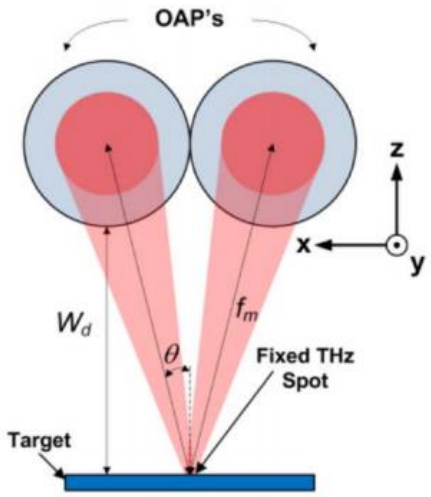

Figure 3-3: Illumination geometry. The incidence angle and working distance are functions of the OAP focal length and clear aperture [6].

and machining the system in **Figure 3-2** is equipped with the arguably the first ever THz objective which allow OAPs of varying EFL to be changed without needing to realign the THz beam.

For all *in vivo* THz imaging, a 50.8 mm EFL OAP objective mirror at a 14° incidence angle is used to focus the beam onto the target. The reflected THz radiation is then collected and collimated by a second 50.8 mm EFL OAP. Finally, a 25.4 mm EFL OAP couples the collected signal to the feedhorn of a WR1.5 waveguide mounted Zero-bias Schottky diode detector (ZBSD). Waveguide mounted, ZBSD are convenient detectors in the THz regime as these devices offer high room temperature responsivity (1000 V/W), low NEP (100 pW/Hz), and extremely broad video bandwidth (1–14 GHz). THz pulses are detected and rectified by the ZBSD. Resulting THz signals are coupled to a gated receiver referenced to split the original optical pulses, that are detected with a 1550-nm high-speed photodiode. The THz imaging system acquires pixel-by-pixel data with a 1 ms integration time. The THz image is generated by raster scanning the region of interest beneath a fixed, focused THz beam using x and y stepper motors. An image with a 6 cm x 6 cm FOV and 0.5mm isotropic resolution can be acquired in ~10 min.

System characterization studies have shown that this particular system architecture yields an effective THz operational band and only requires few optical components [6]. This simple

design minimizes laser alignment and down-converts the THz signal to baseband immediately, rendering the system more robust to misalignment. The overall compact size (12 cm x 10 cm x 8 cm) of the THz imager and the robust optical layout improves the portability of the system and enables reliable operation in both animal operating suites, and future clinical settings.

3.3 OPTICAL CHARACTERIZATION

Spot size and depth of focus measurements of a 2'' focal length mirror (most commonly used in our THz imaging studies) and all available EFLs (1'', 2'', and 3'') are displayed on the left and right in **Figure 3-4** respectively. The spot was measured using a knife edge target with the

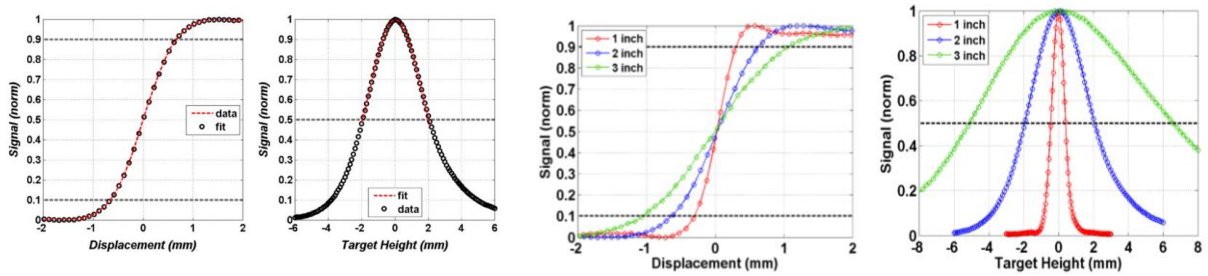

Figure 3-4: (left) Optical characterization of 2'' EFL parabolic mirror. Knife response of the spot size on target measured along the x-axis. Depth of focus limited by the optical properties of the mirrors and feedhorn directivity. (Right) Spot size and depth of focus measurements of 1'', 2'', and 3'' EFL OAPs [6].

edge swept through the beam (in the x-direction), and is defined with the standard 10–90 edge response criteria. The data follows the fit (dotted line) predicted by the 2D integration of TEM Gaussian beam and yields a 10–90 dimension of 1.1 mm for a 2'' EFL mirror. The depth of focus (DOF) was measured by translating a polished metal reflector in and out of the focal plane and the OAP EFLs and measures a total of 4 mm full width at half maximum (FWHM) for a 2'' EFL mirror. Superimposed on the data is a Gaussian fit whose shape is predicted by Gaussian beam transverse mode matching. A slight asymmetry about the maximum is visible in **Fig. 3-5** and is due to unequal beam walk off as the target is moved above and below the focal plane. The DOF is limited primarily by the optics of the system and not the pulse multiplication of the receiver. The delay line was manually scanned at the extremum of the DOF sweep and found to have minimal

effect on the synchronicity of the rectified THz pulse and reference pulse. **Table 4** summarizes the parameters of the 3 OAP THz objectives and their predicted 10% - 90% THz spot sizes.

Table 4: OPTICAL CHARACTERIZATION OF THZ OAPS

OAP EFL (mm)	W_d	*Θ (deg)*	*10-90% Spot Size (mm)*	*DOF (mm)*
25.4	9.3	30	0.8	0.8
50.8	36.5	14	1.5	4
76.2	62.4	9	2.5	11.7

3.4 THE 400 – 700 GHz FREQUENCY BAND

The effective center frequency and bandwidth of the system are constrained by the switch power spectral density (PSD) the detector spectral responsivity. The normalized power spectral density of the photoconductive switch is displayed in **Figure 3-6** superimposed on the normalized Schottky diode spectral responsivity. The switch spectrum was acquired with a Fourier Transform

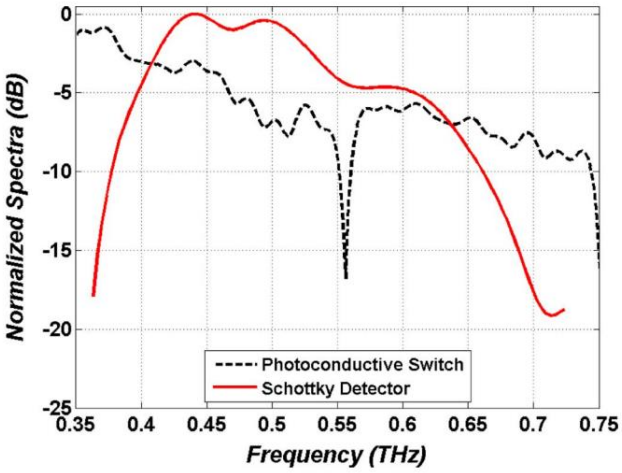

Figure 3-6: THz imaging system spectra. The dotted (black) line is the normalized photoconductive switch power spectral density. The solid line (red) is the Schottky diode normalized spectral responsivity. The response peaks at 440 GHz and the total width reflects the operational band of a WR1.5 waveguide [6].

Infrared (FTIR) spectrometer and He-cooled composite bolometer. The detector spectral responsivity was measured with a THz photomixing setup. A center frequency of 525 GHz with 125 GHz of 3 dB bandwidth is observed. As detailed below, this bandwidth is sufficient to overcome speckle from standing waves between the source and detector as well as provides

sensitivity to changes in water concentration and good spatial resolution.

3.4.1 Sensitivity to Water Concentration

Measurement of sensitivity to water concentration is determined by quantifying the expected change in THz tissue reflectivity for a given change in water volume fraction at a particular volume fraction. Basic calculations on hydration sensitivity can be explored using the dielectric properties of water and simple Fresnel equations [6]; it has been shown THz interaction with biological material, including skin, can be accurately described by dielectric models of water. Here, tissue is modeled as a homogenous mixture of water and biological background which is constructed as a lossless dielectric with an index of 2. For hydration concentrations of 100% (pure water), 75% (muscle tissue), and 50% (adipose tissue), reflectivity trends are displayed in **Figure 3-7** with the y-axis in units of % change in THz reflectivity per % change in water volume fraction.

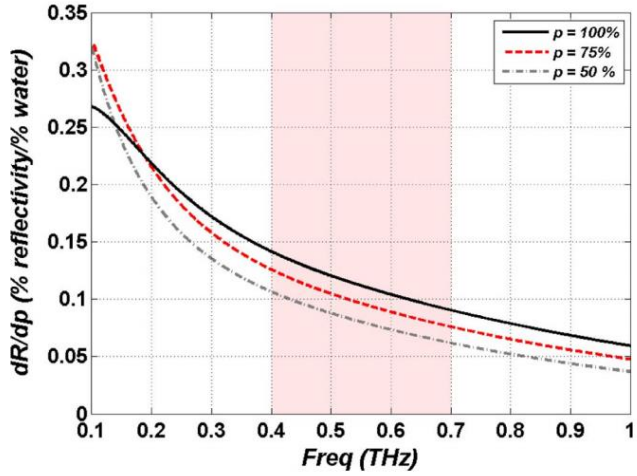

Figure 3-7: Intrinsic hydration sensitivity as a function of water concentration and illumination frequency using the double Debye dielectric model and Bruggeman effective media theory [6].

Not only does lower frequency illumination provide greater reflectivity, it also produces greater changes in reflectivity for a given change in water contrast with 6 times more sensitivity at 100 GHz as compare to 1 THz. This implies that lower frequency provides better water concentration sensitivity.

3.4.2 Scattering

Scattering from rough surfaces is a well-known problem often observed in optics. In THz medical imaging, particularly the imaging of skin, typical target feature sizes approach hundreds of micrometers, placing them directly in the middle of the wavelength bands of interest. This poses a significant problem for hydration sensing, where small changes in hydration dependent reflectivity may be masked by random scattering due to target geometry.

A common method used to model frequency dependent scattering in the THz regime is the Rayleigh roughness factor. As expected, lower frequencies are much more robust to scattering than higher frequencies, and tissues appear more specular in the millimeter wave range than they do in the sub-millimeter (**Figure 3-8**).

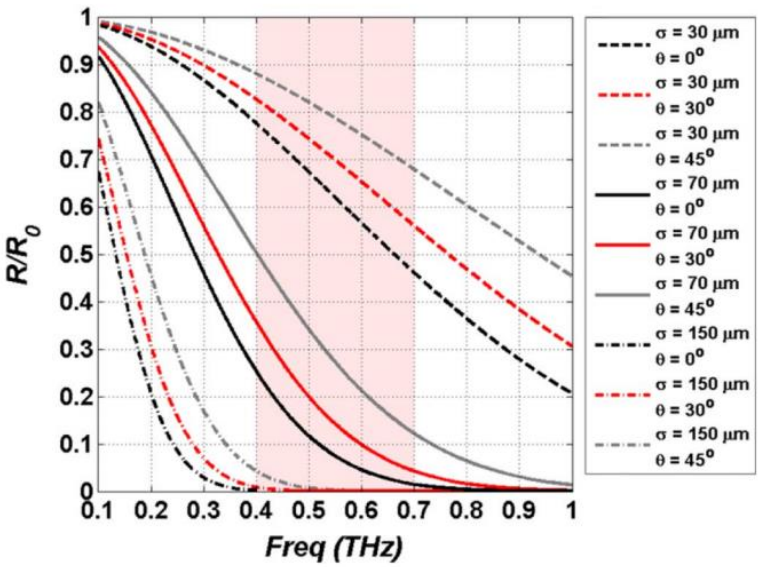

Figure 3-8: Simulation of Rayleigh scattering for pairs of RMS surface roughness and incidence angle. Note the increase in specularity as the incidence angle increases [6].

3.4.3 Spatial Resolution

The goal in THz medical imaging is to sense small changes in hydration with some degree of spatial discrimination. Since the output of most THz sources can be approximated with a Gaussian beam, theoretical spatial resolution limits can be calculated using Gaussian beam

theory. A high numerical aperture, 25.4 mm effective focal length off-axis parabolic mirror with a 25.4 mm clear aperture 90% filled by the THz beam is used in the simulation. This optic represents a practical upper limit on the focusing power of available reflective THz optics. The results are displayed in **Figure 3-9** and form an upper bound on THz beam focusing performance. As expected, higher frequencies produce a smaller spot size for a given optic and hence are able to resolve higher spatial frequencies.

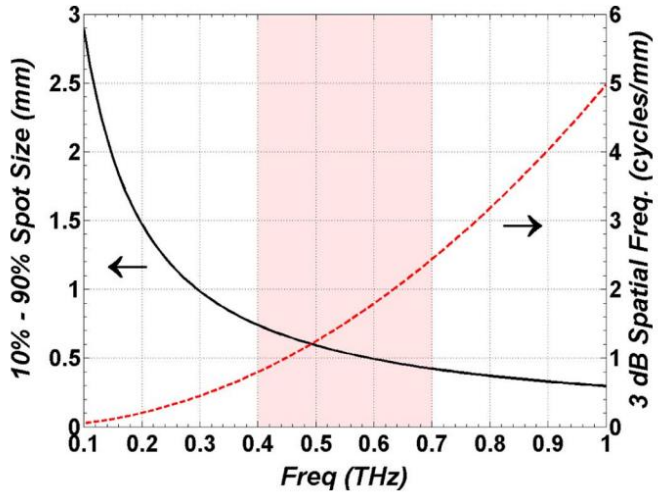

Figure 3-9: Plot of THz imaging system resolution as a function of frequency. (Left axis) spot size as a function of frequency. (Right axis) 3 dB spatial frequency cutoff in cycles per mm [6].

3.4.4 Conclusions

There are distinct tradeoffs between high and low frequencies. When developing the system design, it is imperative to choose as low a frequency band as possible while maintaining a minimum spatial resolution. The band covering 400–700 GHz offers the best compromise between scattering, sensitivity to water concentration gradients and maximum spatial resolution.

CHAPTER 4: PRELIMINARY THz BURN WOUND IMAGING

4.1 BACKGROUND

THz imaging has been gaining considerable attention among burn experts largely due to the high image contrast between burn tissue and surrounding uninjured tissue. Because significant fluid shifts follow thermal insult and the dielectric properties of water at THz frequencies (100 GHz to 10 THz range) yield easily detectable changes in THz reflectivity for small changes in hydration, TWC is largely hypothesized to be the contrast mechanism in reflective THz imaging of skin wounds [13]–[15], [133].

Concerted efforts to image wounds follow the pioneering work done with THz-TDS systems in *ex vivo* chicken skin [11], [135]. In this study, a series of circular burns of increasing severity were induced in chicken breast with an argon laser. These results are the first to report on burn tissue-THz radiation interactions and apparent THz contrast between injured and uninjured tissue. As an applications-based THz imaging lab, our group has followed their lead and published THz imagery of *ex vivo* porcine skin burns acquired in reflection [128], [136], while Dougherty presented transmission imagery of burns in chicken skin [137].

An interesting question is whether these findings can be observed *in vivo.* Over the last few years, THz imaging systems have been designed to consider system geometries, data acquisition rates, image resolution, and penetration depths that make *in vivo* THz imaging feasible [6], [22], [129], [132], [138], [138]–[143]. In 2012, we were the first in the field to publish *in vivo* THz burn imagery obtained in reflection of partial thickness burns induced in pre-clinical rat models [9]. Significant shifts in spatially varying reflectivity were observed between 8hr and 72hr following burn induction. These differences are hypothesized to be the result of the buildup and dissipation of TWC ensuing injury; segmentation profiles across high-resolution (d10–90/λ~1.925) images reveal certain wound areas experience an increase in hydration of >20% with respect to the uninjured skin, while others display a drop in hydration of up to ~10%. Arbab

et al. have published extensively on the THz spectroscopic properties of *in vivo* rat burns [10], [144]–[146]. Spectra obtained from a large rat trial fit to Double Debye electromagnetic models indicate that interstitial water buildup is primarily responsible for the change in dielectric properties between normal and full thickness burn wounds; burned tissue in rat models exhibits higher reflectivity compared to normal skin over a frequency range between 0.5 and 0.7 THz ($p < 0.05$). Additionally, the presence and absence of microstructures in uninjured and burned skin were found to have a measureable effect on THz spectra [10]. Collectively, these *in vivo* and *ex vivo* findings, though preliminary, reflect the capabilities of THz imaging as a potential tool for detecting and monitoring wounds of varying severity during the acute edematous phase of the burn response.

While these studies measured the effects of thermal injury on THz reflectivity and lay the groundwork for THz wound imaging, further, longitudinal investigations in varying wound models (partial vs. full thickness burns) of larger population sizes need to be performed to evaluate the wound discriminating and monitoring capabilities of THz imaging.

In 2013, we performed a first-of-its-kind *in vivo* THz imaging study of burn wounds in 10 rats to explore the utility of THz-TWC based maps in assessing burn wound severity. Partial thickness (130°C) and full thickness (200°C) burn wounds were induced with a previously reported protocol in the abdominal skin and reflective THz imaging was used to track the distribution of hypothesized TWC throughout the wound bed over a period of 72 hours [9]. Ideally, we aimed to translate changes in image contrast or the shapes of particular features in THz burn data into biologically meaningful terms, such as changes in physiology and anatomy in injured tissue. We hypothesized that burn injury models of varying severity would elicit different physiological responses, and therefore their respective THz-TWC maps will have unique THz image contrast. To this end, spatial-temporal variations in THz signal in partial and full thickness wounds may be useful indicators for burn assessment and physiological changes occurring over time.

4.2 PRE-CLINICAL RAT MODEL

Rats were used as an pre-clinical model for *in vivo* THz burn wound imaging [147]. There are inherent drawbacks in using rats for comparisons with human skin wound healing. Specifically, rat skin anatomy does not perfectly mimic that of human skin. Rats possess a subcutaneous panniculus carnosus muscle, which humans lack, and this muscle contributes to skin healing by both contraction and collagen formation [147]–[150]. Burn studies that employ rat models must be aware of this distinction, as it can cause a decrease in the overall healing time of rat wounds. Among the available burn wound parameters, skin thickness is most

Table 5: HUMAN AND ANIMAL SKIN THICKNESS MEASUREMENTS [148]

Type of Skin	*Stratum Corneum (μm)*	*Epidermis (μm)*	*Whole Skin (mm)*
Human	16.8 ± 0.7	46.9 ± 2.3	2.97 ± 0.28
Pig	26.4 ± 0.4	65.8 ± 1.8	3.43 ± 0.05
Rat	18.4 ± 0.5	32.1 ± 1.3	2.09 ± 0.07
Hairless mouse	8.9 ± 0.4	28.6 ± 0.9	0.70 ± 0.02
Mouse	5.8 ± 0.3	12.6 ± 0.8	0.84 ± 0.02

pertinent for understanding the wound depth as an aspect of wound healing. The thicknesses of rat and human skin layers are most similar compared to those of other animal skin (**Table 5**), and therefore rats are frequently used as cutaneous injury models [151]–[154]; entering the terms *skin, wound healing models,* and *rats* in the scientific search engine of the National library of Medicine, Pub Med, returns 198 articles, 67 of which have been published after 2000 [147]. In addition to the availability of a broad knowledge base on rat wound healing, rats are readily available, inexpensive, and easy to manage. Lastly, large numbers of these pre-clinical models can be used to achieve statistically significant measurements.

4.3 DIELECTRIC WINDOW SELECTION AND DESIGN

From a clinical vantage point, the use of windows for THz burn wound assessment is a practical barrier to non-contact, *in vivo* medical translation of this technology. Nearly all reflective

THz imaging systems employ low-less dielectric substrate windows, and these contact methods share several significant problems:

- Physical perturbation of the wound when contact is made
- Risk of contamination of the wound site
- Pressure exertion, which can affect fluid shifts as well as loss in the wound bed
- Contributions to observed electromagnetic properties of the burn tissue
- Modulation of TWC contrast in THz burn imaging

Although windowless burn wound assessment is ideal, windows are necessary in THz imaging to minimize confounding effects from surface roughness, non-planar geometries, and respiratory motion artifacts *in vivo* [155]–[157]. Both high and low dielectric substrates, including quartz, sapphire, and thin stretched Mylar film, are commonly used to flatten the imaging target [6], [14], [29], [158]–[161]. As shown in Figure 4-1, slight perturbations in THz signal are evident even with window-driven motion correction. In addition, the thickness of windows contributes substantially to the overall observed electromagnetic properties of the target of interest. Consequently, the distribution of water along the coronal axis (both in the thickness of tissue layers and the layer composition) alters the tissue's reflectivity. To explore these effects, we have previously modeled the power reflectivity of a tissue system under a window illuminated at 30° incidence angle and evaluated the response over illumination frequencies from 500 GHz – 700 GHz [6] [136], [162].

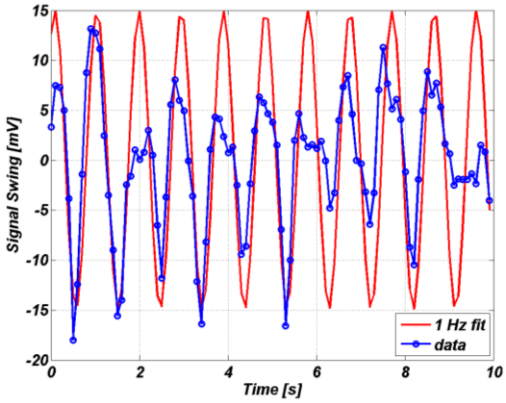

Figure 4-1: Thin flexible windows provide significant motion artifacts for time domain systems. Displacement of ~ 100 um.

Two cases were considered: a 500 µm thick Mylar window and a 12 µm thick Mylar window (**Figure 4-2**). Electromagnetic modeling predicted that the power reflectivity of a tissue system under thick Mylar illuminated at a 14° incidence angle was frequency-dependent, and, therefore, varied non-linearly with respect to increasing tissue water content.

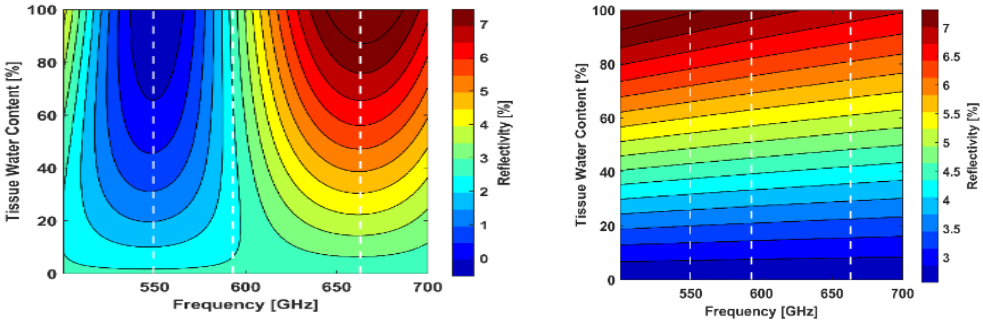

Figure 4-2: Electromagnetic models of dielectric substrates. Left: Thick 500 µm Mylar. Right: Thin 12 µm Mylar.

In other words, over the aforementioned frequency range, reflectance may vary from high-to-low or high-to-low-to-high with increasing tissue water content. Conversely, in the case of thin Mylar, a positive correlation was suggested between increases in TWC and THz reflectivity. Given that implementation of an optical window is currently necessary in THz burn imaging, a 12µm Mylar was selected to enable more predictable electromagnetic modeling behavior for in vivo burn imaging.

4.4 ELECTROMAGNETIC MODEL AND EXPECTED BEHAVIOR

Extensive work has been published on the THz properties of skin and, more recently, skin burns [6], [9], [12], [12]–[14], [29], [30], [128], [133], [144], [145], [162]–[165]. While fits between theory and experiment suggest small contributions from frequency dependent scattering, skin pigments, and physiologic variation, tissue permittivities at THz frequencies can be accurately described by dielectric functions used to capture the electromagnetic properties of liquid water. Many groups have published on the accuracy of using the double Debye model as a baseline and perturbing the relaxation time until the fit converges with the observed spectra [162], [166]–[169]. Our group has proposed employing effective media theory to compute tissue dielectric properties through the use of the estimated fill factor of water to tissue. When the tissue water content is changed by thermal insult and the subsequent physiologic response, the fill factor can be modified to compute the effective dielectric function at the tissue hydration of interest. This methodology models what is thought to occur in burn wounds and serves as a good starting point when performing system design calculations for expected reflectivity, sensitivity, etc. The methodology for simulating the frequency dependent aggregate properties of skin has been presented in prior publications [6], [167], [170]. A brief summary of this method is provided below.

The frequency dependent dielectric properties of water are captured by the Double Debye model (**equation (5)**) with the same constitutive parameters and corner frequencies (ε0, ε1, f1, f2) used in our previous work [6].

As mentioned previously, the skin is composed entirely of collagen and water which allows the implementation of a binary

$$\boldsymbol{\varepsilon_w(f) = \varepsilon_\infty + \frac{\varepsilon_0 - \varepsilon_1}{1 - j2\pi f/f_1} + \frac{\varepsilon_1 - \varepsilon_\infty}{1 - j2\pi f/f_2}} \qquad \textbf{(5)}$$

mixture Bruggeman model (**equation (6))** where ε_{bb} is the frequency invariant dielectric constant

of the non-water tissue constituents which we term biologic background (bb), ε_w is the frequency dependent dielectric constant computed with **(5),** p_w is the water volume fraction, and $\hat{\varepsilon}$ is the effective permittivity of the layer that satisfies the equivalence relation in **(6**). The water volume fractions can be adjusted to match any hypothesized distribution. Further, when tissue water content is perturbed by thermal insult and subsequent physiologic response, the fill factors can be modified to compute the change in dielectric function and overall expected change in THz reflectivity.

$$\hat{\varepsilon} \ \mathbf{s.t.} \ \ \mathbf{p}_w\left(\frac{\hat{\varepsilon}-\boldsymbol{\varepsilon}_w}{\boldsymbol{\varepsilon}_w+2\hat{\varepsilon}}\right)+(\mathbf{1}-\mathbf{p}_w)\left(\frac{\hat{\varepsilon}-\boldsymbol{\varepsilon}_{bb}}{\boldsymbol{\varepsilon}_{bb}+2\hat{\varepsilon}}\right)=\mathbf{0} \qquad \mathbf{(6)}$$

The stratified media and effective media methodologies used to simulate the THz frequency properties of skin are shown in **Figure 4-3**. To illustrate the variability of the skin electromagnetic properties, two candidate variation types were explored. **Figure 4-3(b)** contains an example of a localized TWC perturbation where the edema occurs primarily at the epidermis/dermis interface. **Figure 4-3(c)** shows an example of global variation with fixed surface hydration where the edema penetrates all the skin layers but the top surface remains intact.

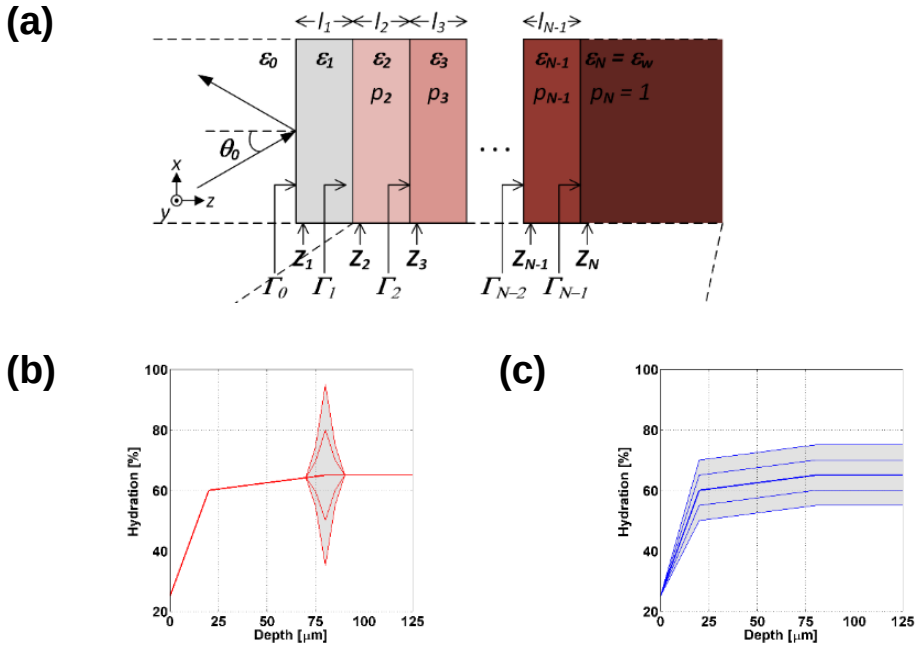

Figure 4-3:THz electromagnetic model. (a) Effective media model. (b) Localized and (c) global TWC perturbation

While researchers have hypothesized that burn wound edema is expressed in some layers more strongly than others, there is a general consensus that the TWC of all layers are effected to some degree [64], [80], [85]. This notion suggests that burn wounds experience perturbations that are some combination of the distributions in **Figure 4-3(b)** and **Figure 4-3(c)**.The effective electrical length of the layer *i* is written **(7)** where $\hat{\varepsilon}_i$ is the

$$\boldsymbol{\delta_i = \frac{2\pi}{\lambda} l_i \sqrt{\hat{\varepsilon}_i}\cos(\theta_i)} \qquad \textbf{(7)}$$

complex, effective permittivity of layer *i* computed with **(6)** and θ_i is the complex angle of refraction computed with Snell's law.For the simulations presented below the discretized layer thickness was set at ~ 10 μm where reflectivity simulation results with varying layer thicknesses converged to a differential less than 10^{-3}. Thinner layers results in insignificant increases in accuracy at the expense of increases in computational complexity.

$$\boldsymbol{\rho_i = \frac{\sqrt{\hat{\varepsilon}_{i-1}}\cos(\theta_{i-1}) - \sqrt{\hat{\varepsilon}_i}\cos(\theta_i)}{\sqrt{\hat{\varepsilon}_{i-1}}\cos(\theta_{i-1}) + \sqrt{\hat{\varepsilon}_i}\cos(\theta_i)}} \qquad \textbf{(8)}$$

$$\boldsymbol{\Gamma_i = \frac{\rho_i + \Gamma_{i+1} e^{-j2\delta_i}}{1 + \rho_i \Gamma_{i+1} e^{-j2\delta_i}}\ where\ \Gamma_N = \rho_N} \qquad \textbf{(9)}$$

The Fresnel reflection coefficient from layer *i-1* to layer *i* each interface can be written as a function of the complex effective dielectric constants and the complex refractive indexes. Note that the Fresnel coefficient has been written for TE polarization. This polarization has been shown to produce reflectivities and hydration sensitivities larger than the TM polarization for any incidence angle. The total aggregate electric field Γ reflection coefficient from layer i+1 to N is given in **(9)** where Γ_N is defined as the Fresnel coefficient between the final layer of the stratum corneum and dermis and Γ0 is the total reflection coefficient of the window covered burn wound.

For the analysis we are interested in 2 different quantities as a function of hydration and frequency; the expected reflectivity of the burn wound **(10)** and the expected change in reflectivity

per change in hydration **(11)**.

$$\boldsymbol{Power\ reflectivity} = \boldsymbol{\mathcal{R}} = |\boldsymbol{\Gamma_0}|^2 \qquad \textbf{(10)}$$

$$\boldsymbol{Hydration\ Sensitivity} = \Delta \boldsymbol{H} = \left|\frac{\boldsymbol{d\mathcal{R}}}{\boldsymbol{dp}}\right| \qquad \textbf{(11)}$$

Although significant research has been undertaken to understand the physiology of burn wounds, the depth dependent tissue hydration of burns throughout the healing process are not entirely known. This is due in part to the lack of imaging tools that are sensitive to hydration.

Simulations of the computed reflectivity over the system operational band have been performed. The key difference observed is that the global perturbation displays a positive correlation between TWC increase and THz reflectivity while the localized perturbation displays areas of positive and negative increase. In other words, increasing TWC at a particular depth can lead to a decrease in THz reflectivity.

4.5 BURN INDUCTION, IMAGING, AND HISTOLOGY

A 12.7 μm Mylar window suspended from a brass frame was lowered onto the shaved abdomen of anesthetized rats to flatten the imaging field. The THz reflectivity was maximized off animal's skin for every individual. Visible images of the uninjured abdomen were captured with a SLR camera and control scans covering a 2.5 x 2.5 cm field of view (FOV) were initiated with the THz imaging system. Image acquisition time was estimated to be ~10 minutes. The window was then removed, and a 2 mm x 19 mm rectangular brass brand secured to a thermocouple – to accurately monitor the absolute temperature- was heated to 200°C and 130°C using a hot plate, positioned between the three black circular dots on the abdomen, and manually applied with a constant pressure for 10 seconds to induce a full thickness and partial thickness burn, respectively. 5 rats received partial thickness wounds, and the remaining 5 rats received full thickness burn wounds. The Mylar window was repositioned on the burn and concomitant visible and THz imagery were continuously acquired every 15 min for the first hour and every 30 min for

the remaining 7 hrs. The Mylar window was kept stationary during continuous scanning to remove any discrepancies in z settings arising from removing the window between scans. Upon scan completion, the rat was awoken and returned to the vivarium in care fresh bedding to ensure minimum discomfort to the wound. An antibiotic, Trimethoprim-Sulfamethoxazole, was administered orally to prevent possible infection ensuing burn injury. Follow up visible and THz imagery were acquired at 24 hr, 48 hr and 72 hr post burn induction, at which point the animal was euthanized.

Three sections of skin along the rostrocaudal axis were harvested from the left, center and right regions of the burn and transferred to 10% formalin solution; these tissue specimens contained both uninjured and injured tissue, providing a control area which the burned area could be compared to. The skin samples were then submitted for histological embedding, sectioning (8 μm thickness), and staining with hematoxylin and eosin (H&E). Light microscopy was used to examine the burn slices, followed by analysis of the observed structural tissue damage to assign burn severity.

4.6 IMAGE REGISTRATION

External fiducial markers were used to align THz images to their respective visible pictures. Two triangular painter's tape pieces positioned on diametrically opposite sides of the brass frame of the Mylar window served as fiducial markers. The triangles were visible in the THz image and visible picture acquired prior to the THz scan. Additionally, the markers on the visible picture were aligned with the corresponding view on the THz images with respect to location and size of the markers. Because the Mylar window was kept stationary during continuous scanning, all THz images are registered to one another during the 7 hr period. Interpatient registration was performed by selecting the center of the burn to be the intrinsic fiducial marker. Setting the center as the point of origin, THz images across all rats were rotated and translated to line up in the same orientation.

4.7 RESULTS

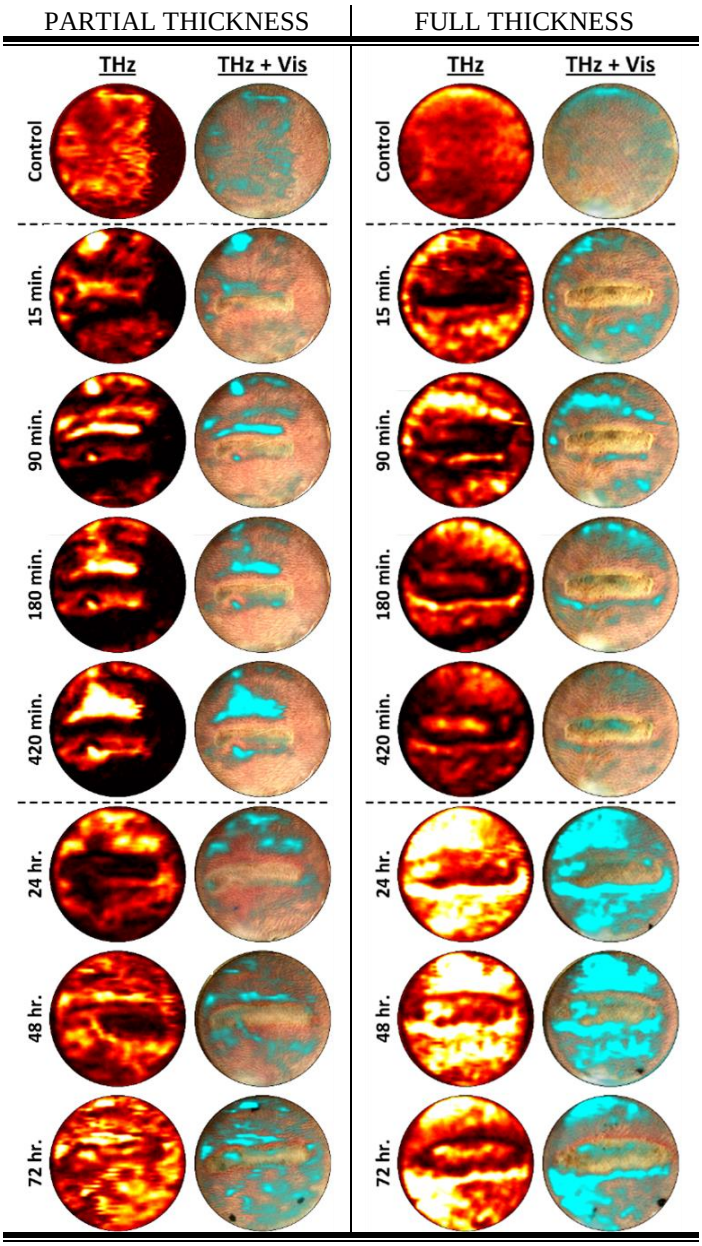

Figure 4-4: Left: Time series THz burn imagery with hot color map. Right: Superimposed THz/Visible imagery, where cyan color map denotes edema.

As shown in **Figure 4-4**, burn wounds were imaged under a thin film Mylar window, and THz images and superimposed THz-Visible images were generated using a hot color map and cyan color scale, respectively. The hot color map transforms black to the global minimum THz reflectivity and white to the global maximum THz reflectivity for all burns, and the cyan color map denotes tissue edema. For our THz imaging observations, we assume the positive correlation between water concentration increase and THz reflectivity suggested by stratified media and effective media modeling of a global perturbation in tissue water content under a thin film Mylar window. At this time, we also assumed that the dominant contrast mechanism of THz imaging was TWC and reported our findings in this context. This latter assumption, of course, would later be investigated and become the underlying topic of this dissertation.

Following burn induction, partial thickness burns demonstrate a TWC variation within the contact area and low level desiccation in the surrounding tissue while full thickness burns undergo

an overall increase in surrounding TWC and the contact region experiences a noticeable drop in TWC. High TWC levels can be ascribed to previously reported TWC increases of up to 75% in the burned tissue compared to uninjured skin that occur 30 minutes post injury. The rapid image acquisition time (~10 minutes) of THz imaging is on the same order as burn pathophysiology, and therefore enables the visualization of these immediate post burn events.

Upon visual inspection of THz imagery in **Figure 4-4**, two features are evident at the wound center: a central area enveloped by a thin annulus. These image features are first apparent by the 1.5 hr mark and are starkly visible in full thickness burns and much less visible, but still present, in partial thickness wounds. TWC of the annulus, in particular, is consistently low for longitudinal THz burn imagery in both partial and full thickness burns. The zone of stasis -the intermediate region between the central zone of devitalized tissue and the outermost zone of hyperemia- is similarly known to be characterized by low perfusion, and therefore we strongly hypothesize this ring of low TWC to correspond to this zone.

Conversely, the central wound area varies with wound severity. From 1.5 hours up to 7 hours post induction, partial thickness injuries demonstrate significant reduction of TWC in the central contact area and a significant yet somewhat localized increase in TWC in the adjacent regions. Full thickness burns also initially display increases in TWC in the adjacent tissue, however the effect is less localized and instead appears to fill the entire FOV. Furthermore, the central contact area of a full thickness wound begins to fill in and approach the TWC of the adjacent tissues. By Days 1-3, fluid redistribution resurfaces in THz imagery of both a partial and full thickness burn wound. This resorption of fluid begins ~24 hours post injury and may be responsible for the reduced contrast observed at Day 3 in the partial thickness wound.

To explore the spatial information contained in the imaging data sets, features inspired by burn wound physiology were identified and classifiers based on these features were used to delineate between burn severity groups. Burn pathophysiology is commonly characterized by three typically concentric regions; the zones of coagulation, stasis, and hyperemia, and each is

representative of tissue viability. The innermost region (coagulation) contains irreversibly damaged cells and depending on the severity of injury and damage to the vasculature. This is surrounded by the zone of stasis which is characterized by mixed viability tissue and the zone of hyperemia which contains affected but likely salvageable tissue. Accompanying these zones are local and systemic fluid shifts, with water concentrations that may vary by up to 80% within 10 minutes of the injury.

To leverage this knowledge of physiology, features consisting of orthogonal line cuts (collinear with the location tissue was harvested from for histology) and local and global annuli of constant distance from the wound center were analyzed and a classification function looking at the variation in reflectivity as the length and radius of the lines and annuli was increased was evaluated. After intermodality registration (THz image to visible), intersubject registration (animal to animal), and intrasubject registration (within the same animal) was performed, temporal and

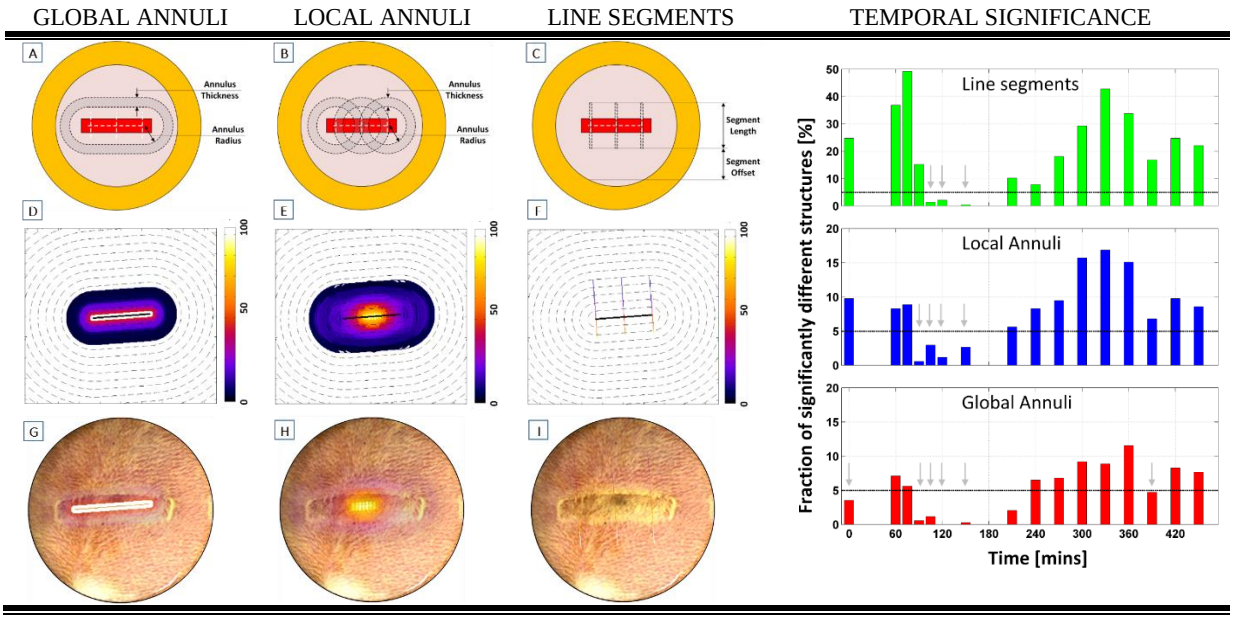

Figure 4-5: Image segmentation for (a) global annuli, (b) local annuli, and (c) line segment features for a partial and full thickness burn wound on Day 0. Spatial significance, where the number of times a pixel was included in a statistically significant feature is converted to a percentage, for (d) global annuli, (e) local annuli, and (f) line segments. THz spatial significance superimposed on co-registered visible imagery. Annuli demonstrate peak overall significance at the center while line segments demonstrate peak significance below the wound. Right: Temporal significance of the fraction of significantly different structures that pass a 5% false discovery rate.

spatial significance of the different segmentation methods was performed. As shown in **Figure 4-5,** for global and local annuli segmentation, the center of the wound is spatially significant between a partial and full thickness wound. For orthogonal line segments across a partial thickness and full thickness wound, the bottom of the wound is statistically significant. For all segmentation methods, the temporal significance of the fraction of significantly different structures that pass a 5% false discovery rate is observed within the first 2 hours following burn induction and after 4hr.

4.8 DISCUSSION AND CONCLUSIONS

Assuming that TWC is the dominant contrast mechanism underlying THz imaging, these THz burn results suggest that variations in spatiotemporal THz-TWC measurements between partial thickness and full thickness burn wounds are statistically significant when imaged under a dielectric Mylar window within the first few hours of injury. Partial thickness burns demonstrate significant decreases in TWC in the burn contact area and localized increases in TWC in the adjacent tissue. By comparison, full thickness burns display a global increase in TWC. Although these THz burn studies yielded THz TWC signatures of edema, the pathogenesis of fluid shifts secondary to thermal injury is incompletely understood and in direct contrast to clinical observations of burn-induced edema; published data on acute changes in fluid transport suggest that the accumulation of TWC in partial thickness wounds should, in fact, be greater than that in full thickness wounds [64], [80], [85]. These discrepancies stem, in part, from inherent limitations of the previous experimental methods (i.e. burn induction and image registration) and system designs used in our pilot THz imaging studies.

For example, the burn protocol required that the experimentalist manually place a heated brand on the abdominal skin of the anesthetized animal with constant contact pressure. This task proved to be difficult in practice and all the induced burn wounds were of mixed severity. The resultant THz burn maps, therefore, did not reflect unique edema pathogenesis characteristic of

either a partial thickness or full thickness burn injury. To overcome this issue, we need to integrate a precisely controlled z-stage that enables positional and pressure accuracy of the heated brand. All burn wounds induced with this technique will be histologically verified to be distinctly either uniform partial thickness or full thickness severity. This result will enable a comparative THz imaging study of wounds of definitive burn depth.

A second key improvement will be that all burn wounds must contain permanent fiducial markers, in the form of tattoo ink, that enabled accurate comparison of histological wound outcome with THz frequency reflectivity measurements acquired with different dielectric windows. In the burn study, black marks created with sharpie dots were used as fiducial markers to register images between 7hr, 24hr, 49hr, and 72hr. However, these dots disappeared by 24hr, and therefore temporal and spatial significance between partial thickness and full thickness burn wounds could only be computed for the first 7hr, when the position of the dielectric window was fixed. Because the height of the window is adjusted between scans and repositioning to the same location is difficult to perform manually, the maximum and minimum reflectivity observed for each THz image, as well as between subjects and within the same subject, may have varied significantly: the tolerance of the depth of focus for a 2'' parabolic objective mirror is ~2 mm, and, therefore, any large adjustments in the window would have changed the observed reflectivity signal.

To ensure robust and repeatable target positioning, a cartridge system allowing optical windows with different dielectric properties to be exchanged must be designed and fabricated. Windows should be able to be exchanged from a rigid aluminum mount that is positioned orthogonal to the imaging head at a fixed standoff distance. An aluminum calibration reflector must be used to track maximum THz reflectivity signal during image acquisition. The center of the cartridges will be coincident with the optical axis of the window and the standoff distance between the windows and imaging head will be identical.

Because the THz imager is repeatedly used *in vivo*, the sensitivity of the system to water

concentration and an investigation of TWC contrast in THz imaging are warranted. Once these advancements are effectively implemented, THz imaging can be used to acquire unique and reproducible *in vivo* THz-TWC maps in burn wounds and other applications. Moreover, after a confirmation of THz-TWC based contrast, these results can be confidently reported in the context of edema pathogenesis.

CHAPTER 5: SYSTEM CALIBRATION WITH PHANTOMS

5.1 MOTIVATION

Quantitative assessments of system performance measurements, specifically water concentration sensitivity, with tissue substitutes were performed. This study originated from limitations associated with previous efforts to convert THz reflection images of skin burns into hydration images using standard electromagnetic models. A calibration relation was computed from the assembly of data with known hydration concentrations and validated by comparison with three layer simulations. The model and fit was evaluated.

Previous hydration concentration sensitivity measurements of THz imaging, although statistically significant, have been acquired with non-tissue targets, including hydrated polypropylene towels, and therefore are not biologically relevant models for *in vivo* applications [162]. Non-tissue mimicking targets have been used to date, but as the applications of THz imaging become more biological in nature, hydration phantoms that closely emulate biological tissue will be required to quantify system performance measurements in the THz imaging community [171]. An ideal tissue phantom would provide physical properties equivalent to tissue and comprise its primary constituents, specifically water and protein [172], [173]. Such calibration phantoms are commonly used in radiation therapy, computed tomography (CT), and ultrasound imaging, but have not yet been developed for reflective THz imaging [173], [174].

A review of the literature suggests that phantom studies using THz illumination have primarily been investigated with absorptive THz imaging [172], [175], [176]. The THz spectra of phantoms composed of naphtol green dye mixed with distilled water and TX151 gels have been measured, however, the refractive indices of these phantoms vary significantly from those observed in tissue, limiting their utility as biological tissue targets [177]. Studies of hydrated myoglobin powders and protein gel films present a more biologically relevant analysis, however,

these samples are partially hydrated and fail to reproduce the true biological condition of tissue [178].

Gelatin, widely known to be inexpensive and easy to prepare, has been frequently used to fabricate *in vivo* models in medical imaging studies and was selected to be the protein agent for this hydration phantom [179].

5.2 MATERIALS & METHODS

5.2.1 Phantom Mount Design

As illustrated in **Figure 5-1**, custom mount configurations were designed with a transparent window to isolate hydration contrast from all other features of the phantoms, including surface topography, curvature, and the standoff distance between the sample and imaging head. In all three design configurations, tissue phantoms were pressed against a fixed, transparent quartz, imaging window (Meller Optics, Providence, Rhode Island) to allow for a constrained, tangential geometry of the samples over the course of the image acquisition period [8]. Maintaining a constant standoff distance is of particular importance to overcome both the surface features within a sample and those between neighboring samples. The quartz window is housed in a 76 mm diameter lens mount (Thorlabs, CA), and is positioned orthogonally to the illumination path. Configuration 1 (Figure 5-1**(a)**), a preliminary mount design, includes an aluminum piece of tape along an imaging axis on the quartz window to provide a reflective calibration target at the same standoff distance as the phantom for standardization of generated THz imagery. Analysis of THz hydration mapping acquired with this mount indicated that topographical changes in the aluminum tape were evident across the image sets as well as spatial gradients across the field of view. Consequently, the mount design was revised.

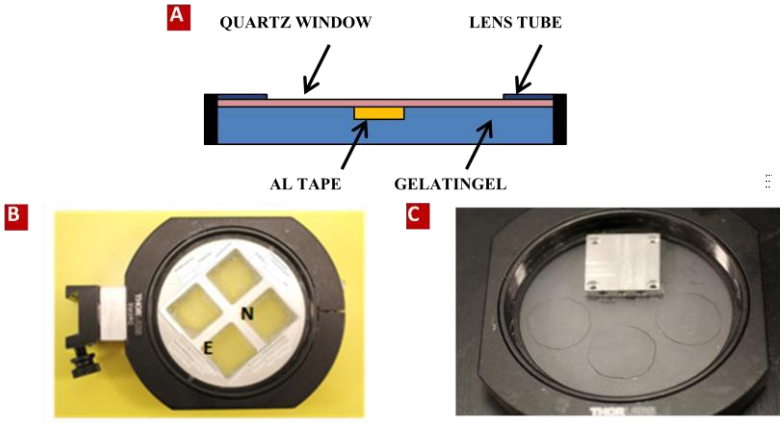

Figure 5-1: Illustration of experimental geometry of a (a) mount configuration. (b) Visible picture of mount configuration 2 after inversion. (c) Visible picture of mount configuration 3 before inversion.

Configuration 2, a reflective aluminum disc (~71 mm in diameter with a 4mm thickness) with four 20 mm x 20 mm extruded compartments, was designed and machined to serve as a robust reflective calibration target to sit on the quart window at the same standoff distance as the phantoms, or gels, it contains **(**Figure 5-1**(b))**. This aluminum component holds multiple samples to 1) assess the repeatability of the gel fabrication process and 2) to evaluate spatial and temporal drift of the system power levels observed between phantom sets. Gels were placed in the northern (N) and eastern (E) compartments, which is evident in the THz imagery presented in Figure 5-1. Configuration 3 uses a 20 mm x 20 mm aluminum mount on the quartz window as a reflective calibration target and holds two gels, indicated by the left and right circles drawn in ink **(**Figure 5-1**(c))**. Once gels were positioned into the configurations discussed above, the mount was inverted to create the following three layer system: Air-Quartz-Phantom.

5.2.2 Phantom Synthesis

Porcine derived gelatin (Sigma Aldrich, MO) phantoms were synthesized in a series of percent-by-weight (%wt) mixtures ranging from 83% water content to 95% for most of the gel solutions. The choice of gel hydration content was motivated by the physiological relevance of this range to ophthalmological applications as well as gel synthesis restraints; at lower

concentrations it becomes more difficult to create uniform suspensions [172], [180]. For each percent hydration phantom, dry gelatin powder and the respective ratio of DI water were measured on a high precision scale (ZSA 80, Scientech, Boulder Colorado) to create 15 ml solutions. Two mixtures of the same hydration concentration were prepared simultaneously to test the repeatability of the fabrication process and to evaluate spatial/temporal variations in THz power during the image acquisition process. These mixtures were left in a water bath to dissolve at 58ºC for 30 minutes. Dissolved solutions were then poured into wells of a 6-well cell culture plate to a height of 8 mm and allowed to cool to room temperature. Upon hardening, 12.5 mm diameter discs and 8 mm x 4 mm cubes were cut from the gel and positioned on the mount for configurations 3 and 2, respectively. In the case of configuration 1, which had to be abandoned due to topographical effects of the reflective calibration target, the entire 15 ml solution was poured into the mount and allowed to congeal. The synthesis order of the varying percent hydration gel phantoms was randomized to account for spatial and temporal system bias.

5.2.3 THz Imaging of Phantoms

THz imagery of the gelatin phantoms was acquired using the existing reflective THz imager. A 90 mm x 90 mm field of view (FOV) was acquired within 30 minutes using a 0.5 mm step size.

5.3 RESULTS

5.3.1 THz System Sensitivity to Water Concentration

The THz imaging results of the hydration phantom experiment using mount configuration 1 are illustrated in Figure 5-2, with the aluminum tape represented by the bright rectangle centered along the x-axis, the mount container identified by the outer red ring, and the quartz window without (Figure 5-2**(a-b)**) and with a gel (Figure 5-2 **(c) –** Figure 5-2**(f)**) represented by the inner red and blue disc, respectively. In Figure 5-2**(b)–(f)**, a region of interest (ROI) was selected to

contain the entire inner disc, which assigns a maximum value to the highest intensity pixel in the ROI and adjusts all other pixels in the field of view (FOV) to this value. All pixels within the window, with the exclusion of those associated with the aluminum tape, are captured in the ROI. An ROI enclosing the quartz window with no gel beneath it (Figure 5-2 **(b)**) is associated with the greatest degree of brightness due to the larger mismatch between the refractive indices of the Air-Quartz-Air system [181]. Figure 5-2**(c)-(f)** represent the Air-Quartz-Phantom-Air system, which is further simplified to a three layer model (Air-Quartz-Phantom) assuming that the phantom layer is effectively infinite. All the intensities in these figures are lower than those of the previous system given the closer match between the refractive indices of the quartz window and the underlying gelatin gel.

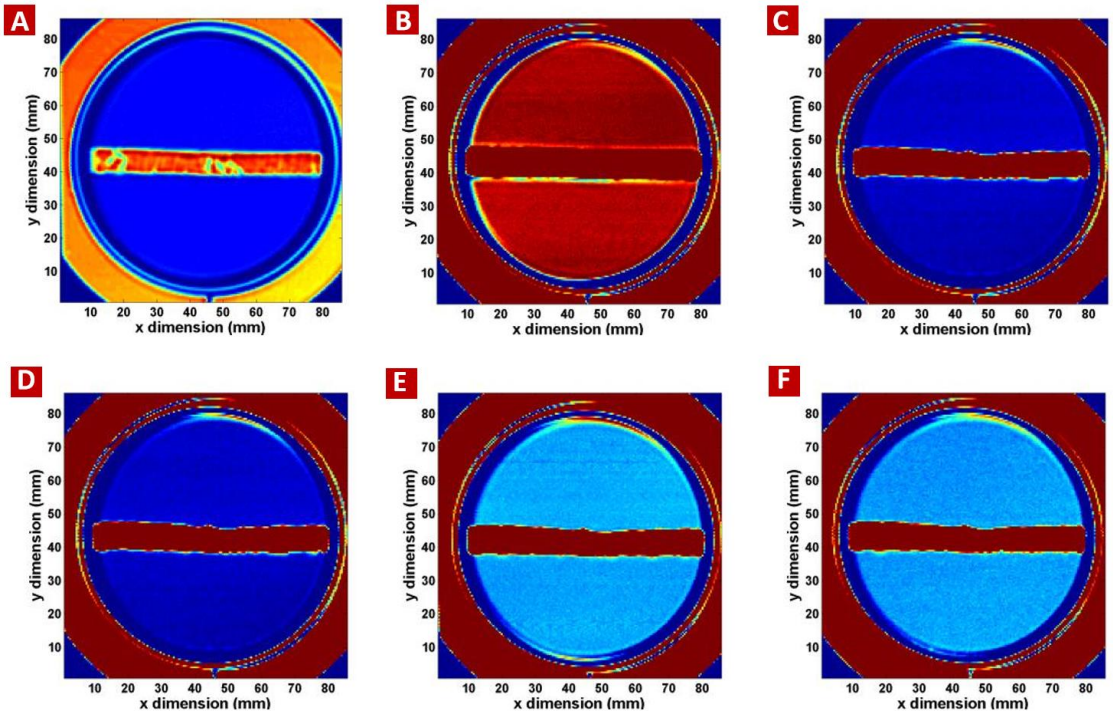

Figure 5-2. THz imagery of mount configuration 1. A: Raw THz image (No ROI selection) of the mount with an aluminum strip of tape along the center and no underlying gel. Region of interest (ROI) contains the B: quartz window with no gel, C: 83% hydration gel, D: 85% hydration gel, E: 87% hydration gel, and F:89% hydration gel. As hydration content of the gel phantoms incrementally increases, the respective THz reflectivities also increase. All images share a common color map.

As the hydration content of the gels is increased by 2% increments, the THz imagery of the more saturated gels appears brighter across the entire image. The uniformity in brightness of these large gels, measuring 72 mm in diameter, indicates low variances in intensity across the entire sample and reinforces the homogeneity of the gel fabrication process. Although these findings are qualitatively compelling, topographical changes observed in the aluminum calibration target prevented accurate standardization across the different image hydration sets. In addition, we suspect that long term fluctuations in system power amplitude may have overshadowed hydration changes observed in such a narrow hydration sensitivity range.

Figure 5-3 is the resultant THz imagery of hydration phantoms placed in mount configuration 3. Similar to configuration 1, THz reflectivities associated with ROIs of neighboring gelatin samples of the same concentration, referred to as "left" and "right" gels, monotonically increase with increasing hydration content. Due to spatially varying THz reflectivity in the FOV, ROIs were selected for both the right and left gels that capture the entire gel sample size. The images indicate that ROIs of the 89% hydration gelatin phantoms (high intensity yellow discs in Figure 5-3**(c**) have a greater reflectivity compared to those of gelatin phantoms with 83% water content (Figure 5-3 **(a)**).

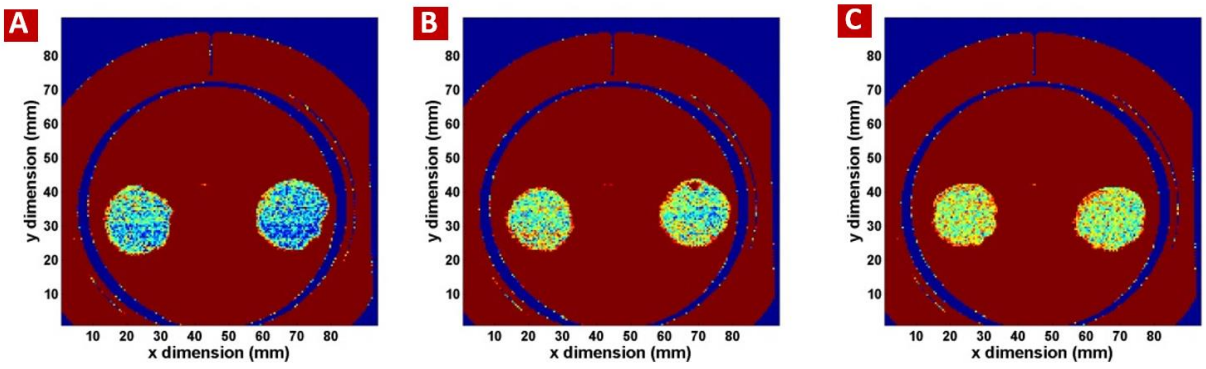

Figure 5-3. THz imagery of mount configuration 3. A: 83% hydration, B: 85% hydration, and C: 87% hydration gel. Left and right gels are evaluated independently. As hydration content of the gel phantoms incrementally increases, the respective THz reflectivities also increase. All images share a common color map.

Sample means of normalized THz reflectivities (ranging from 0 to 1) for left gel phantoms synthesized at 83%, 85%, 87%, 91% and 93% hydration saturations for mount configuration 3

were calculated to be 0.0516, 0.0524, 0.0526, 0.0529, 0.0536, and 0.0544, respectively, where the highest sample margin of error (at 95% confidence) was calculated to be ±1.41x 10^{-4} . In comparison, normalized THz reflectivity values of the right gel were calculated to be 0.0512, 0.0514, 0.0517, 0.0524, 0.0532, and 0.05404 for an identical hydration range, with the highest margin of error (at 95% confidence) equal to±1.81x 10^{-4}.

As illustrated in Figure 5-4, linear regression curves fit both data sets with statistically significant R^2 values (R^2 = 0.953 and R^2= 0.949 for the left and right gel, respectively) and p values (p = 0.008 and p = 0.001 for the left and right gel, respectively) calculated with a one way ANOVA test **(Table 6)**; as the hydration content of the gel phantoms is increased, the normalized THz reflectivity of these samples also increases in a linear fashion within this narrow hydration regime.

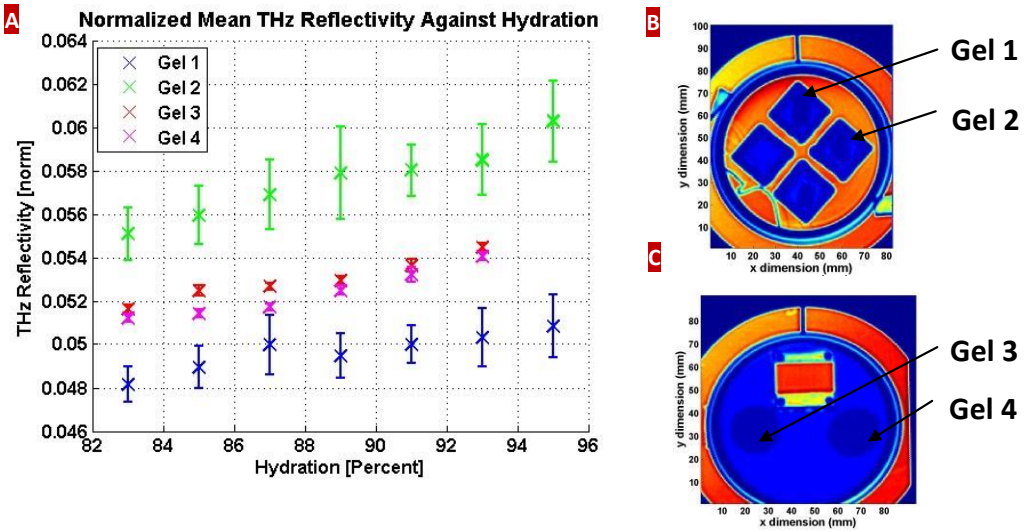

Figure 5-4. A: Reflectivity vs. Hydration curves for all gelatin phantom sets with 95% confidence. B: Raw THz image of mount configuration 2 with location of gels. C: Raw THz image of mount configuration 3 with location of gels.

The hydration sensitivity (reflectivity: % hydration), captured by the slope of the linear fits, was 0.0258% and 0.0289% for the left and right gel, respectively. Similar linear trends and hydration sensitivities were computed for gels imaged with configuration 2: 0.0389% and 0.0209% for the northern and eastern gel, respectively. Due to smaller sample sizes associated

Table 6: HYDRATION SENSITIVITIES OF GELATIN PHANTOMS

		% Hydration Sensitivity (refl. : % hyd)	R^2 value	1 Way ANOVA
Mount Configuration 2	**Gel 1 / North gel**	0.0209	0.0981	p = 0.016
	Gel 2 / East gel	0.0389	0.956	p = 0.0009
Mount Configuration 3	**Gel 3 / Left gel**	0.0258	0.953	p = 0.008
	Gel 4 / Right gel	0.0289	0.949	p = 0.001

with these gelatin phantoms, their margins of error are roughly twice those observed for gels imaged with mount configuration 3.

Considering that both gel sets (left/right and east/north for mount configurations 3 and 2, respectively) were imaged simultaneously for all hydration saturations, discrepancies observed within the curves of a particular mount configuration and between different configurations may be due to an imaging plane having a spatially varying impulse response. Analysis of the normalized mean aluminum reflectivities associated with the calibration targets in each mount configuration indicates fluctuations between 0.635 to 0.675 for mount configuration 3 and between 0.9212 and 1 for mount configuration 2. These findings suggest that there are variations as large as 8% in the maximum THz power within hydration experiments using the same mount configuration and variations as large as 32% between experiments that employ different mount configurations.

5.4 DISCUSSION

Differences in the calculated hydration sensitivities for varying gel phantom experiments reinforce the challenges in establishing a robust standard for THz hydration calibration that effectively accounts for variations in system performance. Due to changes in THz reflectivities of a constant hydration phantom across –x and –y directions as well as drift in system bias, a single relation between THz reflectivity and phantom hydration content is insufficient. Instead, multiple hydration sensitivity curves of gelatin phantoms, similar to those generated in this study, can

account for temporal and spatial system differences between and during image acquisition periods to allow for quantitative comparisons within and between varying THz hydration sensing data sets. For example, THz imagery of gelatin hydration phantoms may generate data that fits gel curve 1 of Figure 5-4 on day 1 of a hydration experiment and data that fits gel curve 3 on day 2 of the same study. To quantitatively compare hydration imagery acquired on each day, the hydration sensitivity curves can be easily compared with one another at each percent hydration point. This concept can be further generalized to include reflective THz hydration imagery acquired by imaging systems developed at different academic institutions. THz hydration maps of tissue mimicking targets can be transformed such that their empirical calibration curve is described by a maximum goodness of fit relative to a golden standard.

5.4.1 Simulation of THz-Phantom Interactions

The reflectivity spectra of a hydration phantom imaged under a quartz window can be simulated as a three-layer system (Air-Quartz-Phantom) using the Transfer Matrix Method (Figure 5-5) [6], [162]. The simulation employs the Debye dielectric model to calculate the dielectric constant of water and the Bruggeman effective media model to calculate the index of refraction of the phantom for each hydration saturation level. The simulation samples the three-layer system in step sizes of 1 GHz from 300 GHz to 775 GHz and examines hydrations from 0.001 to 0.999 in increments of 0.001 (0.1%). The generated result is multiplied by the system responsivity spectrum to create a receiver-source-object spectrum, which is finally integrated to assign voltage values for all phantom hydration levels. The simulation indicates that reflectivity vs. water content in the region of 81% - 97% hydration is linear, with a R^2 value of 1. These simulation results agree with and validate the linear trends observed in the experimental results.

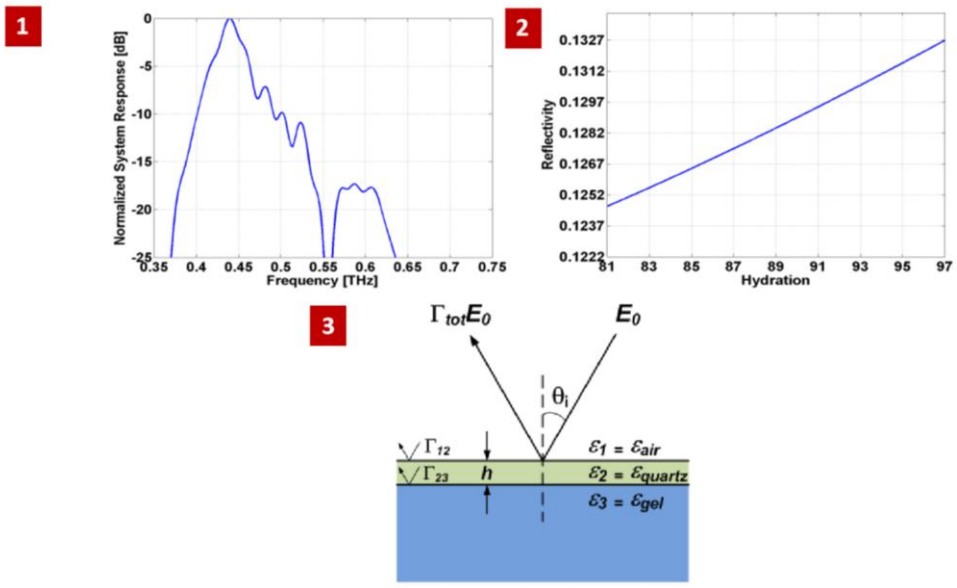

Figure 5-5: 1: Empirical product of measured source and receiver spectra. 2: Normalized response vs. hydration curve from 81-91% hydration. 3: Three layer system simulation of THz-phantom interactions using the Transfer Matrix Method.

5.5 APPLICATIONS

Characterized by high hydration sensitivity to tissue equivalent phantoms, reflective THz hydration sensing possesses great potential for accurate assessments of the onset and evolution of injuries to the skin, specifically wounds. This technology offers the ability to noninvasively detect minute changes in water content in the hydration range relevant to skin applications with high water concentration sensitivity (0.02 – 0.038%), and may potentially be used to diagnose edema. Edema is typically qualitatively estimated by visual inspection, so THz imaging could serve as an augmentation to current clinical standard assessment. Future research should implement hydration phantom calibration of THz sensing at higher frequency illumination prior to *in vivo* studies to explore tradeoffs between hydration sensitivity and spatial resolution.

5.6 CONCLUSIONS

This study confirms that THz sensing requires calibration of clinical performance metrics, specifically hydration concentration sensitivity. Gelatin hydration targets, identified as an appropriate tissue-mimicking model for reflective THz imaging applications, can be used to relate THz reflectivities to water content for quantitative comparisons of THz hydration imagery. Within a hydration range of 83% - 95%, pertinent for *in vivo* medical assessments, a positive linear trend was observed between increases in hydration and corresponding THz reflectivities. Statistically significant hydration sensitivities between 0.0209 – 0.0389% were calculated for multiple hydration phantom configurations, and the generated calibration curves can be implemented to correlate data sets associated with varying spatial and temporal effects.

CHAPTER 6: *EX VIVO* MRI OF PORCINE SKIN BURNS

6.1 MOTIVATION

Preliminary THz imagery of partial thickness and full thickness burn wounds suggests that hydration gradients are responsible for the observed image contrast. Subsequent THz imaging of hydration phantoms of known water concentration also demonstrates the sensitivity of THz sensing to variation in water concentration. However, sensitivity and image contrast are not synonymous; an imaging modality may be sensitive to several tissue properties but more sensitive to specific tissue components from which the dominant source of image contrast originates. Unlike depth-resolved images of tissue acquired with magnetic resonance imaging (MRI), THz images of tissue are 2D reflection maps representing an aggregate tissue property. Because water constitutes ~70% of the weight of soft tissue, and the THz frequency dielectric constant of water is significantly higher than that of non-water constituents, the aggregate reflected signal observed with *in vivo* THz imaging is interpreted as TWC [13], [15]. However, liquid water displays broad absorption bands rather than *narrow* absorption signatures in the THz band. Consequently, this observation does not identify TWC as the primary source of contrast in THz imaging. Therefore a companion imaging modality is currently needed to interpret contrast in THz tissue data [7].

MRI offers a means to visualize changes caused by water ingress and egress *in vivo* in skin layers [46]. A non- invasive imaging technique, MRI can be used to detect the location, concentration, and chemical environment of skin water protons and how these parameters change as a function of hydration [46]. Traditional techniques used to measure skin hydration *in vivo* do not provide direct measurements of water, but rather infer its presence as a result of changes in specific skin parameters, such as electrical impedence conductivity or transepidermal water loss (TEWL) [44], [45]. These methods are invasive and may result in a temporary deficiency of stratum corneum barrier function [46]. High resolution ultrasound, currently the benchmark in *in vivo* skin imaging, provides mean values of water content [47]. The use of

ultrasound probes in the range of 15-50 MHz frequencies to visualize layers of the dermis and epidermis and poor depth resolution make ultrasound studies difficult in practice, lending MRI as a more effective imaging technique in detecting hydration [48]. The hydration contrast parameters of MRI (relaxation times (T_1 and T_2) and proton density) are well established and provide measures of mobile water content in localized areas [182]. Transverse relaxation time (T_2) is a more sensitive indicator of changes in the amount of mobile water than longitudinal relaxation time (T_1). Here, we aim to use T_2-weighted MRI imaging in an *ex vivo* porcine model to 1) test the feasibility of this technique to detect variation in TWC; 2) and optimize MRI imaging parameters for future studies that will investigate the hydration states observed in preliminary *in vivo* THz burn imagery. MRI measures of TWC in burns are compared to histopathology. Insights gleaned from this research effort will be used to lay the ground work for parallel MRI-THz imaging of injury-induced edema in *in vivo* pre-clinical models as well as further support the use of THz imaging to track fluid shits in patients sustaining cutaneous wounds.

6.2 MATERIALS & METHODS

6.2.1 Porcine Skin Burns

Preliminary studies were performed in *ex vivo* porcine tissue phantoms to assess the feasibility of 7 T MRI of skin burns. Porcine skin is a close physiological and anatomical model of human skin and was therefore chosen as a phantom for this study. Skin samples (25 mm x 50 mm sections, with 2.5 mm thickness) were fixed to an acrylic substrate with nylon fiducial markers and burned with a 18 mm x 6 mm brass brand heated to temperatures between 250 to 530°C, and immersed in a 50 ml centrifuge tube of Galden HT 55 fluid.

6.2.2 7 Tesla T2-weighted and Diffusion-weighted MRI

The MR scanner used to obtain preliminary hydration imaging results, illustrated in **Figure 6-1,** is a Bruker 7.0T MRI instrument (Bruker Biospin, Switzerland) with a clear bore diameter of 30 cm. This diameter is sufficiently large to image small animals including rats. A 116 mm

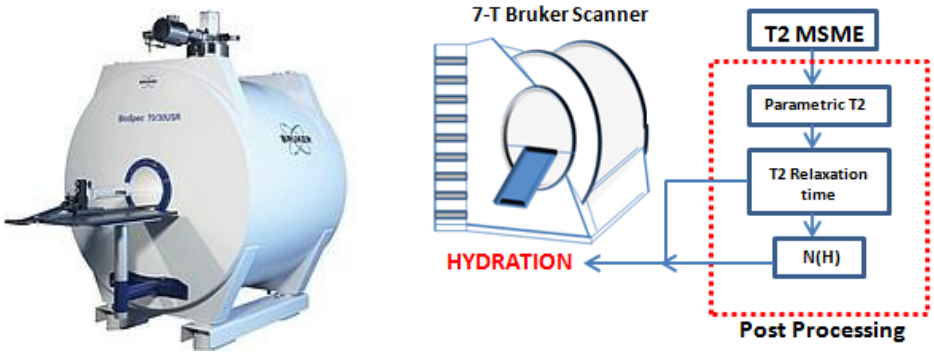

Figure 6-1: Visible image of 7-T Bruker MRI Scanner (left), and a schematic of the 7T- MR scanner operating with a T2 MSME contrast sequence (right).

inner diameter gradient system was used to generate a maximum gradient strength of 400 mT/m. Optimal reception sensitivity was achieved with a 7.5 cm surface gradient coil which reduced losses magnetically coupled to the sample and increased the maximum gradient intensity perpendicular to the skin surface. Surface artifacts were reduced by immersing samples in HT55 Galden oil, a heat transfer fluid commonly used in skin spectroscopy studies. MR imagery of burn tissue samples not suspended in Galden oil was also collected to determine possible hydration effects of Galden oil. Co-registration of MRI generated imagery with histological analysis was achieved using nylon screw fiducial markers that were captured in every burn slice and measurements from these to the burn origin. T_2 weighted multi slice multi echo (T_2w MSME) and diffusion weighted echo contrast sequence data (**Figure 6-1**) was then acquired for both pre and post burn samples (128 x 456 x 48 um anisotropic voxel size; 0.0859 x 0.1719 x 2 mm pixel resolution; 2 mm slice thickness; 120 ms echo time; 4.4 x 1.1 cm FOW; 14 min acquisition time; 180 degree FA; 14ms T_E; 1000 ms T_R). T_2 relaxation times were calculated from the relation in **equation (1).** Following the study, porcine skin specimens were fixed in 10% formalin and sectioned for histopathological assessment of burn severity.

6.3 RESULTS

6.3.1 *Ex Vivo* MRI Imagery and Histological Assessment

7T MR tissue characterization of *ex vivo* porcine skin burns showed two significant results: first, T_2 relaxation times and relative proton density behavior increase in post burn samples, and 2) these multiparametric findings increased with increasing burn wound temperature.

T_2 and *p*, which describes the density of mobile water protons, are closely related to protein-water interactions, and thus change with burn induction of the skin. Thermal injury of tissue results in cellular damage of the affected area and a loss of macromolecular-water interaction sites, compromising the structured architecture of skin and releasing water originally bound to surfaces into a more mobile state. Damaged cells also release their contents, mainly water, and an increase in total water content occurs. This phenomenon is visualized as increased intensity of the burn region in MR generated images.

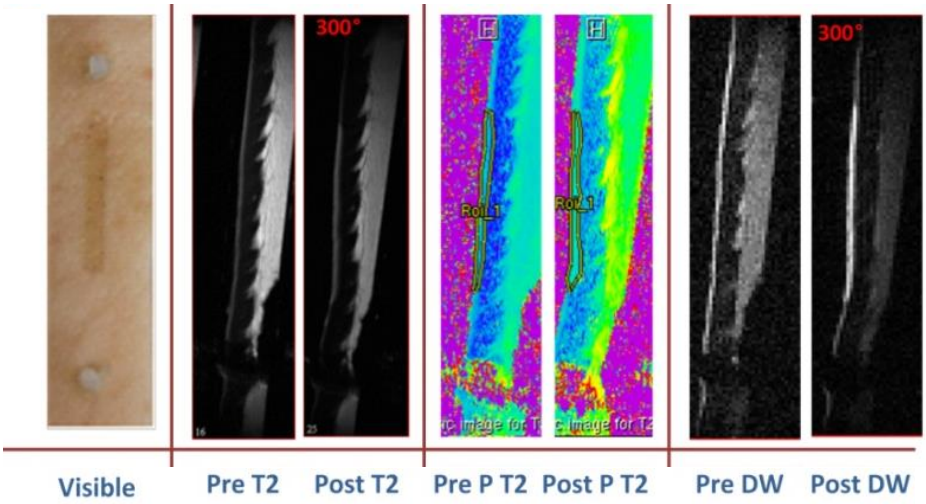

Figure 6-2. Visible porcine skin burn image, pre and post T2w MSME images, parametric (PT2) images of T2 relaxation times, and diffusion weighted spin echo images of a 300°C burn. Post T2w burn images show increased signal intensities of the burn region. Post parametric T2w images are associated with increased T2 relaxation times compared to surrounding normal tissue and pre burn images.

Acquired T_2w MSME images, shown in Visible Pre T2 Post T2 Pre P T2 Post P T2 Pre DW Post DW **Figure 6-2**, demonstrate that injured areas of 350°C burns were associated with a 2.4 fold intensity increase compared to

surrounding normal tissue and pre-burn samples. MR imagery of 350°C samples without Galden oil suspension were characterized by similar intensity increases, however the emergence of surface artifacts resulted in less resolved burn regions. With no evidence of Galden oil fluid changing the hydration state of skin burn tissue, all subsequent imaging used samples prepared in this heat transfer fluid. T_2w MSME images of a 300°C burn in Fig. 4 showed increases in signal intensity in the vicinity of the burn in the post-burn image; the average signal intensity of the 300°C post-burn ROI was lower than that of the 350°C burn. For the 250 °C study, visual inspection of pre- and post-burn images showed no differences in intensity, which is confirmed by T2w MSME analysis, suggesting MRI of burns may be sensitive to a particular range of temperatures. Mean T_2 values of the burn region are 35.9 ms for 350°C, 30.2 ms for 300°C, and 28 ms for 250°C burns, where the characteristic T_2 value of uninjured tissue is 24 ms. Mean relaxation time values of uninjured tissue samples, all pre-burn skin specimens, were consistent with *in vitro* values previously reported [182]. Proton density was increased in the burned epidermis in a temperature related fashion (7.6% increase for 350°C, 2.4% for 300°C, and 0.54% for 250°C), confirming changes in burn wound hydration.

Similar findings are confirmed Figure 6-3, a subsequent study that included histological assessments. Burn wound geometry, localization, and severity correlated between MRI and histological analysis. More severe burns, specifically those induced at 530°C, are associated with thick, dark purple H&E stains (Figure 6-3 **(a)**) which extend deep into the dermis. Similarly, burns induced at 350°C can be visualized in H&E histopathology images (Figure 6-3 **(b)),** however these are characterized by a reduced burn extent compared to those at higher burn temperatures. These and the previous studies demonstrated that MRI is a suitable method to evaluate the behavior of water molecules in burned tissues. In addition to spatial localization of burn areas, MRI furnished multiparametric information including T_2 proton relaxation times and p measurements. These intrinsic parameters of tissues are sensitive to both water content and water structure of skin, lending MRI as non-invasive tissue characterization tool to investigate the

motional behavior of biological water in burn wounds. Acquired T2w MSME hydration results correlate well with THz hydration mapping of in vivo partial thickness burns, which can accurately detect >20% increases in THz reflectivity with respect to normal tissue in burn zones. Burn imagery acquired with both THz and MR imaging modalities result in burn regions that are characterized by high signal intensities, indicating changes in the hydration states of injured tissue. *In vivo* THz imagery captures the ingress of water that results from biologic inflammatory responses to injured tissue. T_2 weighted MR of *ex vivo* skin, which lacks the dynamic responses of living tissue, does not detect an increased flux in water but rather a change in the water structure and increases in mobile water content. Although the independent effects of water structure and water content on hydration are difficult to isolate, the visible and quantifiable changes in water that are responsible for contrast generation in MR skin burn imagery suggest that the contrast mechanism of THz burn imaging relies on hydration states of biological tissues. Future studies using parallel *ex vivo* and *in vivo* MR and THz imaging are necessary to better understand and investigate quantitative correlations.

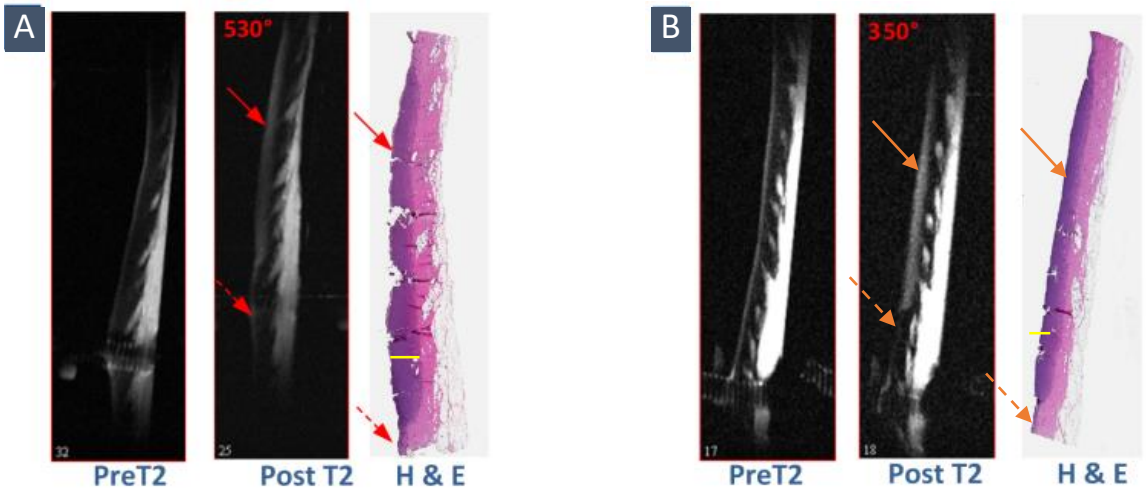

Figure 6-3: Pre and post sagittal T2 MSME images of a A) 530°C burn and B) 350°C burn with H&E sections to verify burn severity. Thick, dark purple stains along the length of the H&E image correspond to cell damage, spatially localizing the burn region. More severe burns extend deeper into the dermis, demonstrating that higher burn temperatures, such as 530°C, are associated with greater burn extents. Burn extent is shown as horizontal yellow lines in the H&E images. Solid arrows point to burned tissue and dashed arrows designate healthy tissue.

6.4 CONCLUSIONS

This research investigates MRI hydration indicators, specifically changes in T_2 relaxation times and proton densities *p*, as a possible means to verify tissue water content as the dominant contrast mechanism in THz burn imaging. T_2 weighted multislice mutiecho MRI studies in *ex vivo* porcine skin demonstrated that T_2 relaxation times and *p* values, common MR indices of hydration, increased following burn induction and with increases in burn temperature. Thus, MRI may be used as a supplementary tool in future *in vivo* THz imaging studies to substantiate variation in TWC as the source of image contrast in observed THz maps.

CHAPTER 7: *IN VIVO* REFLECTIVE THz IMAGING OF BURN-INDUCED EDEMA CORRELATED WITH MRI

7.1 SIGNIFICANCE

Tissue edema, the build-up of fluid in tissue, is often an underlying cause of infection and morbidity. Quantifying and visualizing edema, however, remains a clinical challenge. We show that it is possible to non-invasively and rapidly detect fluid shifts in burn-induced edema models using reflective terahertz (THz) imaging. For *in vivo* burn wounds of varying severity, the time course and magnitude of THz reflectivity associated with the burn region reflected known trends observed in edema pathogenesis and strongly correlated with companion hydration measurements acquired at specific burn depths by magnetic resonance imaging (MRI). This work offers the first *in vivo* correlative assessment of mobile TWC as a major contributor to THz imaging contrast. THz imaging in acute injuries could enable earlier tissue viability assessment and treatment in patients sustaining severe burns, trauma, or other conditions leading to profound tissue edema.

7.2 MOTIVATION

Recent *ex vivo* evidence shows that MRI can be used to verify the contributions of TWC to THz imaging of superficial tissues [15]. Despite its limited access and associated costs, MRI can resolve depth information and provide comprehensive, layer-specific anatomical and physiological data on TWC in a single setting. Among the multitude of sequences available, T_2-weighted (T_2w) MRI has previously been used to successfully generate native, pathology-specific tissue contrast for burn wound assessment in an *ex vivo* skin model. Tissue contrast in T_2w MRI is primarily determined by differences in the transverse component of proton relaxation time (T_2), from which relative proton density - the fraction of mobile water protons available in the tissue - can be calculated [183]. Specifically, relative proton density has been used to distinguish protein-

bound water from “free” water (i.e. effusion or edema) in superficial wounds of increasing severity (superficial, superficial partial, deep partial, and full thickness) *ex vivo* [15]. Among wound models, *in vivo* burn injuries are more clinically relevant and are characterized by the biggest inflammatory reaction and result in substantial and rapid edema formation [64], [80], [86].

Herein, this work investigates the potential of THz imaging for edema assessment by correlating THz frequency tissue reflectivity measurements with relative proton density measurements captured by T_2w MRI in burn-induced edema models. It is important to note that MRI is only used here for pre-clinical research purposes, as its cost and limited portability make it inappropriate for TWC characterization in patients, especially critical patients. Burn wounds in rats are known to severely and acutely perturb TWC and, thus, were selected as the model for this correlative study. A partial thickness burn (n=1) and a full thickness burn (n=1) were induced *in vivo* to the abdominal skin of rats using an established contact wound protocol that exhibits markedly different TWC perturbations corresponding to burn severity [9], [147]. Concomitant THz and MRI images of both burn models were acquired with a previously reported reflective THz system and 7T MRI prior to thermal insult, 90 min, 210 min, and 270 min following burn induction [6], [9], [15]. Previous work in THz wound imaging has shown that partial thickness and full thickness burns produce pronounced and distinct spatiotemporal changes in THz image contrast. Therefore, similar to THz imaging, we hypothesized that MRI TWC-based contrast would: I) exhibit unique signal characteristics for each wound model; and II) agree with trends observed in the companion THz burn imagery [6], [9], [10].

Compared to THz imaging, which furnishes a 2D surface reflection map of the underlying tissue, a 2D MRI scan provides a cross-section of depth-dependent TWC information across multiple skin layers. In other words, there is a one-to-many relationship between THz imaging and MRI data. Following histological assessment of burn severity in each wound model, a one-to-many cross-correlation across time was performed between the THz reflectivity of the burn region and many relative proton density measurements acquired by MRI at specific tissue depths in the

same burn area to: I) investigate mobile TWC (i.e. edema) as the underlying biophysical driver of observed changes in THz reflectivity and II) quantify, for the first time *in vivo,* the tissue depths at which THz imaging can potentially probe edema.

7.3 MATERIALS & METHODS

7.3.1 Injury-Induced Cutaneous Edema

All experiments were approved by the Institutional Animal Care and Use Committee (IACUC). Two male Sprague Dawley rats weighing 180-200g (Harlan laboratories, Hayward, CA) were used as preclinical models to investigate the effects of burn-induced edema on reflective THz imaging contrast. While pigs are a more appropriate genomic model of human skin, THz imaging in bulk tissue is insensitive to molecular-based mechanisms [184]. Rats are also widely available, convenient in size, and tractable in nature, lending them as an attractive model [147]. Finally, there are few known differences in edema physiology between rats and other candidate animal models.

Surgical preparation of the rats began with administration of extrinsic intradermal fiducial markers to allow for image registration between the THz images, visible images, and histology. 72 h prior to burn induction, each rat was anesthetized using isoflurane (4% and 1% for induction and maintenance, respectively), the skin from the abdomen was shaved to expose a 5 cm x 5 cm area of bare skin, and three tattoos were applied to the abdomen; intradermal injections of non-metallic green ink were administered via a sterile 28G needle to form the apices of a right triangle. Once tattooed, both subjects were awoken and allowed to recover for 72hr.

On the day of imaging, each rat was injected with Buprenorphine (analgesic) subcutaneously one hour prior to induction of general anesthesia with isoflurane gas delivered through a nose cone. Any abdominal hair that had grown back since tattooing was shaved and aseptically cleaned. Rats were placed on an internal heating pad to maintain normal body temperature during

imaging. A 2 mm x 19 mm rectangular brass brand was secured to a thermocouple (OMEGA, Stamford, Connecticut), that accurately monitors the absolute temperature of the brand, heated to 200°C and 130°C using a hot plate, positioned between the fiducial markers, and applied with a constant pressure for 10 s to induce a full thickness and partial thickness abdominal burn [9]. This burn contact methodology resulted in a partial and full thickness wound of uniform burn severity. Each rat received one burn to minimize the total burned body surface area, thus reducing effects of shock on the physiologic response.

7.3.2 Imaging Systems

A 7T small bore MRI scanner (Bruker Biospin, Switzerland) was used to acquire MR imagery of *in vivo* burns [15]. To obtain high-resolution images a 160 mm gradient was used to achieve a pixel size of 86 microns in depth in combination with a small surface radiofrequency coil (3 cm in diameter) to improve the signal-to-noise ratio (SNR). High-resolution T_2w multislice multiecho (MSME) MR images of abdominal skin prior to and following burn induction were obtained by varying T_E (T_R = 500 ms, eight TE values including 14, 28, 42, 56, 70, 84, 98, and 112 ms) within a 44 x 11 mm^2 field of view and a slice thickness of 2 mm, corresponding to a voxel dimension of 172 x 86 x 2000 μm^3. A total stack of six axially oriented MRI slices required an image acquisition time of ~35 min. The aforementioned protocol has previously been used to acquire spatially resolved imagery of *ex vivo* skin burns with high contrast and SNR [15].

A reflective THz imaging system was used to acquire THz images of uninjured skin and burn tissue [6], [9], [132]. The system consists of a photoconductive switch based THz emitter, Schottky diode detector, and a novel gated receiver for high SNR, high dynamic range measurements of THz power. The Schottky diode detector is mounted in a 0.381 x 0.1905 mm rectangular waveguide (WR1.5) to limit the system detection to the 400 GHz – 700 GHz band. Considering the emitter's power spectral density and detector's spectral responsivity, the detected THz signal has a center frequency of 525 GHz with a 125 GHz effective bandwidth. These spectral

parameters are chosen to balance TWC sensitivity and sufficient spatial resolution, while mitigating clutter in the acquired image [6]. The THz beam is handled by quasi-optical imaging system that focuses the radiation to a 1 mm^2 diameter spot at a 36 mm standoff distance. THz imagery was generated by raster scanning the imaging subject beneath the fixed, focused THz beam at a 1 ms per-pixel integration time. An image with a 6 cm x 6 cm field of view (FOV) required a scanning time of ~10 min using a 0.5 mm step size.

On the day of the burn study, visible and THz images of the uninjured, tattooed abdominal skin of anesthetized rats in supine position were captured with an SLR camera and the THz imaging system. In comparison, control scans of the animal in prone position were acquired using a T_2w MSME sequence with the 7T animal instrument. A 12 μm thick optical Mylar window (~3.1 cm in diameter), transparent to THz illumination, was lowered onto the abdominal skin during THz imaging to flatten the imaging plane and minimize effects from non-uniform surface contours. While increased coupling pressure between the rat abdomen and Mylar window can potentially result in areas of high reflectivity, such as those evident in a full thickness wound at t=0 min (Fig. 1A), this effect was intrinsic to a single subject and, therefore, did not affect correlations performed between the subjects.

Before MRI imaging, the Mylar window was removed and two 0.75 cm MRI fiducial markers (Radiance filled Ortho-SPOT Packets, Beekley Medical, Bristol, Connecticut) were positioned superior and inferior to the designated burn induction area and a visible image was acquired. The rat was then placed on the surface coil in prone position for MRI scanning of the uninjured skin; this positioning of the coil on the abdominal skin increased the SNR.

Upon completion of the control scans, a full thickness and partial thickness burn were induced on the rat abdomens. Visible and THz imaging of a burn region covered a 58 mm x 58 mm field of view (FOV). THz images displayed in Fig. 1 only include tissue under the Mylar window, and this measures 7.5 cm^2. MRI covered a registered volume of 44 mm x 11 mm x 92 mm volume.

Parallel THz and MRI imagery were acquired continuously over a 5 h period. The rats were then returned to the vivarium and euthanized 3 days following burn induction because the final status of a burn wound typically manifests 72 h following thermal insult [80].

7.3.3 MRI and THz Analysis

A one-to-many analysis of 2D THz surface imagery of burn wounds and parallel 2D, depth-dependent MRI images was performed for all time points. The MRI signal, S, for a T_2w image is:

$$S = k \cdot N(H) \exp\left(-\frac{T_E}{T_2}\right) \quad \textbf{(1)}$$

where k is a function of the instrument's receiver gain, N(H) is proportional to the mobile proton density, T_2 is the transverse MR relaxation time, and T_E is the echo time. At t=0, 90 (when the burn was induced), 210, and 270 min, MRI slices at T_E= 28 ms were analyzed by visual inspection. Those MRI slices with the greatest observable contrast in the dermal layer of the burn were selected for image analysis. These slices mostly reside in the center of the wound, and therefore did not capture the fiducial markers positioned at the extremes of the MRI slice stacks.

Parametric analyses of the T2-weighted image series were used to determine the relative proton densities and mean T_2 associated with a 1D contour (~5 mm in length). This contour outlined the burn region of the epidermis and was superimposed at incrementally (86 μm) increasing depths in the underlying dermis. Temporal profiles of mean T_2 time and relative proton density were generated for tissue depths up to ~700 μm in the burn contact region. Mean T_2 time and the associated standard deviation was calculated using ImageJ (NIH, Bethesda, MD) by fitting to relation to equation **(1)** the signal intensity S from the contour. Note that S is a function of the instrument's receiver gain, k, which is optimized for each longitudinal time point. Consequently, N(H) of the burn tissue was normalized to that of the previously described MRI fiducial marker to obtain comparable N(H) values across all time points in the study.

A 5 mm long THz reflectivity contour (indicated by a white vertical line segment in each THz image from Fig.1A), was then spatially mapped from its companion, transverse MRI slice for all time points; mapping between MRI, visible, and THz imagery was enabled by capturing contiguous MRI slices of known thickness (2 mm) along the major axis of the burn, measured to be ~20 mm, that include the MRI fiducial markers. Mean THz reflectivity values of these contours, as well as the associated standard deviations, were normalized to the maximum THz reflectivity acquired from an aluminum calibration target (i.e. ideal reflector) and zero THz reflectivity measured in the absence of a reflecting target (i.e. air). The calibrating reflector was positioned in the same manner and stand-off distance as abdominal skin during the initial THz system scans. Temporal profiles of normalized THz reflectivity values were generated for each burn model and correlated with parallel MRI TWC profiles using normalized-cross correlation.

7.3.4 Normalized-Cross Correlation

Normalized cross correlations of THz reflectivity and depth-dependent relative proton densities associated with the burn region of a partial thickness and full thickness wound were performed as a function of time. Normalization removes the effects of system luminance and enables the comparison of data from two different modalities, specifically THz imaging and MRI. The normalized correlation coefficient, therefore, is invariant to affine transformations that adjust pixel values but do not affect overall relative contrast. This many-to-one correlation between multiple MRI TWC measurements at specific burn depths and THz reflectivity of tissue enables an investigation of TWC contrast and the sensing depth of THz imaging.

The variables are defined as follows:

$$N(t_m, d_n) \rightarrow \textbf{Relative proton density as assessed with MRI at time } t_m \textbf{, depth } d_n$$

$$R_{THz}(t_m) \rightarrow \textbf{THz reflectivity at time } t_m$$

Vectors of time dependent value are expressed as follows:

$$\vec{N}(d_n) = [N(t_1, d_n) \quad N(t_2, d_n) \quad N(t_3, d_n)] \tag{12}$$

$$\vec{R}_{THz} = [R(t_1) \quad R(t_2) \quad R(t_3)] \tag{13}$$

The cross correlation coefficient of the THz time series with the depth dependent MRI relative proton density series is written as the inner product:

$$\rho(d_n) = \left\langle \frac{\vec{N}(d_n) - mean\left(\vec{N}(d_n)\right)}{\left\|\vec{N}(d_n) - mean\left(\vec{N}(d_n)\right)\right\|}, \frac{\vec{R}_{THz} - mean(\vec{R}_{THz})}{\|\vec{R}_{THz} - mean(\vec{R}_{THz})\|} \right\rangle \tag{14}$$

7.3.5 Histological Assessment

A blind histological analysis of burn tissue harvested at 72 h post injury was compared to visible imagery to assign burn severity. Three regions of the burn wound (i.e. left, center, and right) were harvested, transferred to 10% formalin solution, and submitted for histopathological evaluation. All tissue samples were sectioned orthogonal to the major axis of the burn and some contained an intradermally injected tattoo marker for orientation and registration of the tissue specimen. Six histological slices of 5μm thickness were acquired from each tissue block, stained with hematoxylin and eosin, and analyzed to determine burn severity. Histology sections included both burned and healthy areas, providing a control area consisting of unburned tissue to which the burned area was compared. A blind investigation of depth of injury was used to confirm that the 130°C and 200°C wound were a partial thickness and full thickness burn, respectively. Complete epidermal necrosis, pyknotic dermal fibroblasts, polymorphonuclear leukocytosis, muscle necrosis, collagen discoloration, and occluded vessels that have clearly undergone cellular degeneration were used to characterize injured tissue of a full thickness wound. In regards

to depth of injury, these histological features extend into the dermis and subcutaneous layer. In contrast, patent vessels as well as intact skin and muscle tissue that did not exhibit signs of cellular damage were used to classify a partial thickness wound [9].

7.4 RESULTS

Parallel THz and MRI time-series imagery of a partial thickness burn and full thickness burn induced in the abdominal skin of anesthetized rats were acquired over a 5hr period (**Figure 7-1**). This time window was selected based on previous observations of apparent morphological changes in the field of view (FOV) and motivated by the evolution of the wound response following acute injury [107]. Histological features in burn wounds are known to manifest by 72hr following thermal insult, and therefore this endpoint was used to harvest tissue and histologically determine burn severity (i.e. partial thickness and full thickness) (Figure 7-2).

During THz imaging, burn wounds were imaged under a thin (12 μm) film Mylar window to eliminate confounding effects from non-uniform surface contours. The “hot” color map associated with THz imagery transforms black to the global minimum THz reflectivity and white to the global maximum THz reflectivity.

During all time points in the study, mean THz reflectivity was calculated for ~5 mm long contours (indicated by white vertical lines in THz imagery in **Figure 7-1(a)**) that captured the same region of the wound. Mean THz reflectivity values of these contours were normalized to that of an ideal reflector (i.e. aluminum; >95% reflective) and the absence of a reflecting target (i.e. air; ~0% reflective). Temporal profiles of normalized THz reflectivity were generated for the burn contact site in each wound model (Figure 7-3). In comparison, multiple temporal profiles of mean T_2 time and relative proton density were generated for specific tissue depths associated with the same burn contact region in spatially mapped MRI image sets (Figure 7-3).

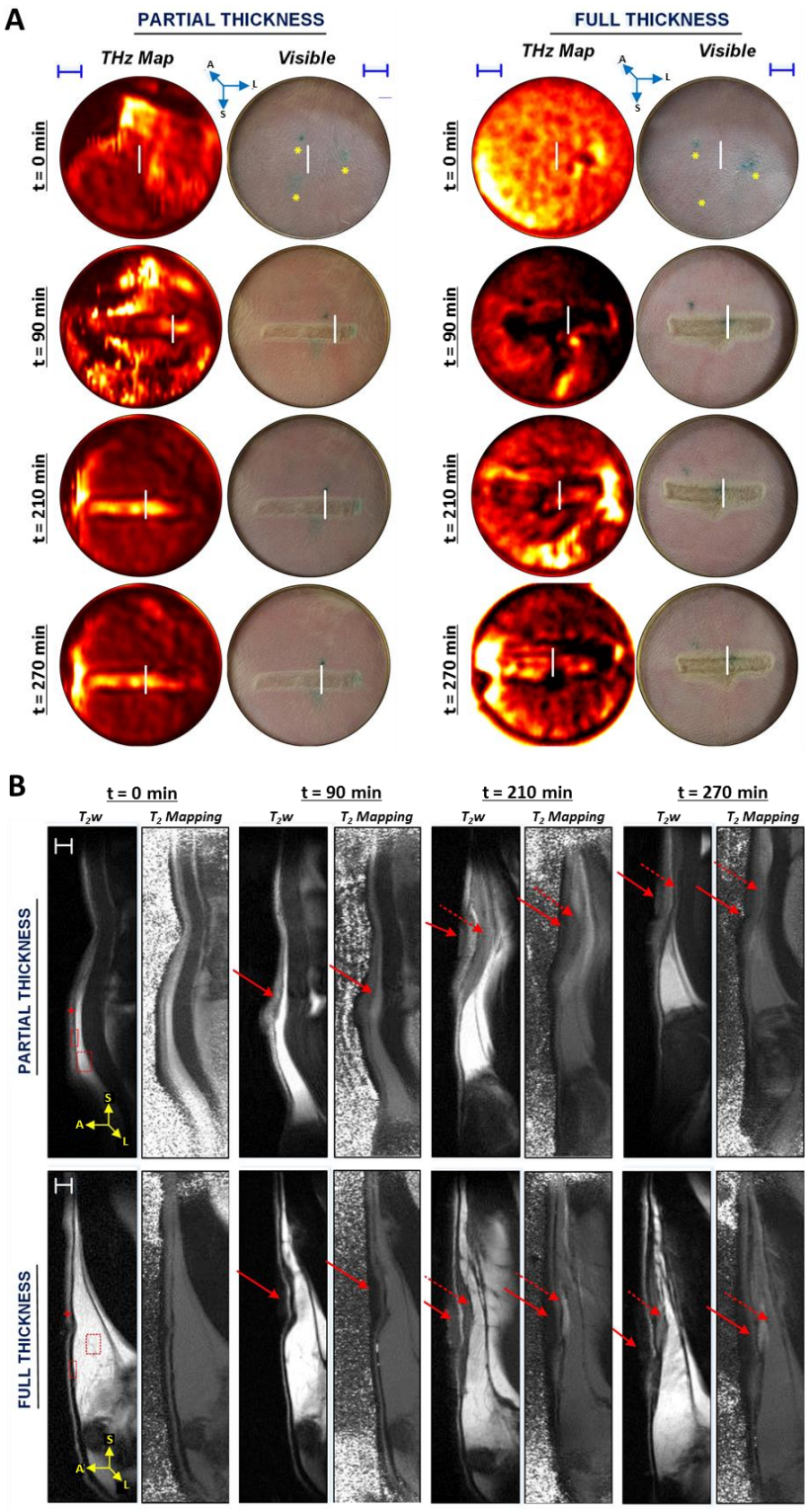

Figure 7-1: A, 2D top-down THz and visible imagery of a rectangular partial and full thickness wound prior to and following burn induction (t=90 min) in rat abdominal skin *in vivo*. THz image sets are displayed in a standard false color map where black-red-yellow-white denotes increased normalized THz reflectivity. Yellow asterisks in the abdominal skin of visible images at t=0 min indicate intradermal fiducial tattoos. *Blue scale bars*, ~6 mm. B, Companion MRI imagery includes 2D transverse T_2w MRI scans and T_2-mapping. All MRI slices spatially map to 1D contours, indicated by solid white vertical lines, shown in their respective THz and visible imagery. MRI images are displayed in a gray-scale color map where black-grey-white indicates increased intensity and T_2 time for T_2w and T_2-mapping images, respectively. At t=0 min in the T_2w MRI scans, layers of the skin are clearly delineated where the outer bright thin line (red cursor) corresponds to the epidermis. The dermis (red solid rectangle) appears as a dark layer, while the hypodermis (red dotted rectangle) is bright. *White horizontal scale bars*, 1.9 mm. Localization of the burn and fluid ingress are demarcated by solid and dashed arrows, respectively. For both a, and b, "L," "S," and "A" in the 3 dimensional axis denote the lateral, superior, and anterior direction, respectively, of a rat imaged in supine position for the THz and visible images and in prone position for parallel MRI imagery. By t=210 and 270 min, MRI and THz signal, both of which appear brighter in a partial thickness wound, become spatially organized within the burn contact area of each wound.

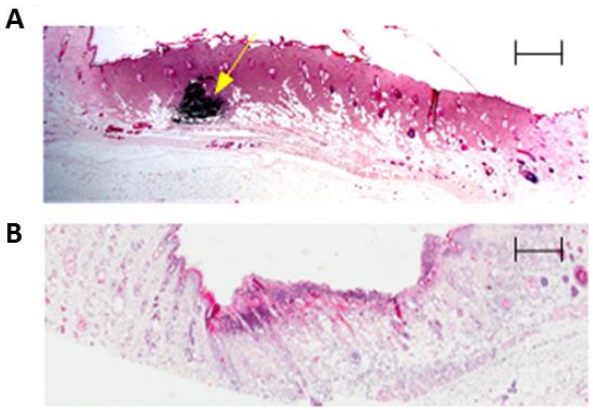

Figure 7-2: Representative 2X hematoxylin and eosin (H&E) staining of a full thickness wound (A) and a partial thickness wound (B) 72 h post burn induction. Coagulation and red brick myocardial necrosis in the dermis and subcutaneous layers are used to classify A, as full thickness. An intradermal fiducial marker (solid yellow arrow) is clearly visible. *Scale bar*, 800 µm. Revascularization of tissue as well as intact subcutaneous and muscle layers are used to confirm B, as partial thickness. *Scale bar*, 600 µm.

THz images of the rat abdomen prior to inducing a full thickness and partial thickness burn (**Figure 7-1 (a)**) display mostly uniform THz reflectivity across the FOV. Companion mean T_2 times of the epidermis (T_2=34±5 ms), dermis (T_2=26±7 ms), and hypodermis (T_2=57±8 ms) are consistent with previously published *in vivo* MRI values for skin (t=0 min in **Figure 7-1(b)**) [49], [61].

Following thermal insult (t=90 min), THz reflectivity as well as depth-dependent T_2 and relative proton density of the burn tissue rise and fall together with a biphasic trend. As originally hypothesized, the evolution of THz reflectivity and MRI tissue measurements is not identical for each wound severity. For a full thickness wound immediately following burn induction, THz imaging captures a drop in THz reflectivity in the wound contact area (Figure 7-3**(a)-(b)**) while MRI detects an increase in relative proton density (i.e. mobile TWC) in the same burn region with respect to uninjured skin (t=0 min). This increase in relative proton density is evident across varying depths – between 172 and 688 µm – in the dermis of the burn tissue (Figure 7-3 **(a)**).

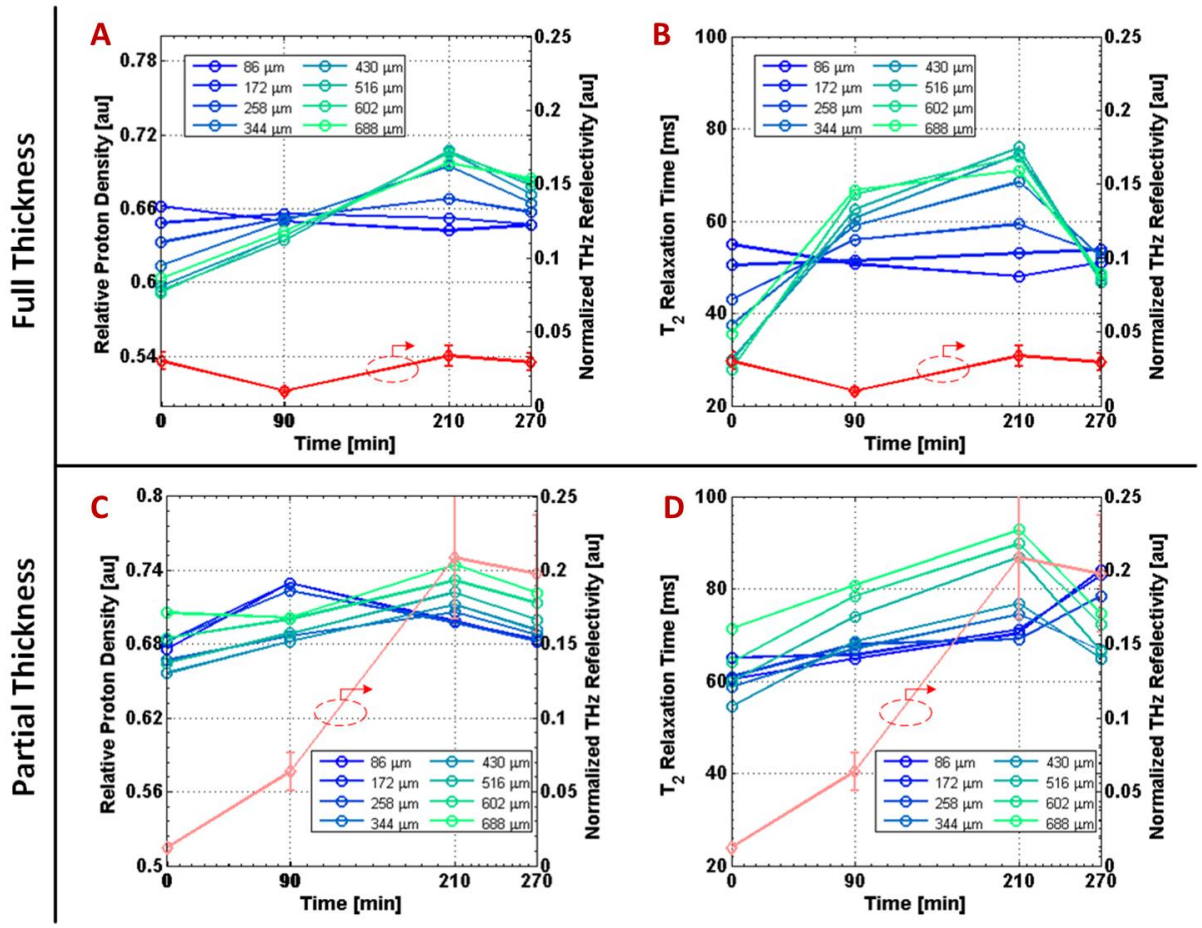

Figure 7-3: Plots comparing mean relative proton densities (i.e. mobile TWC or edema) and mean T_2 relaxation times at varying skin depths with normalized THz reflectivity as a function of time for a full thickness wound (A, B) and a partial thickness wound (C, D). Burns are induced at t=90 min. Normalized THz reflectivity is calculated from white vertical line segments delineated in Fig. 1a. Mean MRI values are generated for similar contours that segment the same burn region at specific depths in the tissue (see Methods). All green-blue depth traces correspond to the left axis of the y-y plots, while the red-pink traces correspond to the right axis. *Error bars*, ± 1 standard deviation. THz reflectivity grows and declines in parallel with MRI measurements at most depths, and their biphasic pattern is consistent with fluid shifts observed in burn edema pathogenesis. As predicted, partial thickness wounds, which experience more dermal perfusion, reveal THz reflectivity and MRI values of greater magnitude compared to those of a full thickness wound.

By comparison, a partial thickness wound is characterized by an increase in both THz reflectivity and relative proton density in the burn contact area for most depths immediately following thermal injury (Figure 7-3 **(c)**). These measurements are also greater in magnitude than those in a full thickness wound. For example, at a depth of 516 µm, relative proton density (Figure 7-3 **(c)**) and T_2 time (Figure 7-3**(d)**) for the same region of a partial thickness wound at t=90 min compared to that of uninjured skin are 3.6% and 7% greater, respectively. The corresponding

THz reflectivity for a partial thickness burn is calculated to be 7% greater than that of uninjured skin. In contrast, reflectivity and MRI differences between burn tissue and uninjured tissue are not as substantial in a full thickness wound at t=90 min.

MRI and THz parameters associated with the burn contact area both peak at t=210 min and visibly decline at t=270 min in each of the two burn severity models. For a depth of 516 μm at t=210 min the THz reflectivity, T_2 time, and relative proton density of a partial thickness wound are 20%, 45%, and 7% greater, respectively, than values in uninjured tissue. In contrast, all mean THz and MRI measurements at their temporal peak for a full thickness wound are lower in magnitude; for the corresponding dermal depth at 210 min the THz reflectivity, T_2 time, and relative proton density are 1%, 15% and 5% greater, respectively, in a full thickness wound compared to uninjured skin. Finally, a concurrent decline in mean THz reflectivity, T_2 time, and relative proton density becomes visible in both burn types by t=270 min (**Fig. X**).

7.5 DISCUSSION & CONCLUCIONS

Because edema is a generic part of the tissue injury response, it has become an important diagnostic indicator of tissue viability. In the past, edema could not be used as a diagnostic target, because the extent and distribution of cellular edema was difficult to qualitatively or quantitatively assess under the microscope; even with increases as large as 100% in cell volume, the cellular diameter increases by only 26% [185]. Although electron microscopy may reveal the presence of edema features including membrane blebbing, detachment of actin filaments, and swelling of the endoplasmic reticulum, this technique is not suitable for assessing the regional extent and distribution of edema, especially in patients. *In vivo* imaging methods, such as MRI and CT, have augmented this but are still financially and practically incompatible with a range of edema-related applications. Moreover, the lengthy acquisition times required to obtain an image render these technologies unsuitable for detecting or monitoring the acute, and often rapidly developing onset

of edema. Early visualization of fluid shifts, therefore, specifically calls for TWC imaging capabilities on the order of minutes for a FOV that spans the injured area.

By comparing THz imaging to MRI, which relies on TWC to generate contrast, we demonstrate that it is possible to use reflective THz imaging to rapidly and non-invasively track fluid shifts in an *in vivo* injury model with excellent contrast and sensitivity. Differences in THz image contrast between both burn models become evident immediately following injury (t=90 min) and reflect THz-tissue interactions known to characterize thermal insult of tissue [6]. An electromagnetic modeling of THz-tissue interaction predicts that the THz reflectivity of a tissue system imaged at our center operating frequency (~525 GHz) increases approximately linearly with increasing TWC [168]. Combining this information with what is known about burn edema pathogenesis, full thickness wounds are hypothesized to first experience an immediate, localized drop in mobile TWC (i.e. transient cessation of vascular perfusion), and therefore an initial decrease in THz reflectivity, followed by a gradual increase in TWC [80].

By contrast, a partial thickness wound is characterized by immediate and greater mobile TWC (i.e. pronounced arteriolar vasodilation), and therefore greater THz reflectivity from the time of burn induction [64], [80]. Since the amount and the physical state of water in tissue directly affect T_2 relaxation time and relative protein density, these parameters can be used to identify and quantify edema associated with each burn model [186]. Specifically, burn-induced edema is reflected by an increase in T_2 and proton density, both of which are directly correlated with greater TWC [187]. The expected trends and magnitudes of these parameters are consistent with THz and depth-dependent MR measurements for both a full thickness and partial thickness wound at t=90 min.

While both MRI and THz data peak at t=210 min for both burn models (Figure 7-3), peak values observed in the partial thickness wound are greater than those of a full thickness wound. These findings agree with well-established reports of peak edema being greater in partial thickness burns than in full thickness burns due to a marked decrease in dermal perfusion as burn

depth increases [80], [86]; partial thickness burn tissue is characterized by higher total water content, that is proton density sensitive, and greater macromolecule content [187]. A coincident increase in water binding capacity, that is T_2 sensitive, collectively results in greater magnitudes for both T_2 time and proton density in partial thickness wounds. Deeper layers of partial thickness wounds are also known to have increased edema, which is reflected in the higher mean relative proton densities that characterize MR measurements at greater depths (Figure 7-3(c)) [80]. The concurrent decline in THz and MRI parameters in both burn severities by t=270 min (Figure 7-3) is consistent with the start of the final resorption phase of the edema response [64].

In both burn models, THz reflectivity of burn tissue correlates with parallel measurements of depth-dependent relative proton density as a function of time (Figure 7-4). Strong positive correlations are evident at greater depths in the dermal tissue: at 688 µm, temporal coefficients (*ρ)* computed with normalized cross-correlation are as high as 0.97 and 0.86 for a full and a partial

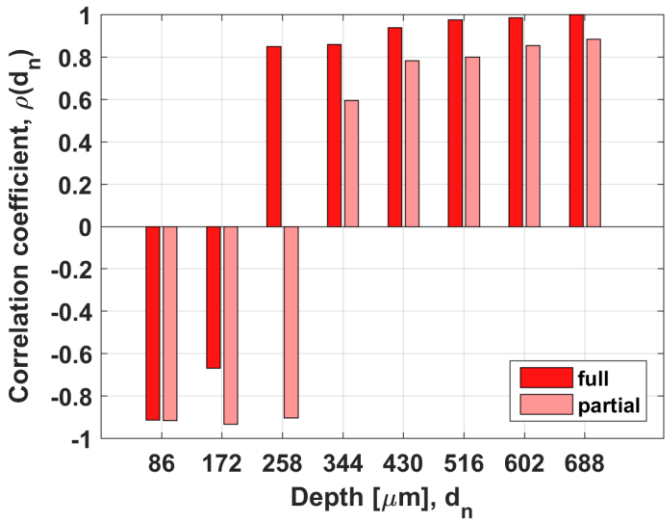

Figure 7-4. Temporal normalized cross-correlation coefficients were computed from THz reflectivity profiles and relative proton density profiles, which vary with depth, for both a partial thickness (pink) and full thickness (red) wound. THz reflectivity and MRI measurements of uninjured skin for the full thickness wound were excluded. The horizontal axis corresponds to the variable d_n in equations 2 and 4 in the Methods section. The vertical axis corresponds to $\rho(d_n)$ in equation 4 of the Methods section. Temporal correlations performed at greater depths result in large, positive coefficients (ρ) while the surface layers of the dermis display strongly negative behavior. The crossover point at ~ 258 µm is just beyond the dermoepidermal junction. The depth-dependent variation in the temporal correlation coefficients is also correlated between the wound severities. Results from both wound models suggest that mobile TWC strongly contributes to the overall observed THz contrast and that THz imaging tracks water movement at depths in tissue that may be useful for edema assessment.

thickness wound, respectively. Depth-dependent variation in *p* is also correlated between the wound severities. These results suggest that mobile TWC strongly contributes to the observed THz imaging contrast, and that THz imaging tracks movement of water at depths in tissue that are relevant to edema assessment [64], [80], [84], [86], [102].

THz reflectivity and companion TWC measurements of the upper dermis (at 86 μm and 172 μm) are anti-correlated, and these depths correspond to skin layer interfaces that likely traverse the dermoepidermal junction [49]. Further work is being performed to explore the potential thin film-like properties of these layers and to ascertain if changes in signal are due, in part, to wave interference effects. Conversely, because MRI signal varies markedly at tissue boundaries, anti-correlations at these depths may also be due to system-related constraints and not pathophysiology.

From a technological standpoint, the TWC shifts that we observed with THz and MR imaging are the first to be imaged *in vivo* for both modalities. Their biphasic pattern and distinct magnitudes also correspond with burn edema pathogenesis commonly observed in partial and full thickness wounds [80]. Although a powerful tool, MR imaging of the skin, at present, functions mainly as a research technique. Slow data acquisition times, cost, and limited access essentially preclude the use of MRI for the detection of processes such as acute inflammation or edema. Although the spatial resolution of THz images is generally inferior to that of images generated by high-field animal MRI, the transverse resolution is on par with clinical MRI systems. Furthermore, the high contrast and speed (with respect to T_{2W} MRI) of THz imaging, combined with sensing capabilities that correlate with those of TWC-based MRI, support the potential of THz imaging for applications in which surface tissue edema underlies the physiology of interest. Future efforts should facilitate the translation of THz technology for clinical use through improvements in imaging speed and optical architectures. These advancements may enable both timely and informed mapping of tissue edema and the extent of fluid extravasation into tissues in patients sustaining severe burn injuries, trauma, or other medical conditions leading to fluid shifts [188].

CHAPTER 8: INDEPRENDENT MRI OF BURN WOUNDS *IN VIVO*

8.1 MOTIVATION

The pilot, concomitant THz-MRI imaging study of *in vivo* burn wounds demonstrates TWC correlates with THz reflectivity at multiple depths in the wound bed, and, therefore, strongly suggests TWC is responsible for THz image contrast. It is important to note, however, the subject was transferred/exchanged between both modalities during imaging. For the sake of completeness and to verify possible contributions of system-related effects to observed TWC image contrast, an independent, continuous MRI and THz imaging study of burn wound is warranted. Here, continuous T_2w MRI imaging of a partial thickness and full thickness wound was performed in an *in vivo* pre-clinical rat model over a 4 hr period and variation of TWC image contrast was observed. MRI burn imaging results were compared to preliminary THz-MRI images to confirm trends in MRI image contrast were solely due to edema pathophysiology and not physical perturbations from repositioning the subject between scanning.

8.2 MATERIALS & METHODS

8.2.1 Injury-Induced Cutaneous Edema

See section 7.3.1.

8.2.2 Imaging System

See section 7.3.2.

8.3 RESULTS AND CONCLUSIONS

Continuous T2w imaging of a partial thickness and full thickness wound is shown in **Figure 8-1**: Continuous MRI scanning of a partial thickness and full thickness burn. In the control image, prior to burn induction, the red *, yellow +, and blue > indicate the location of the epidermis, dermis, and hypodermis, respectively. The solid arrow and dotted yellow arrow denote the spatial

location of the burn contact area and the formation of edema, respectively. Both time-series image sets afford the location of the burn contact region (denoted by the solid red arrow) immediately following burn induction at t=90 min and indicate the formation of

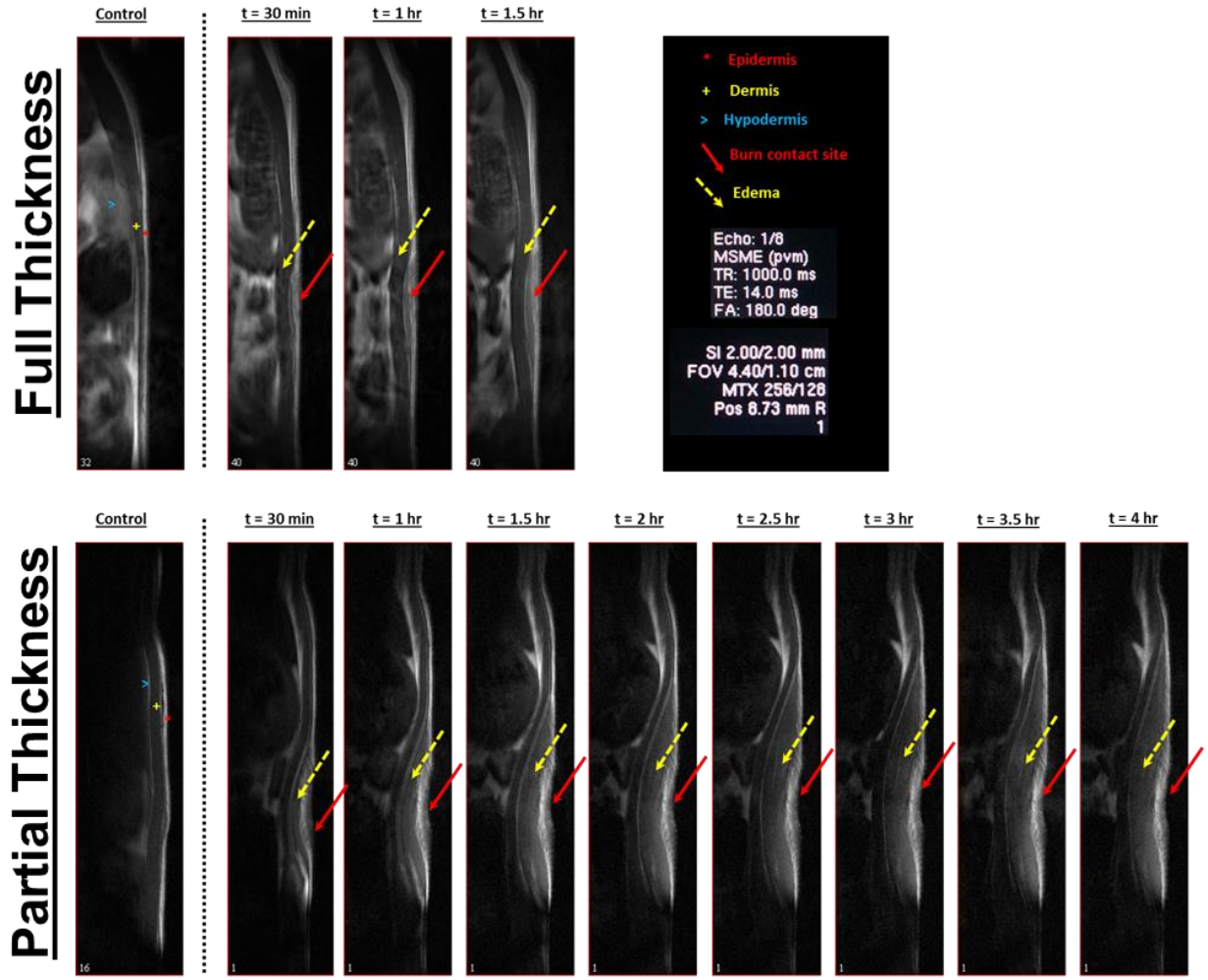

Figure 8-1: Continuous MRI scanning of a partial thickness and full thickness burn. In the control image, prior to burn induction, the red *, yellow +, and blue > indicate the location of the epidermis, dermis, and hypodermis, respectively. The solid arrow and dotted yellow arrow denote the spatial location of the burn contact area and the formation of edema, respectively.

edema over time (denoted by dashed yellow arrow). Mobile TWC, or edema, is observed as an increase in signal intensity and expansion of the dermis, which is more pronounced in the partial thickness burn. This result both agrees with previous reports of edema pathogenesis and trends observed in the pilot THz-MRI burn imaging study. Consequently, changes in image contrast observed in both studies are solely due to burn physiology as opposed to system-related artifacts

from transferring the subject between imaging modalities. It is worth noting that fewer time points were acquired in the case of the full thickness burn due to stress that the animal experienced while inside the MRI scanner.

CHAPTER 9: ADVANCES IN *IN VIVO* THz WOUND IMAGING

9.1 MOTIVATION

We have previously reported on reflective terahertz (THz) imaging, a non-invasive technique, that uses variation in tissue water content (TWC) – the direct indicator of edema – to generate native, pathology-specific tissue contrast. THz radiation is non-ionizing and has demonstrated high contrast in reflection imaging of TWC in burn wounds *in vivo* [13]–[17]. The dielectric properties of water at THz frequencies (100 GHz to 10 THz range) yield easily detectable changes in THz reflectivity for small changes in hydration. Consequently, TWC is an effective contrast mechanism in THz wound imaging [6], [7], [9], [10], [13], [15], [129], [141], [165]. Our previous THz burn results suggest that variations in spatiotemporal THz-TWC measurements between partial thickness and full thickness burn wounds are statistically significant when imaged under a dielectric Mylar window within the first few hours of injury [133]. Partial thickness burns demonstrate significant decreases in TWC in the burn contact area and localized increases in TWC in the adjacent tissue. By comparison, full thickness burns display a global increase in TWC. Although these THz burn studies yielded THz TWC signatures of edema, the pathogenesis of fluid shifts secondary to thermal injury is incompletely understood and in direct contrast to clinical observations of burn-induced edema; published data on acute changes in fluid transport suggest that the accumulation of TWC in partial thickness wounds should, in fact, be greater than that in full thickness wounds [64], [80], [85]. These discrepancies stem, in part, from inherent limitations of the previous experimental methods (i.e. burn induction and image registration) and system designs used in our pilot THz imaging studies. An additional THz investigation of TWC contrast of wounds in vivo and its relationship to burn edema pathophysiology is, therefore, warranted.

Herein, we report on THz imaging methodologies that enable more effective and repeatable *in vivo* visualization of unique TWC contrast in partial thickness and full thickness wounds in a rat model. First, we implemented an effective image registration method to compare longitudinal THz-TWC based measurements and histological assessments of wound outcome. Second, a fine-adjustment burn induction method was used to apply controlled, uniform wounds of either full thickness or partial thickness severity in the abdominal skin of rats. Finally, an optical window mount was developed to exchange dielectric windows that mitigate effects from surface irregularities in THz imaging. Reflective THz imagery (n=26 images/subject) of partial thickness and full thickness wounds were acquired with a thin-film Mylar (n = 1.5, 12 μm) and quartz (n = 2.1, 500 μm) window to track the distribution of TWC (i.e. edema) throughout the wound bed over a period of 72hr. THz burn maps were co-registered to temporally and spatially matched histological assessments to confirm wound severity in both burn models. We hypothesized that these methods would: 1) enable repeatable THz imaging of unique burn edema responses, and 2) THz-TWC maps of these fluid shifts reveal unique and significant differences in THz image contrast. Dielectric window selection, explored here for the first time, was evaluated for its sensitivity to THz imaging signal changes in specific burn wound regions. Histograms of pixel intensities within the burn contact area and uninjured tissue were computed to determine the effects of dielectric windows on THz burn image contrast. A non-invasive imaging technique for diagnosing differences in the burn wound edematous response is a much needed tool for rapid and accurate clinical burn assessment.

9.2 MATERIALS & METHODS

9.2.1 Animal Preparation

All experiments conformed to the guidelines set out by the Institutional Animal Care and Use Committee (IACUC). Four (n=4) 14 week old male Lewis rats (Harlan Laboratories, Hayward,

CA) weighing 300 - 350 g were used as pre-clinical models to investigate effects of burn wound severity on TWC maps acquired with reflective THz imaging. While pigs are a more appropriate genomic model of human skin, THz imaging in bulk tissue is insensitive to molecular-based mechanisms [184]. Rats are also widely available, convenient in size, and tractable in nature, lending them as an attractive preclinical model [91], [147]. Finally, there are few known differences in edema physiology between rats and other candidate animal models. Here, two wound models, partial thickness (n=2) and full thickness (n=2), were compared.

Animals underwent general anesthesia with inhaled isoflurane and were placed on a water heating pad for temperature regulation at 37±0.5°C. Each rat was shaved from scapula to pelvis to expose a 6 x 6 cm2 area of abdominal skin and three green tattoos were applied to the abdomen (Figure 9-1); intradermal fiducial tattoo markers allow for image registration between

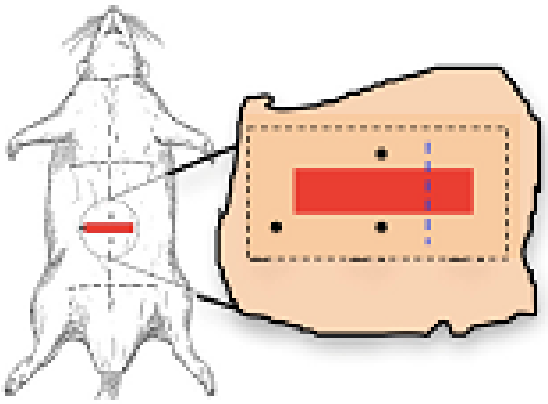

Figure 9-1: Image registration design. Three tattoo fiducial markers were intradermally administered in the abdominal skin to co-register histological burn outcome with THz-TWC maps of burn wounds.

the THz and visible images and histology. Specifically, histological slices of burn tissue that contain a fiducial marker are spatially mapped to the visible time-series imagery to assign burn severity to discrete locations within the burn. Burn protocols often produce mixed severity wounds where the depth of injury can be difficult to characterize, necessitating sampling from multiple sites [189]. Intradermal injections of non-metallic green ink were administered via a sterile 28G needle to form the apices of a right triangle. Once tattooed, the rats were awoken and allowed to

recover for 72hr or until inflammation subsided.

9.2.1.1 Uninjured Skin

Prior to burn wound imaging, a THz control (i.e. uninjured skin) study was performed in two rats to observe potential changes in THz reflectivity due to window-related pressure effects in the captured FOV. Anesthetized rats were placed in supine position on the internal heating pad under the THz imaging system, a dielectric window (i.e. either 12.7 µm Mylar or 500 µm quartz) was lowered onto the shaved abdominal skin to flatten the imaging field, and visible and THz images were captured with a SLR camera and the THz imager, respectively, over a 7hr period. Profiles of normalized THz reflectivity values across the skin were generated every 15min for the first 2hr and every 30min for the remaining 7hr to observe any window-related effects on THz image contrast

For the two remaining rats, a single THz scan and photograph were acquired of the uninjured abdominal skin under the quartz dielectric window. Image acquisition time of THz scans covered a 6 x 6 cm2 FOV. The scanned area of the abdomen was marked with a black marker, and the anesthetized rats were returned to the surgical field.

9.2.1.2 Burn Wound Induction

The rats were then subcutaneously administered buprenorphine (i.e. analgesic), aseptically prepared with three alternating scrubs of betadine and isopropanol, and randomly assigned to receive either a partial thickness or full thickness burn wound (**Table 7**).

A 2 mm x 19 mm rectangular brass brand secured to a thermocouple (OMEGA, Stamford, Connecticut) to accurately monitor the absolute temperature of the brand. The brand was heated to 200°C and 130°C using a hot plate, positioned between the fiducial markers using a high-precision manual z-stage, and applied to the abdomen with a constant pressure for 10s to induce a full thickness and partial thickness burn, respectively [9], [15] (Figure 9-2). Each rat received

one burn to minimize the total burned body surface area, thus reducing effects of shock on the

Table 7: EXPERIMENTAL PARAMETERS

Degree	*ID*	*Weight*	*Quartz/Visible Images (#)*	*Mylar/Visible Images (#)*
Partial Thickness	A	320	22 / 22	4 /4
	B	346	22 / 22	4 / 4
Full Thickness	C	324	22 / 22	4 /4
	D	348	22 /22	4 /4

physiologic wound response.

A 500 μm optical quartz window (i.e. refractive index of 2.1) was then lowered onto the abdominal skin. Concomitant visible and THz imagery were continuously acquired every 15 min for the first 2 hours and every 30 min for the remaining 7 hrs. Upon scan completion, the quartz window was exchanged with a 12.7 μm Mylar window, and a single THz and visible image were acquired of the wound; because a 12.7 μm Mylar window was used in our previous THz burn imaging studies, concomitant THz burn imagery was acquired with the same thin-film Mylar

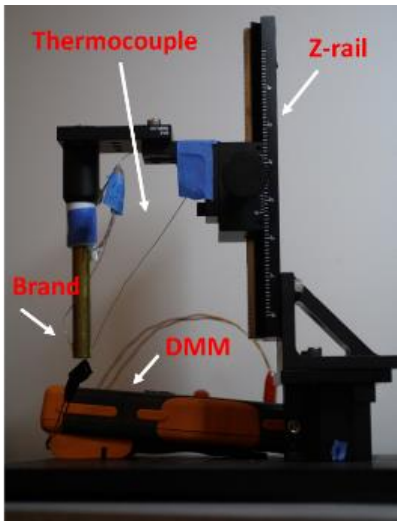

Figure 9-2: Custom burn induction apparatus. A 2 mm x 19 mm rectangular brass brand secured to a high-precision manual z-rail was used to induce uniform burn wounds with constant contact pressure. Temperature of the brand was measured on a digital multi meter (DMM) using a thermocouple.

window. The rat was then awoken and returned to the vivarium in ‘care fresh’ bedding to ensure minimum discomfort to the wound. An antibiotic (trimethoprim-sulfamethoxazole) was administered orally to prevent possible infection ensuing burn injury.

A single follow-up THz scan and photograph were captured at 24hr, 48hr, and 72hr post burn induction. At each time point, the dielectric Mylar and quartz window were lowered onto the wound during THz imaging. After a 72hr observation period, the rats were euthanized with 4% isoflurane.

9.2.2 Pixel Intensity Distributions of THz Burn Imagery

Pixel intensity distributions of time-dependent, serial THz burn imagery were performed to further analyze image contrast. Histograms of pixel intensities were generated for the Mylar and quartz windows from spatially co-registered fields of view (FOV) of: 1) the burn contact area and 2) the surrounding uninjured tissue in a full thickness and partial thickness wound. The surface areas corresponding to the burn contact site and surrounding tissue in the Mylar images at all acquired time points were manually segmented, and histograms of the enclosed pixels were then generated. These manual segmentations were then applied to parallel quartz images to ensure that the compared contrast corresponds to registered, overlapping FOVs. Because the rigid quartz window has a larger clear aperture than the flexible Mylar window, the quartz FOV for the uninjured tissue was eroded post processing to match that of Mylar.

A curved, solid line was superimposed on each plot to represent the cumulative distribution function (CDF) of each histogram. A dotted diagonal line was provided as a reference to gauge the skewness of the distribution - visualized as the difference between the area subtended by the CDF and the dotted line.

To further explore bias of the pixel distributions, the skewness of each histogram was computed using **equation** (15),

$$s = \frac{N^{-1}\sum_{k=0}^{N}(x_k - \bar{x})^3}{[(N-1)^{-1}\sum_{k=0}^{N}(x_k - \bar{x})^2]^{3/2}} \quad (15)$$

where $\bar{x}$ is the pixel population mean and N is the total number of samples in the population. The results were plotted as red and blue bars to indicate the skewness of the pixels obtained with Mylar and quartz, respectively.

9.2.3 Histology

A blind histological analysis of burn tissue harvested at 72hr post burn induction was compared to visible and THz imagery to determine wound severity in both burn models. 1.5 cm x 2 mm sections of tissue along the rostrocaudal axis were harvested from the left, center, and right regions of each burn, transferred to 10% formalin solution, and submitted for histopathological evaluation. All tissue samples were histologically sectioned sagittally to the major axis of the sample and most contained an intradermal tattoo (i.e. fiducial marker) for orientation and registration of the tissue specimen. Three histological slices of 5 µm thickness were acquired from each tissue block and stained with hematoxylin and eosin (H&E). Histology sections included both injured and uninjured tissue, providing a control area which the burned area could be compared to. Light microscopy was used to examine the burn slices, followed by analysis of the observed structural tissue damage to assign burn severity. Figure 9-3 summarizes all the experimental steps, including histology, that were performed during the THz burn wound study.

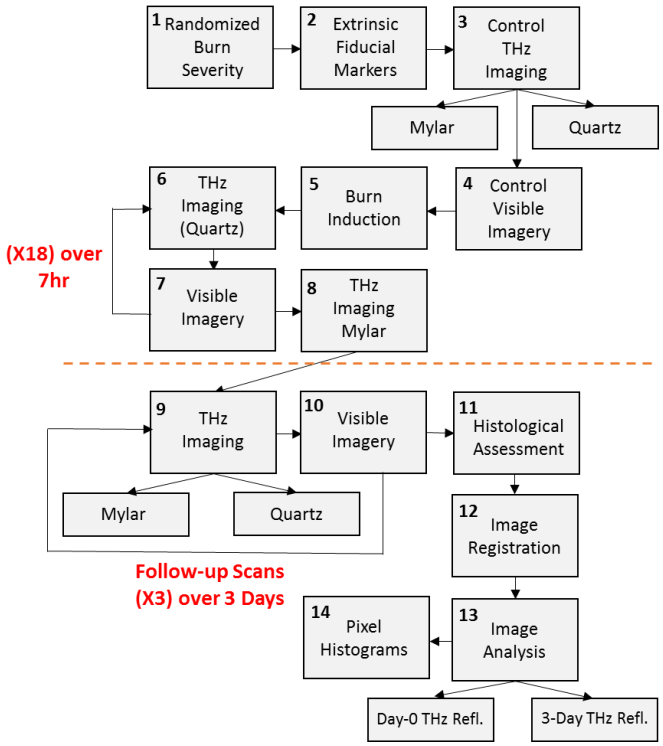

Figure 9-3: Schematic of THz wound imaging methodology. Steps 9-13 (i.e. boxes below the dotted red line) were performed after Day 0.

9.3 RESULTS

9.3.1 *In Vivo* THz Imaging of Uninjured Skin

To investigate potential effects from window-related pressure on THz burn imaging contrast, time-series THz imagery of uninjured abdominal skin in two anesthetized rats was continuously acquired using either the quartz or Mylar window over a 7hr period (Figure 9-4**(a)-(b)**). This time window is identical to that used in our previous THz burn imaging studies and is motivated by the evolution of the acute wound response following cutaneous injury [9], [66]. Over this time course, negligible changes in THz image contrast were visually apparent, and therefore a single representative THz image is included for each dielectric window (Figure 9-4). The “hot” color map associated with THz imagery transforms black to the global minimum THz reflectivity and white to the global maximum THz reflectivity. For THz images acquired with a Mylar window,

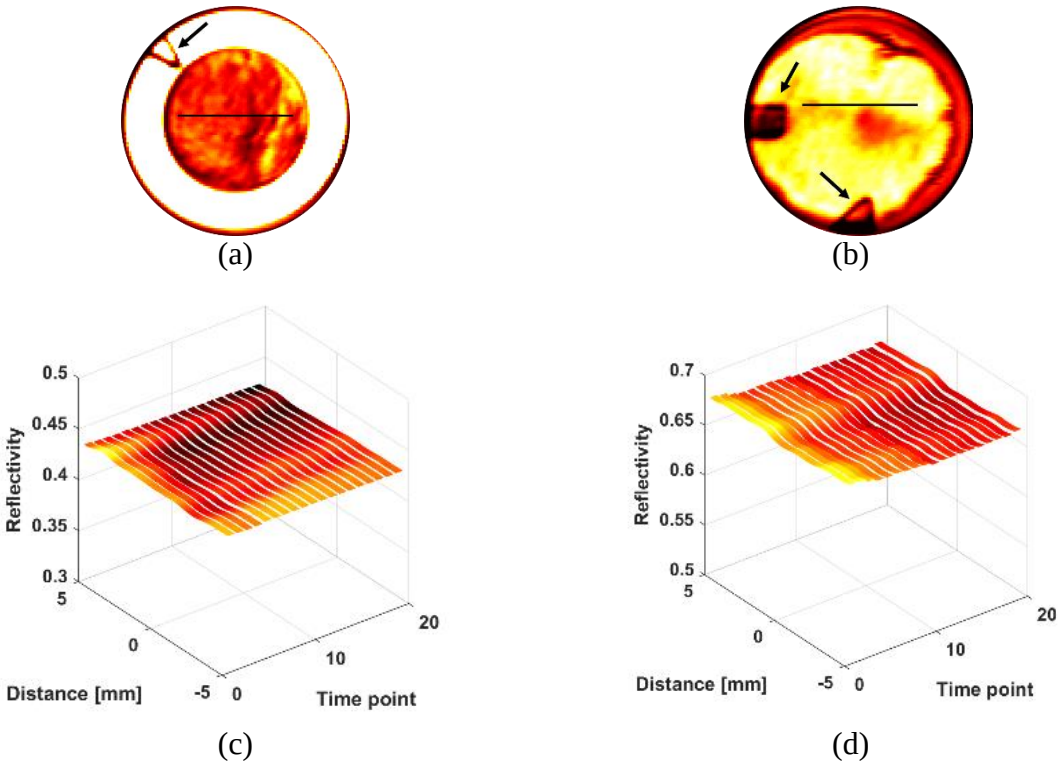

Figure 9-4: Representative THz imagery of uninjured skin under (a) a 12 µm Mylar window and (b) a 500 µm quartz window at 7hr. The hot color map transforms black to the global minimum THz reflectivity and white to the global maximum. Black arrows denote the location of external fiducial markers used to co-register visible and THz imagery. Normalized time-series THz reflectivity profiles were generated for black horizontal contours that captured uninjured skin imaged under a (c) 12 µm Mylar window and (d) 500 µm quartz window. Reflectivity profiles were generated every 15 min for the first 2hr and every 30min for the remaining 7hr. Little change in THz reflectivity was observed as function of time. Therefore, irrespective of substrate choice, pressure-related effects from dielectric windows on THz skin contrast are negligible.

the field of view (FOV) includes a highly reflective brass ring along the periphery that functions as a calibration target. Both dielectric windows contain absorbing films cut into triangular and square shapes, and these serve as fiducial markers (i.e. denoted by a solid black arrow) to enable registration of visible and THz images (Figure 9-4**5(a)-(b)**). Because both windows were kept stationary during continuous THz scanning, all THz images were inherently registered in each subject.

For all time-series THz imagery acquired over 7hr, reflectivity profiles were generated for contours, indicated by black horizontal line segments in THz imagery in Figure 9-4**(a)-(b),** that span the uninjured skin (Figure 9-4**(c)-(d)**). THz reflectivity values of these contours were normalized to the maximum THz reflectivity acquired from an aluminum calibration target (i.e.

ideal reflector) and zero THz reflectivity measured in the absence of a reflecting target (i.e. air). The calibrating reflector was positioned in the same manner and stand-off distance as abdominal skin during the control study.

THz images of the rat abdomens (Figure 9-4**(a)-(b)**) under both mylar and quartz displayed mostly uniform reflectivity across the FOV. Low reflecting areas, such as those evident in the periphery of skin imaged with quartz, may have resulted from reduced contact coupling between the window and underlying skin. The observed THz image contrast for both dielectric windows remained mostly unperturbed over the entire 7hr scanning period. This result was further substantiated by companion THz reflectivity profiles (Figure 9-4**(c)-(d**)) that suggested little to no change in reflectivity for skin as a function of time. As expected, normalized THz reflectivity of skin imaged under quartz was greater than that using Mylar due to the greater dielectric constant of quartz [155].

9.3.2 *In Vivo* THz Burn Imaging and Visual Observations

In vivo time-series THz and visible imagery of partial thickness (i.e. Rat A and Rat B) and full thickness (i.e. Rat C and Rat D) wounds in the abdominal skin of anesthetized rats was continuously acquired under quartz (Figure 9-5). Green ink dots apparent in the visible image sets for all subjects are intrinsic tattoo fiducial markers that were used to compare histological wound outcome at 72hr with THz frequency reflectivity measurements. Histological features in burn wounds are known to manifest by 72hr following thermal insult, and therefore this time was used as the endpoint of the THz burn imaging study.

THz images of the rat abdomens prior to burn induction of both wound severities displayed mostly uniform reflectivity across the FOV. As previously described, low reflecting areas evident in the upper right quadrant of the FOV may have resulted from reduced contact coupling between

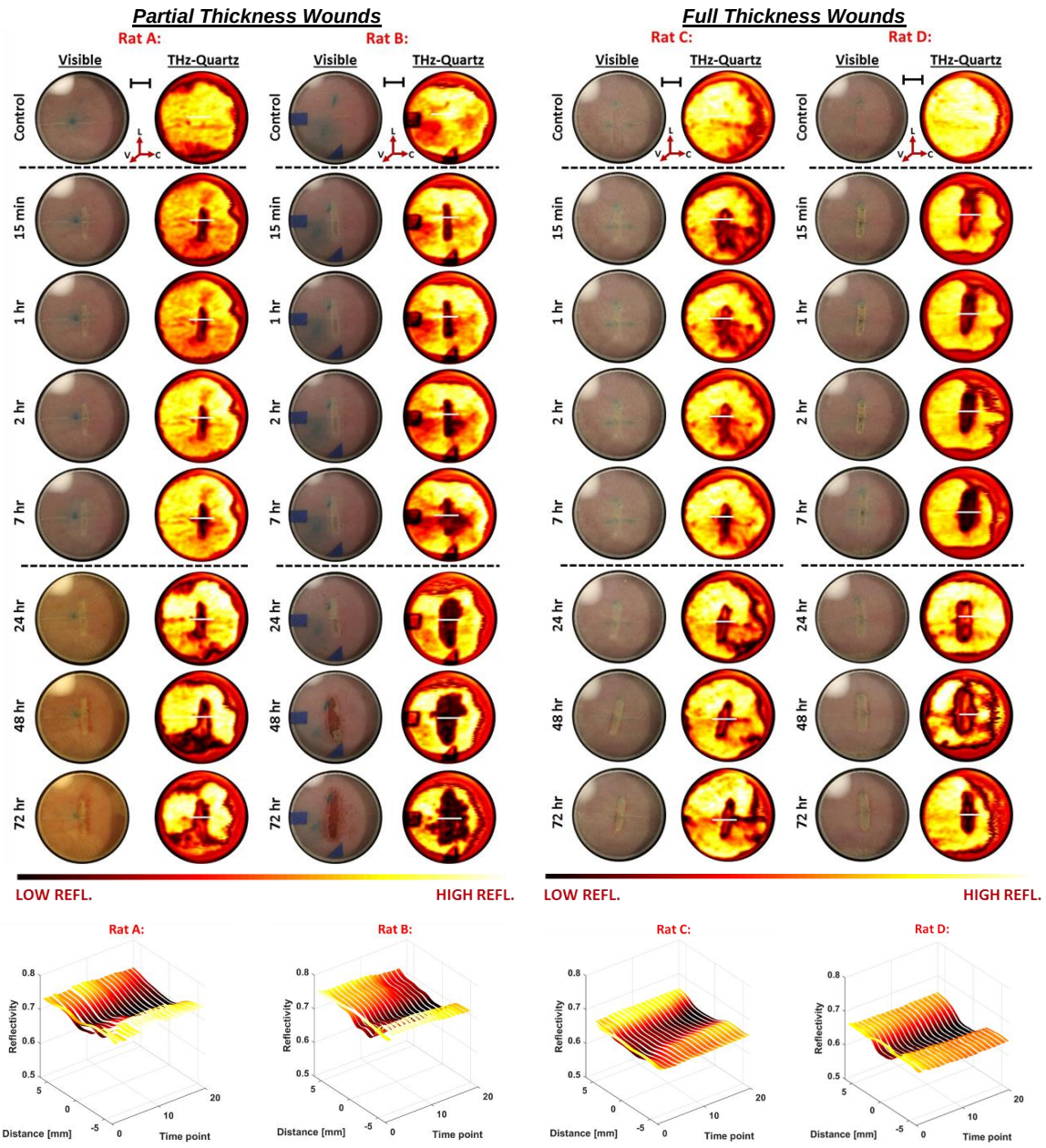

Figure 9-5: Longitudinal THz and visible imagery of partial thickness and full thickness wounds imaged under a 500 µm quartz window over 72hr. The hot color map transforms black to the global minimum THz reflectivity and white to the global maximum THz reflectivity. "L," "V," and "C" in the 3D axis denote the lateral, ventral, and cephalic anatomical directions, respectively. Horizontal scale bars represent ~1 cm in the FOV. ~1 cm long contours, indicated by solid white horizontal lines in THz images, capture the burn contact region over 7hr, 24hr, 48hr, and 72hr. Day 0 normalized THz reflectivity profiles of burn wounds spatially map to their respective horizontal contours. Reflectivity profiles were generated every 15 min for the first 2hr and every 30min for the remaining 7hr.

the quartz window and underlying skin. Only the central area of the FOV (i.e. location of burn induction) is analyzed, therefore contributions from non-uniform THz contrast observed in these peripheral regions to reflectivity measurements are minimal.

Immediately following burn induction, THz images for partial thickness and full thickness wounds revealed unique THz contrast as well as identified the spatial location of the burn contact area (Figure 9-5). Specifically, local variation in THz reflectivity was evident for this region with respect to the surrounding non-traumatized tissue. In partial thickness wounds (i.e. Rat A and Rat B), both visual inspection of THz imagery and normalized reflectivity profiles generated for the burn contact area indicate reduced reflectivity in this region that persists over 7hr (Figure 9-5). Both Rat A and Rat B exhibited an ~11% drop in THz reflectivity with respect to the surrounding normal tissue. In comparison, little to no gross changes in the wound were detectable by visible inspection during the first 7hr following thermal injury.

By 48hr post burn induction, anatomical changes at the wound site become visually apparent for partial thickness burns. While the burn in Rat A remains mostly intact, that of Rat B displays early signs of ulceration, in which the topmost skin layer is completely delaminated exposing the underlying dermal tissue. Changes in THz burn contrast, however, manifest 24hr prior to standard clinical observations. While reduced THz reflectivity characterizes the burn contact region under quartz for both subjects on Day 0, THz imagery for Rat A at 24hr shows two interesting features at the wound site: a central area of high reflectivity enveloped by a thin annulus of low reflectivity. This THz burn feature continues to grow in dimension by 72hr, but is absent in Rat B. THz imagery of Rat B at 24hr reveals low THz reflectivity at the wound contact area, similar to that observed on Day 0, which expands spatially as a function of time.

As originally hypothesized, time-series THz imagery of full thickness burn injuries imaged under quartz reveal variation in THz reflectivity that differs markedly from that for partial thickness wounds (Figure 9-5). At the outset of injury, THz contrast of the burn contact area for both Rat C and Rat D immediately includes the central wound feature that first manifests in THz imagery of

partial thickness wounds at 24 hr. However, the central area appears to be higher in reflectivity and more pronounced in size in full thickness injuries than in partial thickness wounds. In terms of *change* in reflectivity between the burn contact area and the surrounding uninjured tissue at 7hr, this difference was lower in full thickness wounds.

Normalized THz reflectivity profiles that capture this region reveal that this change in reflectivity is, in fact, ~2 fold lower in full thickness burns than in partial thickness burns (Figure 9-5). All follow-up THz scans of full thickness wounds show the continued presence of the central wound feature apparent in THz burn images acquired on Day 0. Parallel visible imagery of Rat C and Rat D show that gross changes in the wound only manifest by 48hr ensuing thermal insult.

Burn images with the 12.7μm Mylar window showed unique image contrast for both partial thickness and full thickness burn wounds (Figure 9-6). These THz reflectivity findings are, in fact, the inverse of those in parallel quartz burn images. Images of the burn contact region of partial thickness wounds under Mylar are characterized by a localized increase in THz reflectivity

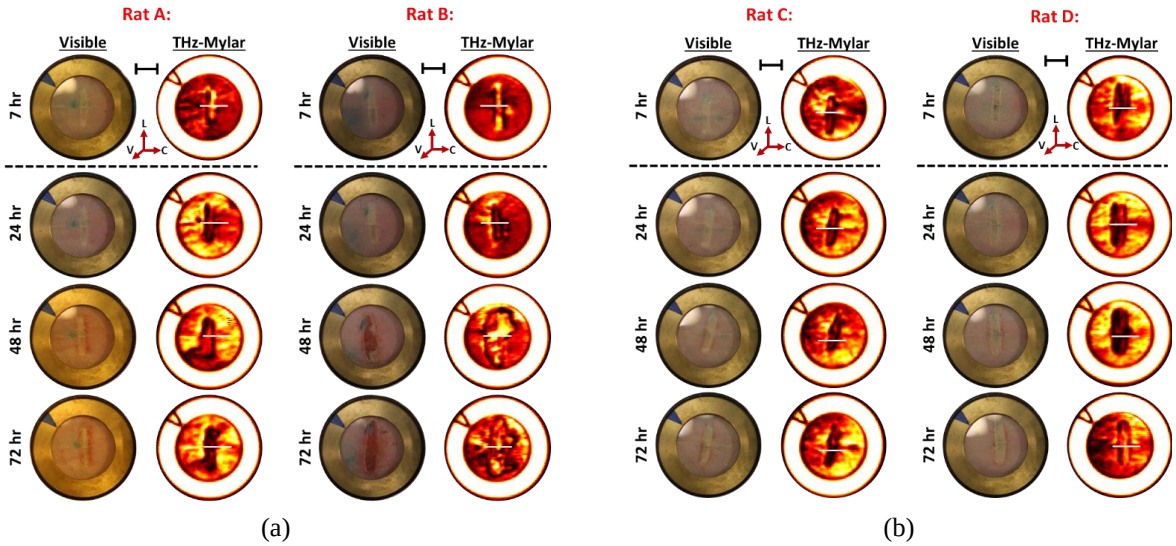

(a) (b)

Figure 9-6: Longitudinal THz and visible imagery of (a) partial thickness and (b) full thickness wounds imaged under a 12.7 μm Mylar window over 72hr. The hot color map transforms black to the global minimum THz reflectivity and white to the global maximum THz reflectivity. "L," "V," and "C" in the 3D axis denote the lateral, ventral, and cephalic anatomical directions, respectively. Horizontal scale bars represent ~1 cm in the FOV. ~1 cm long contours, indicated by solid white horizontal lines in THz images, capture the uninjured and burn contact region at 7hr, 24hr, 48hr, and 72hr following thermal injury.

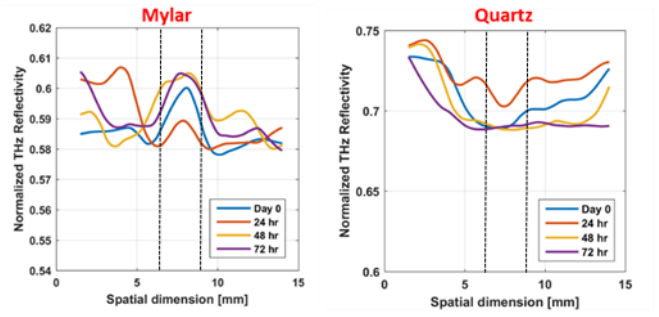

(a)

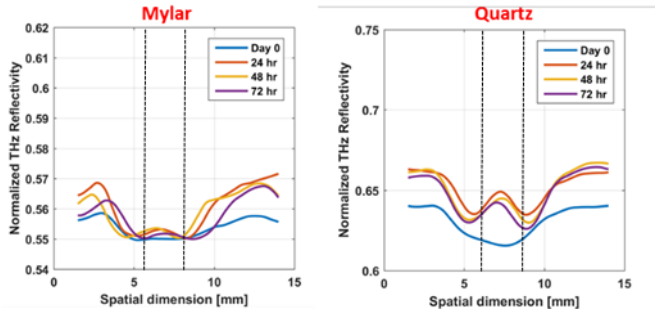

(b)

Figure 9-7: 72hr normalized THz reflectivity profiles of burn wounds. (a) All profiles spatially map to their respective horizontal contours for a partial thickness wound in Rat B and (b) full thickness wound in Rat C imaged under both a 500 µm quartz and 12.7 µm Mylar window. Dashed vertical lines indicate spatial locations of the burn margins, where the inner section and outer regions are burn tissue and uninured tissue, respectively. The results are consistent with THz electromagnetic behavior and burn edema physiology: THz reflectivity of partial thickness wounds under Mylar at ~500 GHz increases in the burn contact area, whereas an appreciable drop in reflectivity is observed in a full thickness wound for the same burn region. The inverse is true for all burn imagery acquired under quartz.

compared to that of the surrounding uninjured tissue (Figure 9-6**(a)**); the burn contact region appears as a discrete bright yellow band in both Rat A and Rat B. This result is most pronounced at 7hr post injury and somewhat diminishes by 72hr. In contrast, THz imagery of full thickness wounds (Figure 9-6**(b)**) imaged under Mylar reveal decreased reflectivity in the burn contact area at 7hr that continues to persist in the follow-up scans.

Comparison of normalized reflectivity profiles that capture the burn contact area of partial thickness and full thickness wounds quantitatively reinforce findings observed by visual inspection of THz burn imagery acquired with both Mylar and quartz windows (Figure 9-7). In Figure 9-7, vertical dotted lines indicate the spatial location of the burn margins (determined by co-registering visible and THz imagery), the inner section corresponds to the burn contact area and regions to the left and right of the lines correspond to uninjured tissue. THz reflectivity associated with the

burn contact region of a partial thickness wound with respect to uninjured tissue results in increased THz reflectivity and decreased THz reflectivity when imaged with a Mylar and quartz window, respectively. This result is consistent over the 72hr post-burn induction surveillance period and agrees with visual observations of THz burn contrast. In contrast, opposite THz reflectivity findings are true for a full thickness wound imaged with identical dielectric substrates over 72hr following thermal insult. For example, reflectivity profiles of a full thickness wound imaged with quartz show a local peak THz reflectivity at the wound center, enveloped by two localized THz reflectivity minima. This finding corresponds to the previously mentioned central wound feature observed in time-series THz quartz imagery of full thickness wounds. These distinct THz signatures confer unprecedented conspicuity for burn wound severity.

9.3.3 Histological Assessment

Histological evaluation of tissue sections acquired from both burn wound models was used to confirm burn severity (Figure 9-8). A pathologist blinded to the study samples, identified all histological sections from the right, center, and left regions of burns induced at 130°C as corresponding to uniform partial thickness burns that extended only as far as the dermal tissue (Figure 9-8**(a) and (b)**)**.** H&E stained tissue sections (5μm thick), delineating a clear demarcation between the burn and non-traumatized viable tissue, showed delamination of the epidermis and superficial dermis, pathologically termed an “ulceration.” Dotted rectangular boxes in 1x H&E images indicate an edge of the ulceration in each tissue section for Rat A and Rat B. Solid red arrows denote the location of the previously described fiducial marker in at least one histological tissue section. Intact muscle and subcutaneous layers as well as early signs of wound healing (i.e. neovascularization, granulation tissue, and collagen deposition) in 2.7x H&E images were

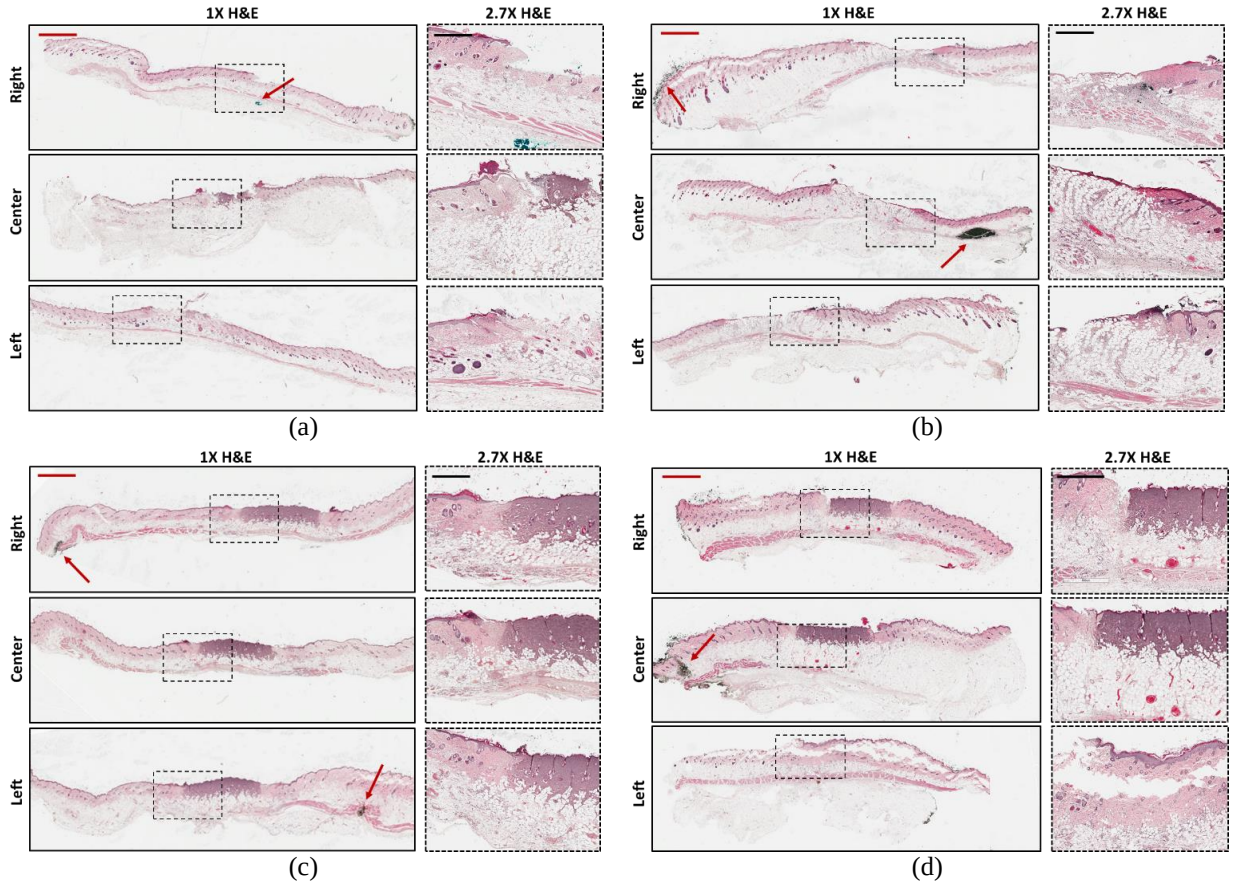

Figure 9-8: 1X and 2.7X representative hematoxylin and eosin (H&E) staining for wound sections acquired from (a) Rat A, (b) Rat B, (c) Rat C, and (d) Rat D at 72hr. Ulceration (i.e. blistering) and intact dermis and subcutaneous layers are used to classify right, center, and left histological sections of Rat A and Rat B as all partial thickness. Coagulation and red brick myocardial necrosis in the dermis and subcutaneous layers are used to classify right, center, and left histological sections of Rat C and Rat D as full thickness. In the H&E images, dotted boxes capture the burn margin. Solid red arrows denote the location of the tattooed fiducial marker for image registration with THz and visible burn imagery. The black scale bar and red scale bar represent 750 µm and 1500 µm, respectively.

used as distinguishing features to identify all 130ºC burn wounds as partial thickness injuries. The depth of injury was consistent across all tissue regions and between subjects in the partial thickness burn group thus confirming all wounds to be of uniform severity.

All tissue sections of burns induced at 200°C were histologically classified by a pathologist to be uniform wounds of full thickness injury, that extended through all the skin layers and underlying muscle (Figure 9-8**(c)** and **(d)**)**.** Injured tissue in H&E images for Rat C and D show severe cellular necrosis and vascular occlusion, and, therefore, are classified as full thickness burns. As shown in Figure 9-8, the dermis and portions of the underlying subcutaneous layers of both full thickness

wounds were stained dark purple, consistent with cellular damage and destruction [190]. The depth of injury was uniform across the length of the burn for all tissue sections (i.e. right, center, and left) harvested from both Rat C and Rat D. Similar to the histology of partial thickness burns, that of full thickness burns also included a fiducial marker in at least one tissue section.

9.3.4 Pixel Intensity Distributions of THz Burn Imagery

Histograms of pixel intensities of 72hr Mylar and quartz images of uninjured skin surrounding a full thickness (Rat C) and partial thickness (Rat B) wound are displayed in Figure 9-9. These subjects were identical to those used to compare 72hr Mylar and quartz THz reflectivity profiles between a partial thickness and full thickness wound. For uninjured tissue in THz images of a full thickness wound, the Mylar histogram resembles that of a shifted Rayleigh distribution and demonstrates a stark bias towards darker pixels. Conversely, the quartz histogram for the same tissue region shows a heavy incidence of bright pixels and is somewhat multi-modal. From the plots, it is evident that the pixels of uninjured tissue in a full thickness wound obtained with the Mylar window are biased to the left and the pixels obtained with the quartz window are biased to the right. Histograms of pixel intensities are similarly biased to the left and right for uninjured skin surrounding a partial thickness burn imaged with Mylar and quartz, respectively. However, the incidence of dark pixels is greater for uninjured tissue of a partial thickness wound obtained with Mylar compared to results observed in a full thickness wound. Uninjured tissue of a partial thickness wound imaged under quartz shows a lower incidence of bright pixel intensities compared to that of a full thickness wound.

Histograms of pixel intensities associated with the burn contact area of each wound severity model are more complex. The burn contact area of a full thickness wound imaged with

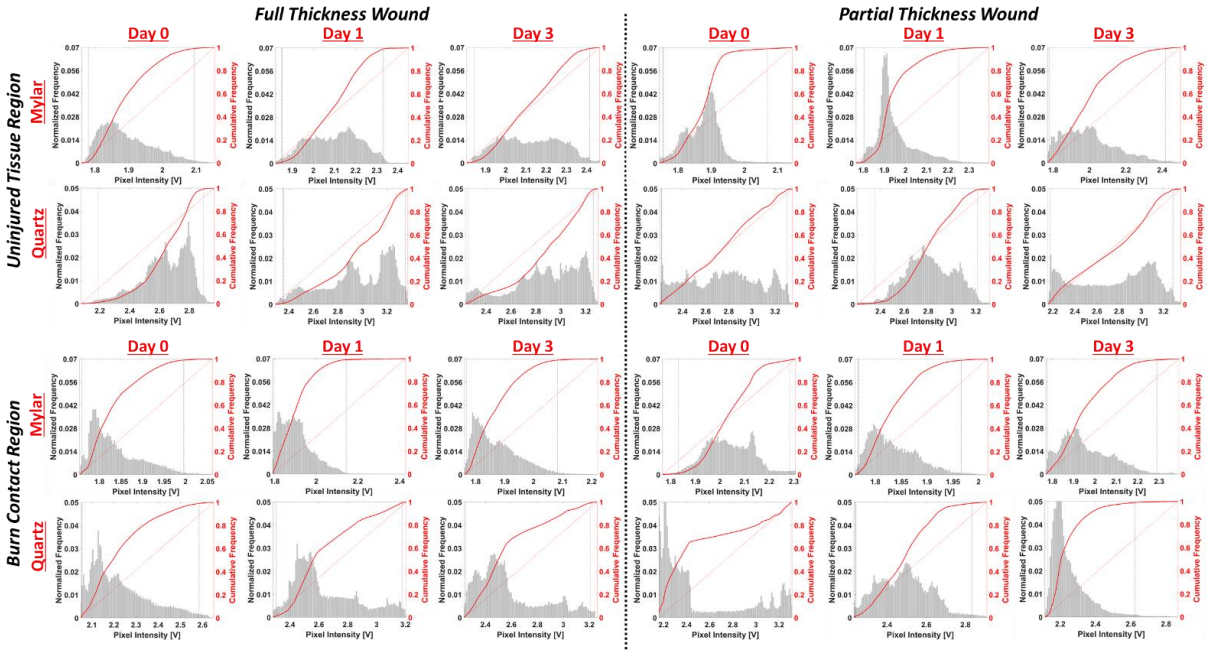

Figure 9-9: Histograms of pixel intensities of 3-Day Mylar and quartz THz imagery of uninjured skin and the burn contact region of a full thickness burn (Rat C) and a partial thickness burn (Rat B). The curved, solid line superimposed on each plot represents the cumulative distribution function (CDF) of each histogram

Mylar shows a higher incidence of dark pixel intensities compared to the same region imaged with Mylar in a partial thickness wound. In contrast, the contact area of a full thickness wound imaged with quartz shows a lower incidence of dark pixels compared to the same region imaged with quartz in a partial thickness wound.

For all the acquired THz images of uninjured tissue, the Mylar pixels are always skewed positively (left) and the quartz pixels are always skewed negatively (right) (Figure 9-10). It is also interesting to note that the time dependent variation in the skewness magnitude is correlated between the window types. For uninjured tissue imaged under quartz, the skewness of the histograms is greater in a full thickness wound. In comparison, for the same tissue region imaged under Mylar, the skewness of the histograms is greater in a partial thickness burn wound. In the case of the burn contact area imaged with Mylar, the skewness of the histograms is greater for a full thickness burn.

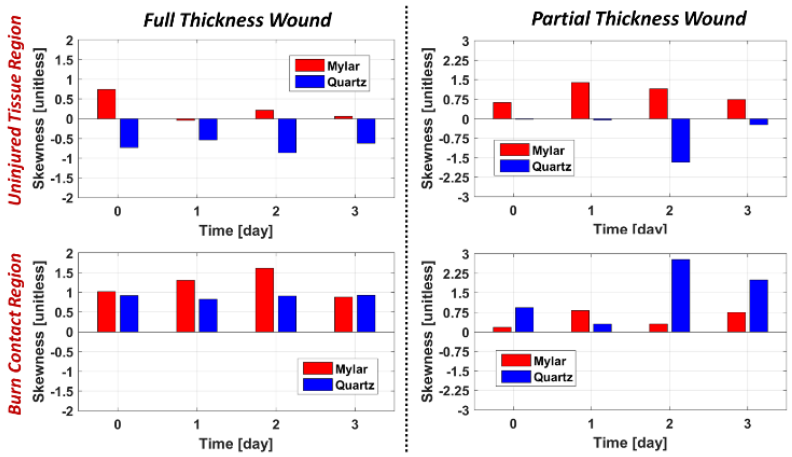

Figure 9-10: Skewness of Mylar and quartz histograms of uninjured skin and the burn contact region of a full thickness burn in Rat C and a partial thickness burn in Rat B.

9.4 DISCUSSION

Limited knowledge regarding burn edema pathophysiology is largely attributed to the difficulty associated with accurately detecting the extent and distribution of the edema process. Quantification and *in vivo* visualization of the edema process is essential for the study of edema formation and resorption and for the evaluation of therapeutic methods to decrease and, in particular, prevent conversion of a partial thickness to full thickness injury [191]. Lymph flow rate and lymph protein content have been frequently used to monitor microvascular fluid filtration rate and protein permeability characteristics [85], [192]. However, due to microvascular occlusion in deeper burns, the measured lymph flow rate in these wounds is likely to underestimate the actual degree of injury and actual edema formation. Serial skin and soft tissue biopsies that measure edema by the wet-to-dry weight are also commonly used for quantifying burn edema [69]. The high and unavoidable sampling error and invasive nature of this technique, however, make it impractical for standard clinical assessment of wounds.

Since water constitutes ~70% of the skin weight and the THz frequency dielectric constant of water is significantly higher than that of non-water constituents, burn wound edema can be monitored with reflective THz imaging, in a similar manner to that used in perfusion studies. Here,

we demonstrate it is possible to use reflective THz imaging - with the addition of improved methodologies and system designs - to track edema processes *in vivo* that are unique to burn models of varying severity. These THz imaging results are not only repeatable but are also consistent with known burn edema pathogenesis associated with partial thickness and full thickness burn wounds.

The first key improvement in this THz burn study was a precise burn induction apparatus designed to inflict a controlled depth of injury in pre-clinical models. A review of the literature, which includes some of our previous THz burn imaging results, revealed that the most commonly used burn contact methods produce mixed severity wounds for which the resultant depth of injury is difficult to classify [66], [69], [190]. For example, our previously reported burn protocol required that the experimentalist manually place a heated brand on the abdominal skin of the anesthetized animal with constant contact pressure. This task proved to be difficult in practice and all the induced burn wounds were of mixed severity [133]. The resultant THz burn maps, therefore, did not reflect unique edema pathogenesis characteristic of either a partial thickness or full thickness burn injury. To overcome this issue, we integrated a precisely controlled z-stage that enabled positional and pressure accuracy of the heated brand. All burn wounds induced with this technique were histologically verified to be distinctly either uniform partial thickness or full thickness severity. This result enabled a comparative THz imaging study of wounds of definitive burn depth. A second key improvement was that all burn wounds contained permanent fiducial markers, in the form of tattoo ink, that enabled accurate comparison of histological wound outcome with THz frequency reflectivity measurements acquired with different dielectric windows.

From a clinical perspective, the use of windows for THz burn assessment is a practical barrier to non-contact, *in vivo* medical translation of this technology. Concerns include physical perturbation of the wound, risk of contamination of the wound, and pressure exertion. Here, we show in uninjured skin that pressure-related effects of windows on THz image contrast are, in fact, negligible. Although windowless burn assessment is ideal, low-loss dielectric windows are

necessary in THz imaging to minimize confounding effects from non-planar geometries and, for example, respiratory motion *in vivo*.

While visual differences between both burn models manifest at 48hr following injury, marked differences in THz image contrast between partial thickness and full thickness wounds imaged under Mylar and quartz windows become evident immediately following injury and reflect THz-tissue interactions known to characterize thermal insult of tissue. Electromagnetic modeling of THz-tissue interactions predicts that the THz reflectivity of a tissue system imaged under Mylar at our center operating frequency (~525 GHz) increases approximately linearly with increasing TWC [6], [129]. In contrast, THz reflectivity of a tissue system imaged under quartz at the same operating frequency decreases with increasing TWC [133]. Combining this information with what is known about burn edema pathogenesis, full thickness wounds imaged under both Mylar and quartz should experience changes in reflectivity that are consistent with an immediate, localized drop in TWC (i.e. transient cessation of vascular perfusion), followed by a gradual increase in TWC (i.e. edema) [64], [80], [86], [91]. In comparison, reflectivity changes associated with partial thickness wounds imaged with both dielectric windows should reflect immediate and greater TWC (i.e. pronounced arteriolar vasodilation) [80], [85].

Immediate THz reflectivity changes associated with both partial thickness and full thickness wounds imaged with Mylar and quartz windows on Day 0 are consistent with specific trends observed in burn edema pathogenesis. Irrespective of window selection, THz-based TWC variation in partial thickness wounds is greater than that of full thickness wounds. For example, compared to uninjured skin, lower THz reflectivity associated with the burn contact area of partial thickness wounds imaged under quartz corresponds to an increase in TWC at 7hr. Similarly, higher THz reflectivity of the same region imaged under Mylar represents an increase in TWC at 7hr. Full thickness wounds imaged with the same windows, in contrast, demonstrate smaller immediate changes in TWC compared to partial thickness injuries. These findings agree with well-established reports of peak edema being greater in partial thickness burns than in full thickness

burns due to a marked decrease in dermal perfusion as burn depth increases [64], [80]. Although THz-TWC based findings observed in follow-up scans (i.e. 24hr, 48hr, and 72hr THz images) may differ among subjects in the same burn group, immediate TWC changes in the burn contact area are on par with each other. These acute results are of most clinical interest. Moreover, THz image contrast at later time points takes on a greater complexity; changes in anatomical features, including scab formation and ulceration may confound THz imaging contrast.

Histograms of pixel intensities of the wound contact area and surrounding non-traumatized tissue in full thickness and partial thickness burns acquired with Mylar and quartz windows agree with trends observed in THz burn imaging contrast as well as edema pathogenesis. Intensity histograms of uninjured tissue regions acquired with a Mylar window for both wound severities are positively skewed, where this tissue region is associated with lower pixel intensities compared to the burn contact area. This corresponds to underexposed THz image contrast around the burn site that is visually apparent in all Mylar burn imagery. The degree of skewness, however, is greater for a partial thickness wound than a full thickness wound, and is consistent with the localized “bright band” characteristic of the burn site in partial thickness wounds. Again, this feature is predicted to correspond to greater, localized edema in partial thickness wounds. In contrast, intensity histograms of uninjured tissue under quartz are negatively skewed for both wound types, where the wound contact region appears lower in pixel intensity. This result is, again, consistent with reduced THz contrast in the burn contact area of quartz THz images and lower fluid shifts that are typically observed in wounds of this severity.

However, histograms of the FOV suggest that skewness associated with each dielectric substrate, although opposite, is not exactly identical. If both windows were used to longitudinally image the same wound, and, therefore, identical tissue water content, there should, theoretically, be no variation between the magnitude of skewness associated with each window. However, a difference is observed, and this is hypothesized to be largely due to electromagnetic behavior between the tissue system and selected dielectric window. Tissue under a window is typically

modeled as a half-space, assuming that the tissue properties, including TWC, are homogenous throughout the tissue layers. However, tissue is known to be a multi-layered, complex system that is characterized by gradients [37], [43], [193]. These tissue layers may exhibit their own interference effects. The distribution of TWC along the thickness of tissue layers and the layer composition, therefore, may alter the tissue's reflectivity. Addition of a window to a multilayer system should cause the sensitivity of THz imaging to the hydration state of deeper layers to change relative to the surface layers. As a result, THz images acquired with different dielectric windows (i.e. quartz and Mylar) may vary not only in hydration sensitivity, but in information content, as the depth of tissue probed varies with the optical path length of the imaging system's window.

Future work is needed to define which dielectric substrate provides the best THz TWC wound contrast and how it may alter hydration sensitivity of THz imaging to specific types of burn wound edema. What is known to be certain here, however, is that the use of multiple windows in the updated experimental methodology enables acquisition of unique and repeatable TWC maps of wounds. Future efforts should focus on dielectric window selection as well as facilitate the translation of THz technology for clinical use through improvements in imaging speed and optical architectures. Because THz burn contrast associated with each window is both unique and consistent with known TWC trends in burn edema pathogenesis, window-driven, high-speed THz imaging could be an emerging technology for detection and monitoring of pathological conditions that lead to tissue edema.

9.5 CONCLUSIONS

Repeatable, *in vivo* THz imaging of unique fluid shifts following burn injury is accomplished with the use of improved burn induction, image registration methodologies, as well as multiple dielectric windows. Uniform burn wounds of either partial thickness or full thickness severity were produced *in vivo* with a fine-precision, contact burn apparatus in rats and imaged with a reflective

THz system over a 72hr period. THz reflection maps of burns acquired with a quartz and thin-film Mylar window demonstrated reproducible and unique changes in TWC that were consistent with trends in burn edema pathogenesis. Histograms of pixel intensities associated with the burn contact area and surrounding uninjured tissue in Mylar and quartz burn images further substantiated THz-TWC findings in burn wounds. Implementation of these techniques in reflective THz imaging may collectively be used to further investigate burn edema pathogenesis as well as more effectively track fluid shifts following cutaneous injury.

CHAPTER 10: EXPLORATION OF EFFECTS OF BURN WOUND PARAMETERS ON THz WOUND IMAGING

10.1 MOTIVATION

Burn wound imaging is an ideal candidate to take advantage of THz imaging due to the large shifts in TWC that occur as an immediate response to thermal injury. A scan of the literature will reveal a number of different protocols designed to inflict a controlled depth of thermal injury in an animal model of interest [9], [10], [153], [154], [194]. One of the most commonly applied protocols uses a reservoir of boiling water, paired with a specific contact duration time depending on the desired severity of injury [152], [195], [196]. This model is advantageous as boiling water (1) has a well-defined, extremely well controlled temperature, (2) the contact area is often flexible allowing the burn induction device to conform to the contours of the animal model, and (3) a good portion of burn wounds observed in the ER are due to kitchen accidents involving boiling liquids. However, controllability of this model can also limit the applicability as real-world burns are seldom so uniform across the injured areas.

Other groups, including ours, had explored the use of hot metallic brands to induce partial and full thickness burns [6], [10]. This technique is well known to produce mixed severity wounds and the depth of injury can be difficult to characterize. While this complicates identification and evaluation of statistically significant burn severity classifiers, candidate feature sets drawn from burns resulting from metal contact protocols may have a good chance of translating clinically.

Recently, our group has employed a version of the metal contact protocol to explore the efficacy of THz imaging in diagnosing burn severity. Prior to the start of a multi animal trial, a pilot study is being completed to confirm burn parameters including temperature and duration. The outcome of the pilot burns are evaluated with histology to confirm that the candidate parameter set produces the desired burn injury. Over the course of the program we have implemented minor changes to the protocol to improve repeatability, data collection, etc. We noticed two key things

after each protocol change: (1) statistically different contrast was maintained between partial and full thickness burns and (2) the image features used to delineate burn severity changed as the protocol changed.

It appears that there may be a many to one relationship between surface burn wound edema distribution obtained through THz imaging, and the severity of the burn as ascertained by histology. In other words many different protocols illicit the histology driven burn severity assessment but these protocols may produce starkly different looking THz derived, tissue water content maps. These observations are consistent with the current body of knowledge of burn wound physiology and suggest that many factors beyond just the thermal temperature, contribute to overall wound response [66]. To begin study of this many-to-one relationship, a pilot trial of three animals with a metallic contact protocol was completed. All animals received a burn wound with the same brand geometry and contact pressure but varying contact times. All burn wounds were evaluated by histology and determined to be deep partial thickness.

10.2 MATERIALS & METHODS

10.2.1 Surgical Preparation and Burn Induction

This *in vivo* study was approved by the UCLA Institutional Review Board (#2009-094-03b). Three male Sprague Dawley (SD) rats weighing 180- 200 g (Harlan laboratories, Hayward, CA) were used as preclinical models to investigate the effects of burn induction parameters on THz imaging contrast. Rats received one burn to minimize the total burned body surface area, thus reducing effects of shock on the physiologic response. Each rat was injected with buprenorphine (analgesic) subcutaneously 1 hour prior to induction of general anesthesia with isoflurane gas delivered through a nose cone. The skin from the abdomen was shaved to expose a 5 cm x 5 cm area of bare skin and aseptically cleaned. Rats were placed in supine position on a mount with internal heating to maintain normal body temperature during imaging. A 500 μm quartz window was lowered onto the abdomen to flatten the imaging plane and THz and visible imagery of the

uninjured skin was acquired. Upon completion of the control scans, the dielectric substrate window was removed and a circular brass brand (12.7 mm in diameter) secured to a thermocouple – to accurately monitor the absolute temperature of the brand-was heated to 130°C using a hot plate. The brand was applied with a constant pressure for a contact time of 5, 7, and 10 seconds to induce deep partial thickness burns on each rat abdomen. On Day 0, THz and visible imagery was acquired with a quartz window every 15 minutes for a duration of 3 hours to investigate the acute injury response ensuing burn induction. THz burn imagery was then acquired at 24 (Day 1), 48 (Day 2), and 72 hours (Day 3) post burn induction. On Day 3, the rats were euthanized and the burn tissue harvested for histological assessment. It is important to clarify that all wounds induced at 130 degrees °C with 5, 7, and 10 second contact times were histologically classified as deep partial thickness burns. Previous histological assessments confirm that a contact time of 10 seconds results in this burn severity, and wounds induced with lower contact times at the same temperature empirically belonged to the same burn classification [6], [9]. THz burn imagery of a 58 mm x 58 mm field of view (FOV) was acquired within 12 minutes using a 0.5 mm step size.

10.3 RESULTS

Ideally, we would like to translate changes in image contrast or the shapes of particular structures in THz data into biologically meaningful terms, such as changes in physiology and anatomy in injured tissue. *In vivo* burn wound imaging allows the progression of pathological conditions in the same animal to be monitored longitudinally over time. We hypothesized that the interpretation of changes observed from THz images acquired at different time points (Day 0, 1, 2, and 3) could be broadly studied under three classifications: 1) changes in contrast delineated as indicators of physiological changes occurring over time; 2) morphometric changes such as changes in shapes detected from THz images, which are more obviously related to anatomical changes; and 3) changes in contrast due to electromagnetic interactions between the dielectric substrate window and the underlying tissue. This preliminary study of the effects of burn

parameters, specifically burn contact times, on THz wound imaging is the first *in vivo* exploration of this hypothesis. **Figure 10-1** illustrates differences in spatiotemporal THz reflectivity profiles acquired on Day 0 of partial thickness burns induced with a circular brand for 5 sec (**Figure 10-1 (a)),** 7 sec (**Figure 10-1 (b)**), and 10 sec (**Figure 10-1(c)**) under a quartz window, where the first time point is prior to burn induction and all following time points are post burn induction every 15 minutes. The false color map transforms blue to the global minimum THz reflectivity and red to the global maximum THz reflectivity of a particular burn contact time series.

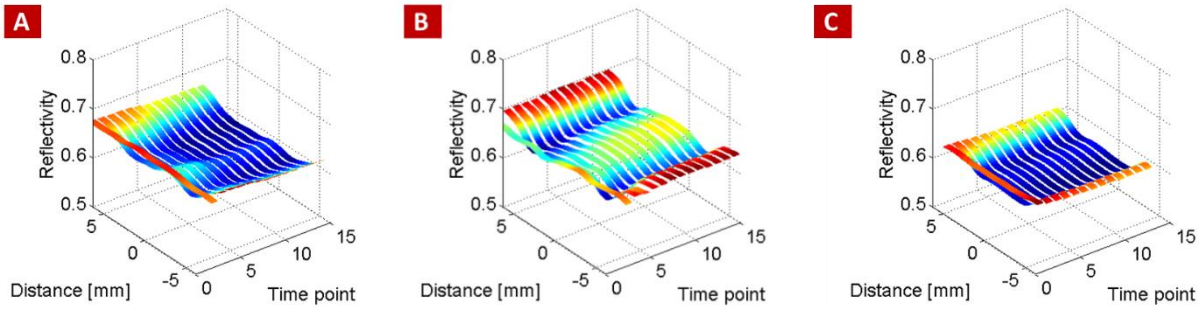

Figure 10-1: Day 0 spatiotemporal THz reflectivity profiles for partial thickness burns induced with a circular brand for (a) 5 sec, (b) 7 sec, and (c) 10 sec under a quartz window. Each time point is 15 minutes apart.

Immediately evident for all burn contact times is the decrease in THz reflectivity between the control and post burn profiles. However, comparison of the signal profiles following burn induction between each burn series reveals different behavior. For instance, the deep partial burn induced with a 5 second contact time **(Figure 10-1(a))** is characterized by a growing decrease in signal intensity (dark blue profiles) within the burn contact area, whereas this effect is lower and negligible, if not absent, in the burns induced with a 10 and 7 second contact time, respectively. Electromagnetic modeling predicts that the power reflectivity of a tissue system under quartz illuminated at a 14 degree incidence angle is frequency-dependent, and, therefore, varies non-linearly with respect to increasing tissue water content. In other words, over illumination frequencies across 500 GHz – 700 GHz, reflectance may vary from high-to-low or high-to-low-to-high with increasing tissue water content. Therefore, the decrease in THz signal may be

interpreted as a possible indicator of resultant edema, or, perhaps, the reflectance lies at a null spot in the spectral response predicted by electromagnetic modeling. Given the preliminary nature of this study (n=1 for each burn group), it is too early to make any definitive generalizations about the changes in contrast observed. It is still interesting to note, however, the noticeable changes in THz reflectivity profiles associated with wounds of identical burn severity, as determined by histological assessment, on Day 0; though not fully understood, the THz contrast is intrinsically unique for each burn series, and these findings are similarly evident in longitudinal THz imagery that spans a period of 3 days.

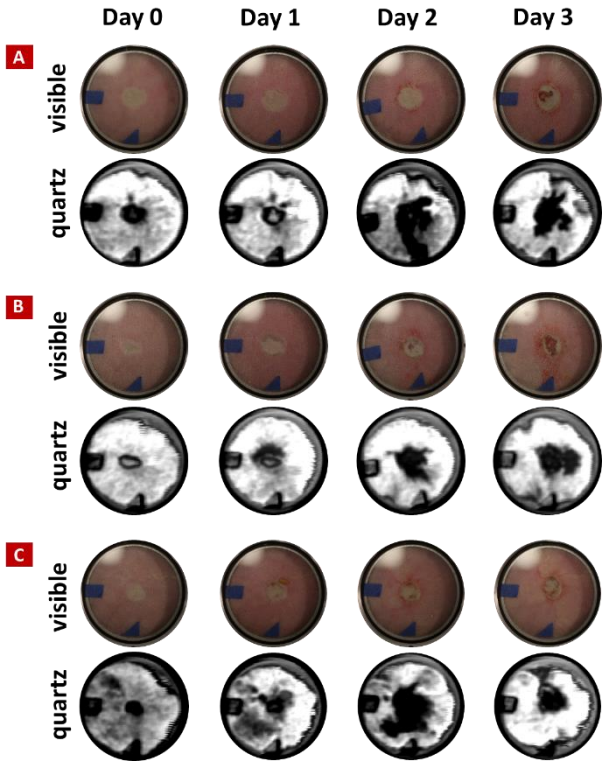

Figure 10-2: Longitudinal visible and THz imagery using a quartz window of a partial thickness burn induced with a ½'' diameter circular brand and a (a) 5 second, (b) 7 second, and (c) 10 second contact time.

As shown in **Figure 10-2**, marked differences in pixel intensities and distributions are observed for THz images of identical deep partial wounds created with varying contact times at different time points (Day 0, Day 1, Day 2, and Day 3). THz image sets are displayed in a standard

false color map where black-gray-white denotes increased reflectivity. Most discernible in the wound induced with a 7 second contact time (**Figure 10-2(b)**) at Day 0, the burn contact area is characterized by a ring of dark pixels encompassing a central region of high intensity pixels. The contributing factors to this difference in contrast, again, could potentially be edematous responses, widely known to accompany cutaneous injury, or conceivably electromagnetic interactions between quartz and tissue. As the days progress, the central area of dark pixels continues to grow. Image contrast, at this point, takes on a greater complexity; changes in anatomical features, including scab formation and regrowth of adjacent hair follicles, may be confounding THz signal. To further analyze image contrast between uninjured and burn contact areas, segmentation profiles were taken through the center of the burn across the field of view (FOV) at each day for all burn contact times (**Figure 10-3**).

The results of the spatial profile cuts are similarly interesting and unique for each burn series. The central burn area is characterized by low reflectivity for all time points in wounds of varying burn contact time. However, the extent of this decrease in signal intensity and its distribution (the spatial length it spans) are distinctly different for each deep partial burn. As originally predicted, there appears to be a many-to-one relationship between changes in image contrast observed with THz imaging and the severity of the burn as ascertained by histology. Without denying the significance and relevance of histology to burn depth assessment, this approach fails to furnish quantitative measurements of other diagnostic targets, including the presence, extent, and regional distribution of edema in injured tissue. Though edema remains to be confirmed as a primary cause of the changes observed in THz contrast of wounds, this preliminary work suggests that differences in contrast exist in imagery of wounds of similar burn severity. And, possibly, more information remains to be gleaned from these THz maps than is available in corresponding histology. The biological meaning and statistical significance of these changes in THz contrast, however, remain to be investigated in future, large-scale studies.

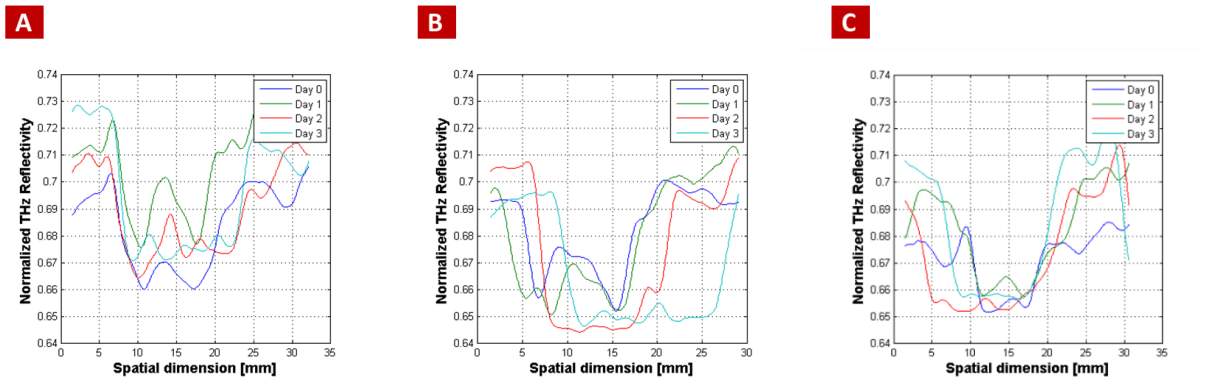

Figure 10-3: Spatial profile cuts of normalized THz signal across partial thickness burns induced with a circular brand for (a) 5 sec, (b) 7 sec, and (c) 10 sec under a quartz window.

10.4 CONCLUSIONS

The goal of tissue edema based burn wound severity assessment is instrumentation that is sensitive to features in edema that correspond directly to the depth of injury and/or the viability of the injured tissue while remaining insensitive to factors not salient to these features. For the first time, *in vivo,* this preliminary study investigates the effects of burn induction parameters, specifically burn contact time, on THz image contrast for burns of similar burn severity. THz imagery of deep partial burns induced with 5, 7, and 10 sec contact times are intrinsically different, and suggest that there may be a many-to-one mapping between information contained in THz contrast and burn depth assessment as ascertained by histology. Future exploration of this relationship will likely require a large data set and feature identification and testing that may require more sophisticated techniques such as belief networks and vector support machines.

CHAPTER 11: NON-INVASIVE THz IMAGING OF TWC FOR FLAP VIABILITY ASSESSMENT

11.1 SIGNIFICANCE

Large soft tissue defects resultant from oncologic surgery require tissue flap reconstruction to mitigate postoperative morbidity and mortality. Perfusion is often used to predict the viability of these flaps. Because TWC is a significant confounder to early perfusion-based assessments, this work set out to use reflective THz imaging, a non-invasive TWC sensing method, to evaluate the viability of myocutaneous dorsal flaps in an *in vivo* rat model. Reflective THz imaging detects variation in TWC between a histologically confirmed flap failure model and flap survival model 24 hr prior to clinical inspection alone. This ability to rapidly and non-invasively assess flap viability by monitoring changes in TWC may enable earlier and more successful intervention in reconstructive surgery.

11.2 MOTIVATION

In cases of vascular occlusion (i.e. thrombosis), flap outcome directly correlates with the rapid restoration of the vessels' patency; if reduced viability can be identified before 6 hr of thrombosis onset, that typically occurs within 72 hr following surgery, 60 - 73% of compromised flaps may be salvaged [108], [109].

Herein, THz imaging of myocutaneous flaps in a pre-clinical rat model was performed to explore the utility of THz-TWC based maps for early flap viability assessment. Six myocutaneous flaps of either high tissue viability (n=3) or low tissue viability (n=3) were surgically created in the dorsal skin of rats and a previously reported reflective THz imaging system was used to track the distribution of TWC across the flap margin over a period of 7 days (**Figure 11-1(a)-(b)**) [6], [9], [15]. This time window was selected based on morphological changes observed in the field of view (FOV) and motivated by the evolution of the wound healing response following cutaneous injury

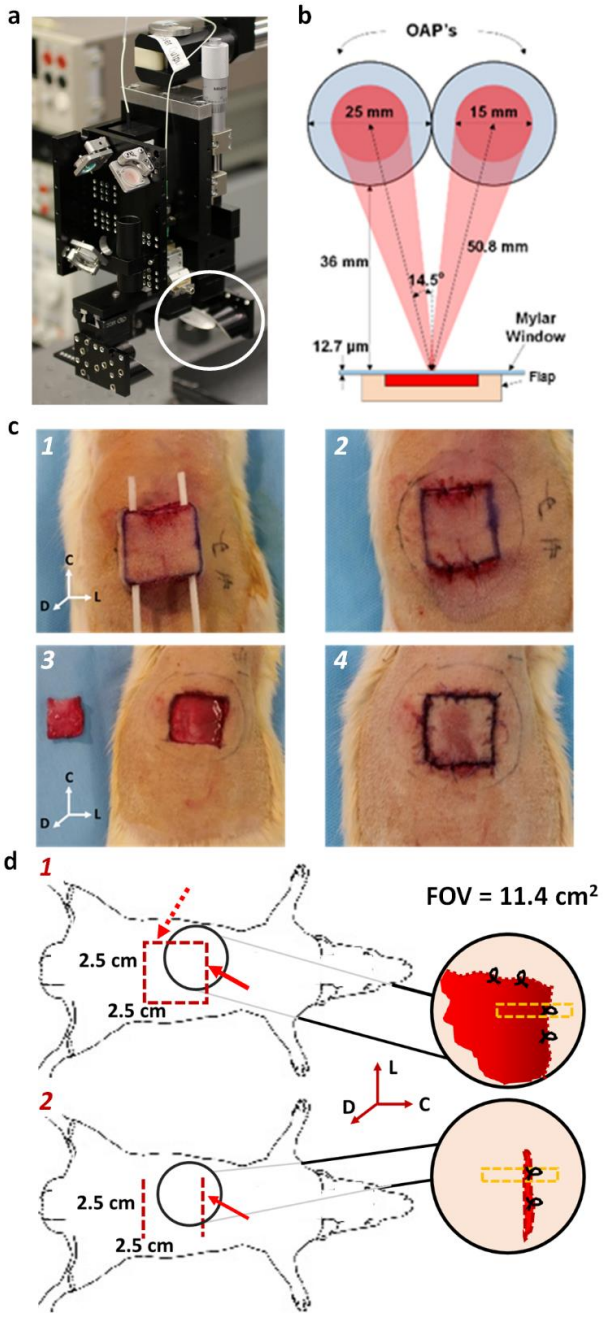

Figure 11-1: (A) Visible image of the reflective THz system. Dorsal flaps of anesthetized rats are raster scanned on x- and y-stepper motors beneath the imager. The encirlcled optics correspond to (B) off-axis parabolic mirrors used to focus the THz beam onto a thin-film Mylar window that serves to mitigate surface contours of the underlying flap. (C) Myocutaneous flap design of (a) an axially-based bipedicled flap (i.e. survival model), measuring 2.5 x 2.5 cm^2 in area with cephalic and caudal incisions, that is elevated deep to the panniculus carnosous and then (b) surgically secured in its anatomical position. (c) Completely excised myocutaneous skin flap (i.e. failure model), measuring 2.5 x 2.5 cm^2 in area with circumferential flap excision, that is elevated deep to the panniculus carnosous and (d) sutured back in anatomic position. "L," "D," and "C" correspond to lateral, dorsal, and cephalic anatomical directions of the rat. (D) Histological evaluation of tissue viability for (a) an excised flap and (b) a bipedicled flap in a rat. Sagittal histological slices of 5 µm thickness were taken from 2 cm x 2 mm tissue sections (dotted yellow rectangle) harvested from the cephalic incision site (solid red arrow) on day 7. A suture in each slice (black loop) served as an intradermal fiducial marker for image registration of histology to the same region in the field of view (FOV) captured by THz-time series imagery.

[107]. Rats were selected as our pre-clinical model given thicknesses of rat and human skin layers are most similar compared to those of other animal models (i.e. pig, mouse, and hairless mouse) [147]. A survey of the literature also shows the rat model has proven useful for studying changes in skin subsequent to surgical elevation of a dorsal skin flap [54]. A 2.5 x 2.5 cm^2 excised myocutaneous flap and a 2.5 x 2.5 cm^2 bipedicled myocutaneous flap were selected as a failure and survival model, respectively (**Figure 11-1(c)**) [197]. We hypothesized that a flap model of lower tissue viability would present lower TWC contrast, and therefore its THz map would display reduced THz reflectivity with respect to that of uninjured skin. Reflective THz measurements of skin were compared to temporally and spatially matched histology (**Figure 11-1(d)**) and clinical assessments.

11.3 MATERIALS & METHODS

11.3.1 Skin Flap Surgery

All experiments were approved by the Institutional Animal Care and Use Committee (IACUC). Six 14 week old male Lewis rats (Charles River Laboratories, Wilmington, MA) weighing 250 - 300 g were used as pre-clinical models to investigate effects of varying flap tissue viability on TWC maps acquired with reflective THz imaging. Here, myocutaneous dorsal flaps of either low or high tissue viability were compared (**Figure 11-1(c)**).

All rats were maintained in temperature-regulated environments (24 ^oC) on a 12-hr light/dark cycle and housed one pair per cage with soft bedding and a microinsolator cover. Animals underwent general anesthesia with inhaled isoflurane and were placed on a water heating pad for temperature regulation at 37±0.5°C. Each rat was shaved from scapula to pelvis to expose a 6 x 6 cm^2 area of dorsal skin. Rats were placed in prone position under the THz imaging system, a 12.7 μm dielectric Mylar window was lowered onto the shaved dorsal skin to

flatten the imaging field, and pre-evaluation visible and THz images were captured with a SLR camera and the THz imager, respectively. The scanned area of the dorsum was marked with a black marker, and the anesthetized rat was then returned to the surgical field.

The rats were then aseptically prepared with three alternating scrubs of betadine and isopropanol and randomly assigned to receive either a 2.5 x 2.5 cm^2 excisional myocutaneous flap (n=3) or a bipedicled myocutaneous flap (n=3).

The axially based bipedicled mycocutaneous flap was designed as the control for flap survival since all axially based vasculature and the dermal plexus to the flap remained intact through the bipedicled flaps (**Figure 11-1c(1**)). Using a #15 blade, an incision was made at the cephalic and caudal borders of the designed flap through the panniculus carnosus. The flap was elevated deep to the panniculus carnosous muscular layer to the lateral borders of the designed flap. Simple interrupted 5-0 polypropylene sutures were used to close the incision in anatomic position (**Figure 11-1c(2)).**

The excisional myocutaneous flap was designed as an experimental flap failure since all vasculature was completely ligated when the flap was excised (**Figure 11-1c(3**)). Using a #15 blade, an incision was made along all borders of the designed flap though the panniculus carnosuos. The flap was elevated deep to the panniculus carnosous muscular layer and the myocutaneous flap was completely excised. The flap was allowed to remain extracorporeal for 20 minutes. Again, simple interrupted 5-0 polypropylene sutures were used to close the incision in anatomic position (**Figure 11-1c(4)).** Rats were then allowed to recover from anesthesia and transferred to the vivarium for post-operative monitoring. Post-operatively, all animals received analgesia with subcutaneous injections of carprofen (5 mg/kg) daily for 72 hr.

THz and visible imagery were continuously acquired for one hour after surgery, followed by a single 24 hr, 48 hr, and 7-day post-operative scan. At each time point, the dielectric Mylar window was lowered onto the flap during THz imaging. After a 7-day postoperative observation period, the rats were euthanized and histological specimens harvested.

11.3.2 Clinical Examination

Postoperative monitoring of flap compromise was performed by two head and neck physicians by visual inspection and palpation. Flaps were evaluated on a daily basis for the first 3 days and then finally on day 7 for clinical signs of ischemia and variation in tissue elasticity [54], [105]. On postoperative day 7, the total amount of skin flap necrosis was observed and recorded for each rat.

11.3.3 Histology

A blind histological analysis of flap tissue harvested at 7 days post operation was compared to visible and THz imagery to determine tissue viability in tissue flaps. A 2 x 2 cm^2 region was harvested from the cephalic and caudal incision sites of each flap, transferred to 10% formalin solution, and submitted for routine processing for histopathological evaluation (**Figure 11-1(d)).** All tissue samples were histologically sectioned saggital to the major axis of the sample and contained an intradermal suture for orientation and registration of the tissue specimen. Three histological slices of 5µm thickness were acquired from each tissue block, stained with hematoxylin and eosin, and analyzed to determine tissue necrosis. Histologic sections included the original flap as well as a myocutaneous margin or non-traumatized tissue to provide a control area for histologic comparison. Assessment of viability was based on the morphology of the individual cells and patency of vessels [198].

11.3.4 Statistical Analysis

An independent Student *t*-test was used to compare reflectivity differences between pre-surgery and 24hr THz profiles for excised flaps and bipedicled flaps. Equal variances were assumed for both flap models and the level of significance was set at $p < 0.05$.

11.4 RESULTS

11.4.1 *In Vivo* THz Flap Imaging

In vivo THz time-series imagery of three excised flaps **(Figure 11-2(a))** and three bipedicled flaps (**Figure 11-2(b)**) in the dorsal skin of anesthetized rats was acquired over a 7-day period. Skin flaps were imaged under a thin (12 μm) film Mylar window to eliminate confounding effects from non-uniform surface topography, and visible and parallel THz images were generated. Because the dimension of the flaps exceeded that of the dielectric window, only the cephalic incision and flap tissue were captured in THz and visible images. The flap tissue and

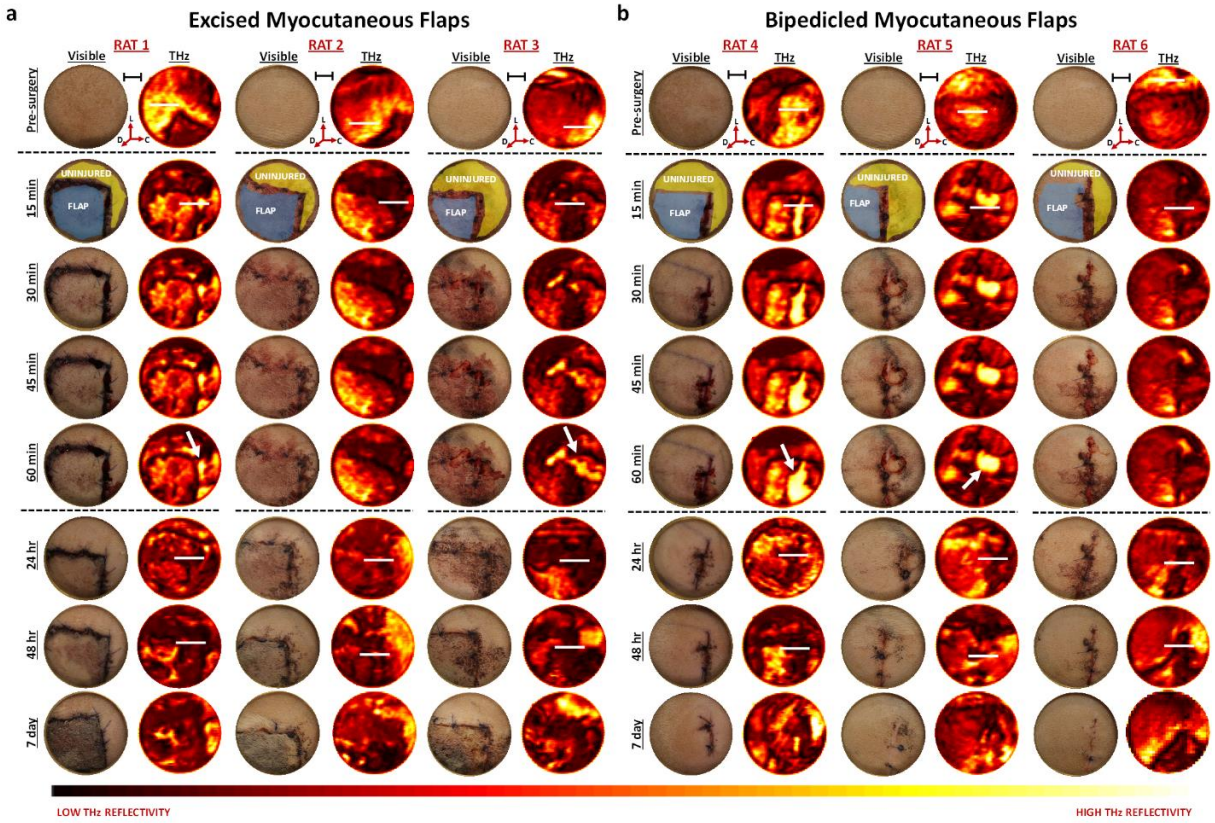

Figure 11-2: (A) Excised flaps and (B) bipedicled flaps in the dorsum of anesthetized rats were imaged under a 12.7 μm Mylar window over a 7-day period. Uninjured tissue and flap tissue are labeled in yellow and gray fields, respectively, in visible images acquired at 15min following surgery. The hot color map of THz imagery transforms black to the global minimum THz reflectivity and white to the global maximum THz reflectivity. "L," "D," and "C" in the 3D axis denote directions detailed in Fig. 1. Black scale bars represent ~1 cm in the FOV. ~1.5 cm long contours, indicated by solid white horizontal lines, segment the cephalic incision, flap region, and non-traumatized tissue. Solid white arrows locate the accumulation of blood, indicated by high THz reflectivity, at the incision site.

non-injured area are denoted by grey and yellow fields in visible images at 15min post-surgery, respectively. The “hot” color map associated with THz imagery transforms black to the global minimum THz reflectivity and white to the global maximum THz reflectivity.

During the first 48 hr following surgery, THz reflectivity profiles were generated for 1.5 cm long contours (indicated by white horizontal line segments in THz imagery in **Figure 11-2)** that captured the same region of the cephalic flap margin. Clinical acute assessments of flap viability are typically performed for 48 hours post-operatively, and therefore we used this as our acute endpoint for the THz image analysis [109]. First, THz reflectivity values of these contours were normalized to the maximum THz reflectivity acquired from an aluminum calibration target (i.e. ideal reflector) and zero THz reflectivity measured in the absence of a reflecting target (i.e. air). Next, the percent change (% Δ) in THz reflectivity between profiles before surgery and those following flap surgery at 15min, 24hr, and 48hr were generated (**Figure 11-3**). Lengths of the THz profile to the left and right of the cephalic incision site, that is denoted by a dotted vertical line, correspond to the flap region and surrounding non-traumatized tissue, respectively.

THz images of the rat dorsums prior to flap surgery (**Figure 11-2(a)-(b)**) displayed mostly uniform reflectivity across the FOV. Low reflecting areas, such as those evident in the periphery of many flaps, may have resulted from reduced contact coupling between the Mylar window and underlying skin.

Immediately following surgery, THz images for all flaps identified the spatial location of the surgical incisons. Black lines (i.e. narrow, low THz reflectivity areas bordering regions of high THz reflectivity in **Figure 11-2(a)**) evident in THz images for all excised flaps at 15min – 1hr spatially mapped to circumferential incision sites. Because a bipedicled flap does not include lateral incisions, black lines apparent in THz imagery of this tissue region **(Figure 11-2(b)**) were likely due to either intrinsic surface contours within the rat dorsum or dissection borders deep to the

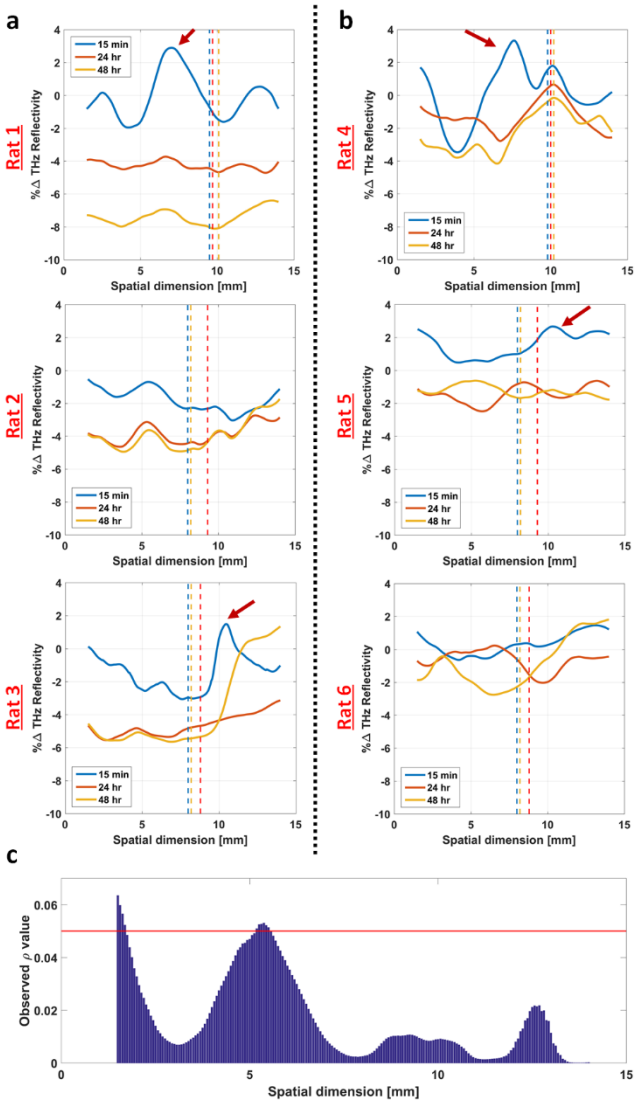

Figure 11-3: (A) Profiles of %Δ THz reflectivity in excised flaps and (B) bipedicled flaps with respect to pre-surgery values were generated for white contours that segment THz images in Fig. 2. These THz profiles captured the cephalic incision (i.e. dashed vertical lines), flap region (i.e. left of incision), and non-traumatized tissue (i.e. right of incision) of tissue flaps at 15min, 24hr, and 48hr post-operation. All red arrows denote increased THz reflectivity due to the presence of blood immediately following surgery, a confounder to THz contrast. (C) Differences in THz reflectivity between the control and 24hr profile for both flap models were confirmed to be statistically significant ($p < 0.05$) across the cephalic flap margin using an independent *t*-test.

panniculus layer rather than gross features from the bipedicled flap. For rat 1, rat 3, rat 4, and rat 5, the leakage of blood (denoted by solid white arrows) from the incision sites further delineated their respective flap margins; blood, like TWC, is a highly reflective, dispersive polar medium, and therefore a confounder to THz TWC contrast. The accumulation of blood along the flap margin

appears as increased THz reflectivity in all post-op images acquired between 15min and 60min (**Figure 11-2).** Because THz flap imagery acquired 15min postoperatively was least confounded by blood, THz reflectivity at this time point was analyzed for Day 0. THz reflectivity profiles for the aforementioned rats at the 15min mark (**Figure 11-3)** illustrate these irregularities, or "hot spots," along the length of the cephalic incision as clearly defined peaks denoted by solid red arrows. With the exception of these peaks and 'troughs,' likely due to uncoupling between the window and skin, %Δ THz reflectivity between pre-surgery and 15min post-surgery across the flap for most rats is close to 0%.

Twenty-four hours postoperatively, the contrast of THz images and their accompanying reflectivity profiles became markedly distinct between both flap models. Visible inspection alone of the THz excised flap imagery (**Figure 11-2(a)**) suggested reduced THz reflectivity in the form of 'dark zones' at the cephalic and lateral incision site as well as the peripheral segment of the flap. Though reflectivity of the cephalic incision was similarly low in THz imagery of bipedicled flaps, likely due to then dried blood, the surrounding tissue contrast was mostly unperturbed. This result was further substantiated by %Δ THz reflectivity calculated between pre-surgery and post-surgery THz profiles for both flap models at 24hr (**Figure 11-3(a)-(b)**). A noticeable decline (4% - 5.5 %Δ) in THz reflectivity was apparent in excised flaps which continued to persist by 48hr ensuing surgery. However, as expected, %Δ THz reflectivity of non-traumatized tissue adjacent to the excised flaps approached baseline values (0%). By comparison, most %Δ THz reflectivity for both the flap region and adjacent non-traumatized tissue in bipedicled flaps either remained within the same reflectivity neighborhood or approached that at pre-surgery (0 %). Irregularities in THz contrast, such as reduced %Δ THz reflectivity in the form of troughs at 48hr for rat 4 and rat 6, were likely explained by suboptimal coupling of tissue flaps with the dielectric window, irregular incision geometries, as well as differences in perfusion due to non-uniform flap surgery. Because 24hr post-surgery is clinically more important for flap assessment, an independent Student *t*-test of reflectivity differences between the pre-surgery and 24hr THz profiles was

performed at this time point. This yielded statistical significance ($p < 0.05$) across the cephalic incision for excised flaps and biedicled flaps at 24hr postoperatively (**Figure 11-3(c)**).

11.4.2 Gross Observations

Surviving surface areas in each flap viability model were markedly different (**Figure 11-4**). Clinical evaluation of bipedicled flap tissue revealed no signs of ischemia (i.e. cyanosis) and

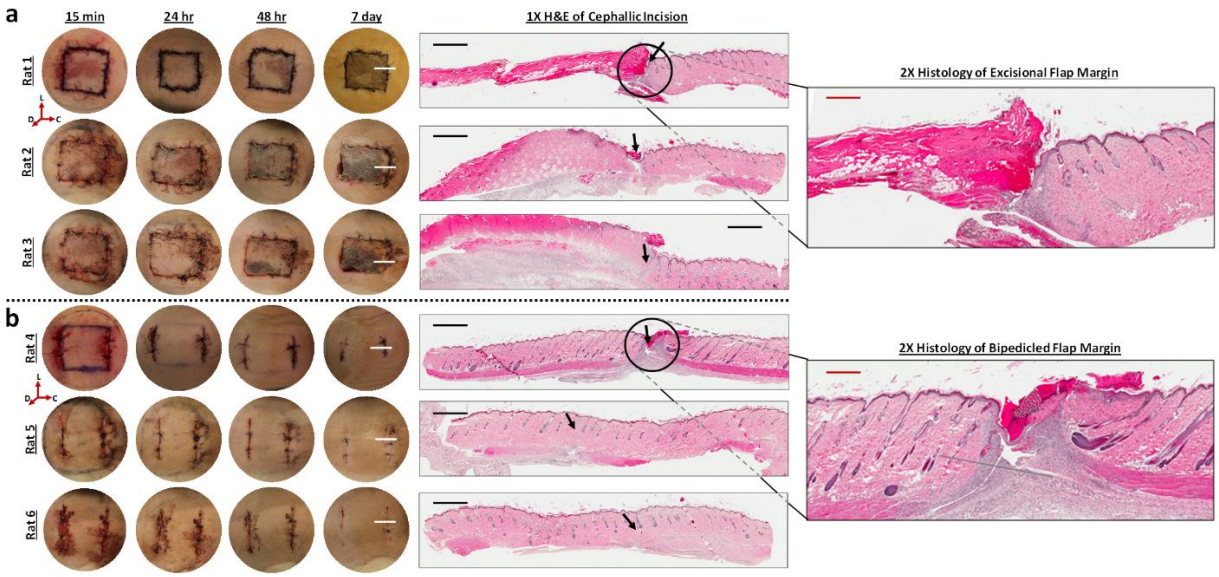

Figure 11-4: Post-operative visual surveillance and histological assessment of (A) excised flaps and (B) bipedicled flaps over 7 days. "L," "D," and "C" correspond to directions in Fig. 1. 1X and 2X representative hematoxylin and eosin (H&E) staining for tissue flap margins spatially map to the cephalic incision at day 7, demarcated by white horizontal lines in the visible imagery. In the H&E image, flap tissue and non-traumatized tissue lie to the left and right of the incision site (denoted by a black arrow), respectively. Necrotic tissue appears dark magenta in the H&E stain. The black scale bar and red scale bar represent ~1 mm and ~450 μm, respectively.

minimal change in skin pliability, all indicative of a surviving flap. Contraction of the cephalic and caudal incisions by Day7 suggested optimal wound healing likely due to neovascularization and metabolic support from the lateral pedicles. The survival area was estimated to be 100% by two independent observers (JKA and RJ). Conversely, the excised flaps displayed progressive necrosis over 7 days. At 24hr, the flaps appeared grossly absent of congestion or cyanosis, with no clear demarcation being evident between viable and nonviable tissue. By 48hr, tissue contraction and cyanosis began to appear near the peripheral segments and on examination

accounted for 30%, 40%, and 25% of the flap area in rat 1, rat 2, and rat 3, respectively. This necrosis continued, and by Day7, a well-defined demarcation line between viable and nonviable tissue was evident. The surviving surface area of the myofascial flap was estimated to be ~0%, 10%, and 20% for rat 1, rat 2, and rat 3, respectively.

11.4.3 Histological Assessment

Histological evaluation of tissue sections from both flap models confirmed viability results that were evident grossly at 7 days following surgery (**Figure 11-4**). A blinded pathologist identified all histological sections from cephalic incisions of the excisional flaps as necrotic (**Figure 11-4(a)**). Severe, full thickness necrosis of the skin and underlying muscle layers as well as the loss of dermal papilla and sebaceous glands were captured by hypereosinophilia in hematoxylin and eosin (H&E) stained sections, delineating a clear demarcation between the compromised and non-traumatized viable tissue. Neovascularization and early collagen deposition were only apparent in the adjacent, non-injured tissue.

In contrast, caudal and cephalic segments of bipedicled flaps were all completely viable (~0% necrosis) on histological evaluation (**Figure 11-4(b)**). Both non-injured and flap segments were characterized by intact skin and muscle layers, subcutaneous follicles, and glands. While absent in the samples of the excised flaps, early signs of wound healing, specifically granulation tissue and chronic inflammation, were apparent at the incision margin (denoted by black arrow).

11.5 DISCUSSION & CONCLUSIONS

Since water constitutes ~70% of the skin weight and the THz frequency dielectric constant of water is significantly higher than that of non-water constituents, increases in THz reflectivity are assumed to be approximately positively correlated to increases in TWC of tissue, such as a flap [6], [49], [168], [199]. In this way, variation in TWC of dorsal tissue flaps can be monitored non-

invasively with reflective THz imaging as a function of time and location to determine tissue viability. It is important to note that THz imaging furnishes a 2D refection image of TWC *contrast* rather than an *absolute* measurement of TWC. Because THz-based visualization of *variation* in TWC is both early and accurate, this technique is more clinically attractive than more costly, difficult, and lengthy estimations of *absolute* TWC. For instance, magnetic resonance imaging is one of the few techniques used to determine the fraction of protons available in tissue, however, its cost and limited portability make it inappropriate for TWC characterization in patients, especially critical patients.

As originally hypothesized, *in vivo* THz imaging measurements indicate that TWC of an excised flap and bipedicled flap model, determined to have low and high tissue viability, respectively, is markedly different. Moreover, variation in TWC between both flap models is evident as early as 24 hr post-operatively. Following surgical elevation of excised flaps, THz TWC contrast at the cephalic incision site is significantly lower than that of the pre-elevation value. TWC contrast observed in THz imagery at this site continues to progressively decline for the remainder of the 7-day observation period.

Spatiotemporal variations in TWC contrast in THz imagery of the excisional flap model are consistent with both clinical and histological assessments of flap viability. There are few visual signs of desiccation or abnormalities (i.e. edema) observed within excised flap tissue 24 hr after the surgical procedure has been completed (**Figure 11-4(a)**). Difficulty in visual assessment of edema arises because fluid build-up, that is perceived clinically as an increase in tissue volume, is only visually apparent after tissue volume has doubled [54]. At this same time point, however, the TWC THz map has clearly identified those regions of tissue that were insufficiently hydrated. Since adequate perfusion of the dermal plexus is essential to sustain the functional and structural viability of the skin, it is expected that severely dehydrated tissues will gradually proceed to ischemia, and finally necrosis [200]. This progression is grossly observed 48 hr after surgery as well as confirmed histologically on Day 7 (**Figure 11-4(a)**); skin flaps rely on the underlying

vascularity of the bed for adequate TWC and nutrients, and therefore wounds that are poorly vascularized, as in the case of an excised injury, will not support the flap [201].

Conversely, THz TWC contrast across a bipedicled flap remains similar to that at pre-surgery (**Figure 11-3(b)**). This TWC result is likely due to survival mechanisms characteristic to flaps containing pedicles, or an intact blood supply:

> Plasmatic imbibition — Initially, skin flaps passively absorb nutrients in the wound bed by diffusion. Both the bipedicled flap and excised flap received rudimentary nutrition in this manner. However, in the excised flap this mechanism was the sole source of tissue nutrients, while the bipedicled flap retained its dermal plexus for tissue perfusion. It is likely that the nutritional demand of the excised flap proved to be in excess of the nutritional supply by plasmatic imbibition resulting in subsequent tissue ischemia and necrosis, and therefore reduced TWC, by 24 hours (**Figure 11-3**) **[202]–[204]**.
>
> Inosculation — By day 2 to 3, the cut ends of the vessels on the underside of the flap dermis begin to form connections with those of the wound bed. This likely explains the observed rise in THz reflectivity, or TWC, towards baseline for bipedicled flaps at 48 hr (**Figure 11-3(b)**). After this point, new blood vessels grow (i.e. angiogenesis) into the flap and the tissue becomes fully vascularized **[202]**.

Clinical and histological evaluation of tissue viability of the bipedicled flaps support this finding. Collectively, THz visualization of differences in flap TWC enables detection of flap status 24 hr prior to clinical assessment and reported imaging methods (i.e. laser Doppler imaging), and, thus, may afford important implications in a number of areas of our research, including edema monitoring in wounds and skin evaluation [6], [15]. Specifically, in clinical cases when a pre-evaluation THz scan of TWC is typically unavailable, early detection of TWC changes with respect

to the neighboring uninjured tissue could enable expedited surgical re-exploration and potential salvage of failing tissue flaps prior to irreversible ischemia.

There are several key experimental points that warrant additional investigation. From a clinical vantage point, the use of windows for THz flap assessment is factor that affects the accuracy of THz measurement and is a practical barrier to non-contact, *in vivo* medical translation of this technology. Concerns include physical perturbation of the wound and pressure exertion that may change TWC image contrast. Although windowless flap assessment is ideal, low-loss dielectric windows are necessary in THz imaging to minimize confounding effects from non-planar geometries and respiratory motion *in vivo*. Both high and low dielectric substrates, including quartz, sapphire, and thin stretched Mylar, are commonly used to flatten the imaging target. During our THz flap imaging study, we employed a thin Mylar window and observed that flexibility of the film may not have sufficiently eliminated confounding contributions from irregular surface features. In future studies, we plan to test the repeatability and accuracy of THz imaging using 500 µm quartz, a more rigid substrate.

Next, flap dimensions and how this may potentially change THz TWC contrast must be explored; the surface area to nutrient ratio of larger excised flaps is greater, which may lead to earlier necrosis. Because tissue flaps also vary in thickness, depending on where the flap is located on the body, electromagnetic modeling may offer more insight into how THz TWC contrast varies as a function of skin thickness. Additionally, significant TWC findings observed in this preliminary study lay the groundwork for future serial studies in which biopsies can be performed at 24hr and 48hr to investigate the predictive power of THz imaging for flap viability assessment. Inclusion of these experimental design parameters, coupled with existing rapid and noninvasive THz imaging, may lend reflective THz sensing as a powerful augmentation to the standard clinical assessment of tissue.

CHAPTER 12: CONCLUSIONS AND FUTURE WORK

The work I have done to further develop, characterize, and pre-clinically test the UCLA reflective terahertz (THz) imaging system represents a significant advancement in both the scientific understanding of the technology itself and its clinical implications for wound edema assessment. This chapter offers a synthesis of the work completed, its clinical significance, and my vision for the continued development and application of reflective THz imaging as an augmentation to the standard clinical assessment of cutaneous wounds.

12.1 Summary of Completed Work

Our THz group pioneered *in vivo* application of THz radiation for wound assessment and was the first to acquire and publish an *in vivo* image of a skin burn. My engineering and scientific work in reflective THz imaging stemmed from an incomplete understanding of THz image contrast in these preliminary *in vivo* THz burn wound imaging studies (**CHAPTER 4**). Native, pathology-specific contrast observed in THz maps of superficial tissue is widely hypothesized to be due to variations in tissue water content (TWC). However, observed spatio-temporal differences in THz reflectivity between burn wounds of varying severity, although the first-of-their-kind, deviated from fluid shifts that are clinically known to characterize burn edema pathogenesis. There is no question that THz radiation is sensitive to tissue water content (TWC). However, the contribution of this factor to THz imaging contrast and how it relates to tissue pathology still remain to be verified. Once investigated and confirmed, THz visualization of differences in TWC has important clinical implications in not only edema monitoring of wounds but also skin evaluation.

Given my group's prescriptive vision for *in vivo* use of THz imaging, my first aim was to characterize the hydration sensitivity of our reflective THz imaging system – a task that had yet to be performed- in tissue-mimicking gelatin phantoms (**CHAPTER 5**). Differences in the calculated hydration sensitivities for varying gelatin phantom experiments reinforced the challenges in establishing a robust standard for THz hydration calibration that effectively accounts

for variations in system performance. Due to changes in THz reflectivities of a constant hydration phantom across –x and –y directions as well as drift in system bias, a single relation between THz reflectivity and phantom hydration content was deemed insufficient. Instead, multiple hydration sensitivity curves of gelatin phantoms under different mount configurations were generated to 1) account for temporal and spatial system differences between and during image acquisition periods; 2) and enable quantitative comparisons within and between varying THz hydration sensing data sets. Irrespective of the gel configuration, a positive linear trend was observed between increases in hydration and corresponding THz reflectivities within a hydration range of 83% - 95%. Statistically significant hydration sensitivities between 0.0209 – 0.0389% were calculated across multiple hydration phantom configurations. Electromagnetic modeling of the three-layer system (Air-Window-Phantom) using the Transfer Matrix Method indicated that reflectivity vs. water content in the region of 81% - 97% hydration is linear, with a R^2 value of 1. These simulation results agreed with and validated the linear trends observed in the experimental results.

Having verified the high hydration sensitivity of the UCLA THz imaging system, I then assessed the feasibility of using 7 Tesla (7T) magnetic resonance imaging (MRI) as a companion modality to investigate TWC-based contrast mechanisms in THz imaging (**CHAPTER 6**). Because quantitative assessments in skin using images obtained with standard MRI sequences are limited, with no reports on MRI of burns, I first explored MRI in an *ex vivo* burn model, specifically porcine skin. This step was both crucial and necessary to identify and optimize the appropriate MRI imaging sequence parameters for future *in vivo* THz-MRI correlative assessments of THz imaging contrast. Working closely with our collaborators at the ALBMC Brain Mapping Center, I verified the sensitivity and specificity of T_2 relaxation times and relative proton densities in T_2w MSME MRI imaging of *ex vivo* porcine burns. Both multiparametric MRI measures describe mobile TWC and increase with increasing burn wound temperature. This study was the first-of-its-kind and laid the groundwork for all subsequent *in vivo,* parallel THz-MRI

burn imaging studies.

Unlike a cutaneous injury in an *ex vivo* model, trauma induced in an *in vivo* system results in an immediate, rapid accumulation of fluid in tissue, clinically termed edema. Quantifying and visualizing edema, however, remains a clinical challenge. By performing the first *in vivo* correlative assessment of mobile TWC in THz imaging with companion T_2w MRI, I demonstrated that it is possible to non-invasively and rapidly detect fluid shifts in burn-induced edema models using reflective THz imaging (**CHAPTER 7**). For *in vivo* burn wounds of varying severity in pre-clinical rat models, the time course and magnitude of THz reflectivity associated with the burn region reflected known trends observed in edema pathogenesis and strongly correlated with companion hydration measurements acquired at specific burn depths by magnetic resonance imaging (MRI). Strong positive correlations were evident at greater depths in the dermal tissue: at 688 μm, temporal coefficients (*p)* computed with normalized cross-correlation were as high as 0.97 and 0.86 for a full thickness and a partial thickness burn, respectively. This work offers the first *in vivo* correlative assessment of mobile TWC as a major contributor to THz imaging contrast and reports depths at which THz imaging can probe edema following cutaneous injury. From a technological standpoint, the TWC shifts that we observed with THz and MR imaging are the first to be imaged *in vivo* for both modalities. For the sake of completeness and to confirm that all observed changes in image contrast were due solely to burn edema pathophysiology and not any system-related artifacts from transferring the animal between both modalities, I performed continuous, *in vivo* MRI of a partial thickness and full thickness burn (**CHAPER 8**). Following the previous MRI imaging protocol, I observed the formation of edema in both wound models. T_2w MRI of a partial thickness wound demonstrated greater edema as was similarly evident in the concomitant THz-MRI burn imaging study.

With a firmer understanding of TWC-based contrast mechanisms in THz imaging and how they specifically relate to tissue pathology, I revisited *in vivo* THz burn imaging to build upon our earlier work (**CHAPTER 9**). Our group has previously reported on the use of reflective THz

imaging to non-invasively detect and longitudinally monitor changes in TWC in burns of varying severity *in vivo*. These first-of-their-kind THz-based TWC results, however, differed from known pathological fluid shifts secondary to thermal injury. To acquire unique and reproducible THz-TWC maps of burns and better interpret these results in the context of burn edema pathophysiology, I performed advancements in THz imaging and the experimental methodology. These included: 1) an image registration method to reliably compare longitudinal THz-TWC measurements with histological wound evaluation; 2) a reproducible contact-burn induction technique; and 3) the exchange of multiple dielectric windows during imaging using a simple, robust optical mount to explore the effects of refractive index on THz burn image contrast. A reflective THz imaging system operating at 0.525 THz was used to acquire longitudinal *in vivo* imagery of histologically verified partial thickness or full thickness burns of uniform severity in the abdominal skin of rats. Wounds were imaged periodically over the course of 7hrs under a quartz (500 µm) and Mylar (12 µm) window, followed by a single 24hr, 48hr, and 72hr post burn scan. For THz imaging of burn wound models using either a quartz or Mylar window, reflectivity changes across the burn region electromagnetically corresponded to TWC variation consistent with burn edema pathogenesis. Differences in THz contrast between the burn region and non-traumatized tissue for both wound models were further substantiated by image intensity histograms. Based on these preliminary findings, Mylar and quartz were identified as appropriate dielectric windows to distinguish partial thickness and full thickness wounds in the burn contact area and the peripheral uninjured tissue, respectively. These results collectively suggest that implementation of these experimental methodologies and the prospect of window-driven THz imaging both enable tracking of TWC to distinguish partial thickness and full thickness burn wounds and further our understanding of the sensitivity of windows to edema in specific regions of burn wound pathophysiology *in vivo*.

Finally, in parallel with my work testing the reflective THz imaging system for burn wound assessment, I also contributed to the first collaborative effort with Dr. St. John in the Department

of Head and Neck Surgery to assess the utility of THz imaging for early assessment of tissue flap viability (**CHAPTER 11**). Accurate and early prediction of tissue viability is the most significant determinant of tissue flap survival in reconstructive surgery. Perturbation in TWC is a generic component of the tissue response to such surgeries, and, therefore, was hypothesized to be an important diagnostic target for assessing the extent of flap viability *in vivo*. For this study, I obtained longitudinal visible and reflective THz imagery comparing 3 bipedicled flaps (i.e. survival model) and 3 fully excised flaps (i.e. failure model) in the dorsal skin of rats over a postoperative period of 7 days. While visual differences between both models manifested 48 hr after surgery, statistically significant ($p < 0.05$, independent *t*-test) local differences in TWC contrast were evident in THz flap image sets as early as 24 hr. Excised flaps, histologically confirmed as necrotic, demonstrated a significant, yet localized, reduction in TWC in the flap region compared to non-traumatized skin. In contrast, bipedicled flaps, histologically verified as viable, displayed mostly uniform, unperturbed TWC across the flap tissue. These first-of-their-kind results indicate the practical potential of THz TWC sensing to accurately predict flap failure 24 hours earlier than clinical examination.

12.2 Significance and Future Work

The collective body of engineering, research, and pre-clinical work that I have completed in support of this dissertation represents a significant contribution to reflective THz imaging technologies and their application to clinical wound assessment in three major regards:

First, I performed the first *in vivo* correlative assessments between THz imaging and T_2w MRI at specific tissue depths in burn wounds that 1) verify mobile TWC (i.e. edema) as the underlying biophysical driver behind observed changes in TH reflectivity; and 2) quantify, for the first time *in vivo*, tissue depths at which THz imaging can probe edema.

Second, I advanced *in vivo* THz burn imaging and confirmed its feasibility for early burn wound assessment. In addition to demonstrating unique contrast in THz burn maps confers

unprecedented conspicuity for burn wound severity within the first 7hr following injury, I have shown that spatio-temporal changes in reflectivity observed with the use of multiple dielectric windows agree with both expected electromagnetic behavior and clinically reported fluid shifts in burn edema pathophysiology.

Third, I performed the first pilot flap imaging study that successfully visualizes differences in TWC between surviving and failing flaps 24hr prior to clinical assessment and reported imaging methods (i.e. laser Doppler imaging). Based on my experience and findings, I posit the following work to maximize potential clinical translation of the reflective THz imaging technology:

1) **Develop a rapid, scanning THz burn imaging system** – Currently, the reflective THz image is generated by raster scanning the region of interest (i.e. the target) beneath a fixed, focused THz beam using x and y stepper motors. An image with a 6 cm x 6 cm FOV and 0.5 mm isotropic resolution can be acquired in ~10 min. Future efforts should facilitate the translation of this THz technology for clinical use through improvements in imaging speed and optical architectures that include system scanning by linear/angular translation of the optical components (**Figure 12-1**: (Left) 3 dB, 10 dB, and 20 dB widths of all THz images. (Right) CAD of scanning THz system.). An analysis of the 2D spatial frequencies of the THz images suggests that imagery acquired with the current system (2'' OAP objective mirrors) is actually oversampled by a factor of 4 (**Figure 12-1**: (Left) 3 dB, 10 dB, and 20 dB widths of all THz images. (Right) CAD of scanning THz system.). Therefore, the constraints on the current spatial resolution (1 mm) can be relaxed if needed, and subsequently the scanning time can be sufficiently decreased by collecting less data. This can be achieved using a larger step size (1 mm) for the translation stage motors and off-axis parabolic mirrors with longer effective focal lengths. Importantly, the long acquisition times of current edema assessment techniques, including CT and MRI, required to obtain an image render them unsuitable for detecting or monitoring acute,

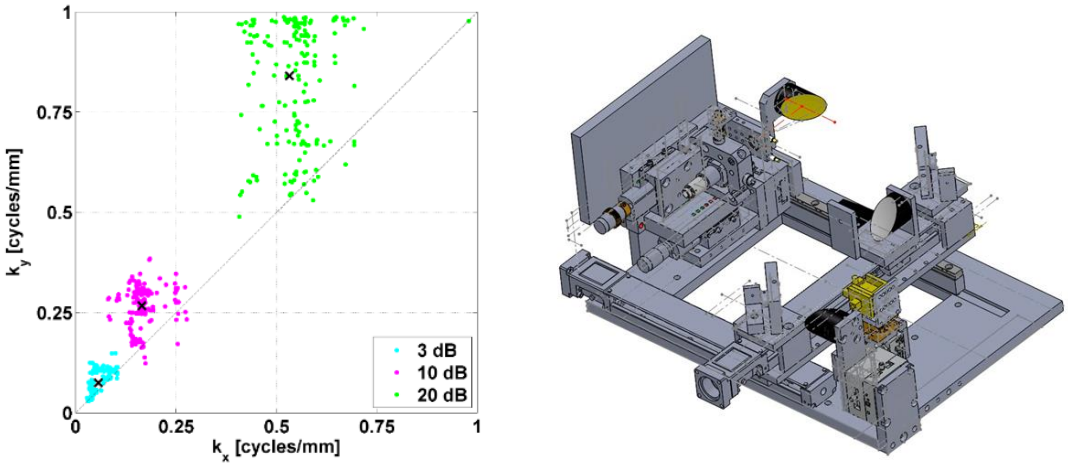

Figure 12-1: (Left) 3 dB, 10 dB, and 20 dB widths of all THz images. (Right) CAD of scanning THz system.

incremental information associated with symptom onset. Although THz imaging is comparatively much faster, reducing the scanning time further offers even more rapid THz image acquisition times (estimated to be ~ <2 min) to enable early detection and longitudinal monitoring of edema processes.

2) **Perform electromagnetic modeling of window-driven THz imaging-** From a clinical vantage point, the use of windows for THz burn wound assessment is a practical barrier to non-contact, *in vivo* medical translation of this technology. Nearly all reflective THz imaging systems employ dielectric substrate windows to overcome confounding effects from non-planar geometrics and surface roughness, and these contact methods share several significant problems: 1) Physical perturbation of the wound when contact is made; 2) risk of contamination of the wound site; 3) pressure exertion, which can affect fluid shifts as well as loss in the wound bed; 4) contribution to observed electromagnetic properties of the burn tissue; and 5) modulation of TWC contrast in THz burn imaging. Although windowless burn wound assessment is outwardly ideal, research findings in this dissertation suggest that the use of windows in THz imaging may not be a

shortcoming after all, but instead an advantage: dielectric window selection in THz burn imaging confers sensitivity to TWC in specific regions of tissue pathology (i.e. burn contact region vs. uninjured tissue) for distinguishing burn severity. This preliminary effort was the first to explore the effects of window refractive index on THz image contrast, however, future modeling work is required to reinforce the clinical significance of window-driven THz imaging. Specifically, simulations are needed to investigate the electromagnetic behavior between the tissue system and selected window and define how exactly window selection alters the hydration sensitivity of THz imaging to specific types of burn wound edema. Tissue under a window, which is typically modeled as a half-space, must be treated as a multi-layered, complex system that is characterized by gradients. These tissue layers are expected to exhibit their own interference effects; the distribution of TWC along the thickness of tissue layers and the layer composition, therefore, may alter the tissue's reflectivity. The effects of the addition of a window to a multilayer system, and therefore the sensitivity of THz imaging to the hydration state of deeper layers relative to the surface layers, must be investigated. These efforts will explore how THz images acquired with different dielectric windows (i.e. quartz and Mylar) vary not only in hydration sensitivity, but in information content, as the depth of tissue probed varies with the optical path length of the imaging system's window.

3) **Re-analyze THz-MRI correlations using a regression model –** It is widely believed that THz images of tissue are 2D reflection maps representing an *aggregate* tissue property. This property was confirmed to be mobile TWC (i.e. edema) based on a normalized-cross correlation performed between *in vivo* MRI measurements, that were analyzed at specific depths in a burn-induced model of edema, and single THz measurements as a function of time. A simple regression model may, in fact, better describe the relationship between aggregate THz reflectivity signal and serial (i.e.

additive) effects of TWC across skin layers observed in MRI.

4) **Perform large scale *in vivo* animal studies to evaluate the predictive power of THz burn wound and flap assessment** – Although the-first-of-its-kind, the pre-clinical work detailed in this dissertation is still very preliminary and must be performed in larger population sizes to test the accuracy and repeatability of THz imaging for burn wound and tissue flap assessment. Moreover, serial biopsies must be included at multiple time points in these longitudinal studies to compare wound outcome with THz TWC maps of pathology. THz prognostic indicators can, therefore, be developed to potentially predict tissue viability and distinguish burn severity within the first few hours after injury. Currently, our group is able to generate spatially resolved THz imagery of superficial tissue with high contrast, as shown on the left in **(Figure 12-2**: Future THz image display for clinicians. Pixels that

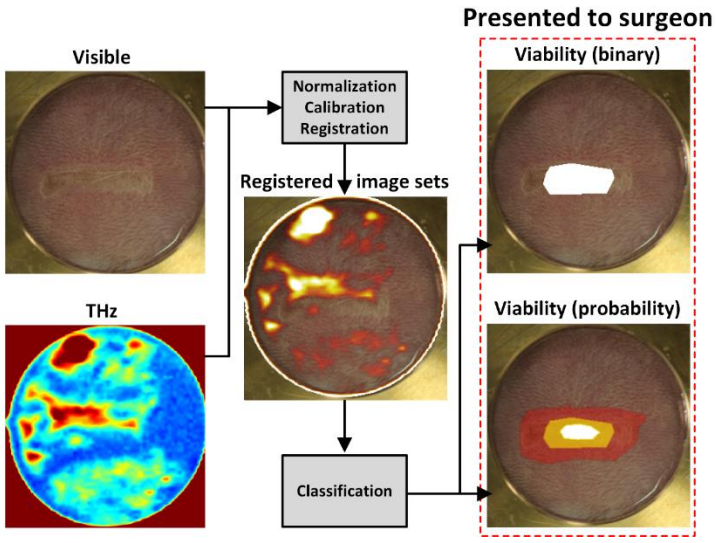

Figure 12-2: Future THz image display for clinicians

display high reflectivity are inferred to be more sensitive to TWC and have been superimposed on companion visible images to conveniently afford the spatial

localization of tissue regions experiencing greater edema. With the addition of prognostic indicators, our team ultimately aims to display a probability map of tissue burn severity or flap viability to a surgeon, thus facilitating both diagnosis of pathology and guided resection of compromised tissue.

Collectively, these THz imaging advancements may enable both timely and informed mapping of tissue edema and the extent of fluid extravasation into tissues in patients sustaining severe burn injuries, trauma, or other medical conditions leading to fluid shifts.

Beyond the direct implications of my research with respect to investigating and confirming TWC as the dominant contrast mechanism of THz imaging, I have also shown through my *in vivo* work in tissue flap and burn models that this technology can non-invasively and rapidly monitor variation in fluid shifts following injury. Such THz imaging capabilities have enabled assessment of burn severity and tissue viability earlier than visual inspection alone. The implications of these findings are twofold: first, it advances our understanding of THz image contrast and how it directly relates to tissue pathology. Second, it promotes a broader perspective towards the potential application of this technology for non-invasive and rapid detection of fluid shifts in any type of cutaneous injury or disease characterized by resultant edema, including skin cancer, ulcers, and dermatological disorders.

With continued *in vivo* use of THz sensing, the technology is well on its way towards gaining clinical traction, like MRI, as diagnostic imaging tool. Although a powerful tool, MRI of the skin, at present, functions mainly as a research technique. Slow data acquisition times, cost, and limited access essentially preclude the use of MRI for the detection of processes such as acute inflammation or edema. Although the spatial resolution of THz images is generally inferior to that of images generated by high-field animal MRI, the transverse resolution is on par with clinical MRI systems. Furthermore, the high contrast and speed (with respect to T_{2W} MRI) of THz imaging, combined with sensing capabilities that correlate with those of TWC-based MRI, support the

potential of THz imaging for applications in which surface tissue edema underlies the physiology of interest.

REFERENCES

[1] K. F. Cutting, R. J. White, and P. Mahoney, “Wound infection, dressings and pain, is there a relationship in the chronic wound?,” *Int. Wound J.*, vol. 10, no. 1, pp. 79–86, 2013.

[2] K. L. Baquerizo Nole *et al.*, “Wound research funding from alternative sources of federal funds in 2012,” *Wound Repair Regen.*, vol. 22, no. 3, pp. 295–300, 2014.

[3] W. Eichhorn, T. Auer, E.-D. Voy, and K. Hoffmann, “Laser Doppler imaging of axial and random pattern flaps in the maxillo-facial area. A preliminary report,” *J. Cranio-Maxillofac. Surg.*, vol. 22, no. 5, pp. 301–306, 1994.

[4] A. D. Jaskille, J. C. Ramella-Roman, J. W. Shupp, M. H. Jordan, and J. C. Jeng, “Critical review of burn depth assessment techniques: part II. Review of laser Doppler technology,” *J. Burn Care Res.*, vol. 31, no. 1, pp. 151–157, 2010.

[5] S. A. Pape, C. A. Skouras, and P. O. Byrne, “An audit of the use of laser Doppler imaging (LDI) in the assessment of burns of intermediate depth,” *Burns*, vol. 27, no. 3, pp. 233–239, 2001.

[6] Z. D. Taylor *et al.*, “THz medical imaging: in vivo hydration sensing,” *Terahertz Sci. Technol. IEEE Trans. On*, vol. 1, no. 1, pp. 201–219, 2011.

[7] P. H. Siegel, “Terahertz technology in biology and medicine,” in *Microwave Symposium Digest, 2004 IEEE MTT-S International*, 2004, vol. 3, p. 1575–1578 Vol.3.

[8] D. B. Bennett *et al.*, “Terahertz sensing in corneal tissues,” *J. Biomed. Opt.*, vol. 16, no. 5, pp. 57003–57003, 2011.

[9] P. Tewari *et al.*, “In vivo terahertz imaging of rat skin burns,” *J. Biomed. Opt.*, vol. 17, no. 4, pp. 0405031–0405033, 2012.

[10] M. H. Arbab, D. P. Winebrenner, T. C. Dickey, A. Chen, M. B. Klein, and P. D. Mourad, “Terahertz spectroscopy for the assessment of burn injuries in vivo,” *J. Biomed. Opt.*, vol. 18, no. 7, pp. 77004–77004, 2013.

[11] D. M. Mittleman, M. Gupta, R. Neelamani, R. G. Baraniuk, J. V. Rudd, and M. Koch, “Recent advances in terahertz imaging,” *Appl. Phys. B*, vol. 68, no. 6, pp. 1085–1094.

[12] R. M. Woodward *et al.*, “Terahertz pulse imaging in reflection geometry of human skin cancer and skin tissue,” *Phys. Med. Biol.*, vol. 47, no. 21, p. 3853, 2002.

[13] E. Pickwell, B. E. Cole, A. J. Fitzgerald, M. Pepper, and V. P. Wallace, “In vivo study of human skin using pulsed terahertz radiation,” *Phys. Med. Biol.*, vol. 49, no. 9, p. 1595, 2004.

[14] V. P. Wallace *et al.*, “Terahertz pulsed spectroscopy of human basal cell carcinoma,” *Appl. Spectrosc.*, vol. 60, no. 10, pp. 1127–1133, 2006.

[15] N. Bajwa *et al.*, “Reflective THz and MR imaging of burn wounds: a potential clinical validation of THz contrast mechanisms,” 2012, vol. 8496, p. 84960X–84960X–7.

[16] S. Ablett, T. A. Carpenter, L. D. Hall, R. J. Hodgson, and D. C. Salter, “MRI microscopy of human skin,” in *Soc. Magn. Reson. Med. 10th Annual Scientific Meeting*, 1991, p. 1251.

[17] F. Mirrashed and J. C. Sharp, “In vivo morphological characterisation of skin by MRI micro-imaging methods,” *Skin Res. Technol.*, vol. 10, no. 3, pp. 149–160, 2004.

[18] X.-C. Zhang and J. Xu, *Introduction to THz wave photonics*, vol. 29. Springer, 2010.

[19] P. Y. Han, G. C. Cho, and X.-C. Zhang, “Time-domain transillumination of biological tissues with terahertz pulses,” *Opt. Lett.*, vol. 25, no. 4, pp. 242–244, 2000.

[20] A. J. Fitzgerald, B. E. Cole, and P. F. Taday, “Nondestructive analysis of tablet coating thicknesses using terahertz pulsed imaging,” *J. Pharm. Sci.*, vol. 94, no. 1, pp. 177–183, 2005.

[21] R. H. Clothier and N. Bourne, “Effects of THz exposure on human primary keratinocyte differentiation and viability,” *J. Biol. Phys.*, vol. 29, no. 2–3, pp. 179–185, 2003.

[22] E. Berry *et al.*, “Do in vivo terahertz imaging systems comply with safety guidelines?,” *J. Laser Appl.*, vol. 15, no. 3, pp. 192–198, 2003.

[23] D. M. Mittleman, R. H. Jacobsen, and M. C. Nuss, “T-ray imaging,” *IEEE J. Sel. Top. Quantum Electron.*, vol. 2, no. 3, pp. 679–692, 1996.

[24] A. I. McIntosh, B. Yang, S. M. Goldup, M. Watkinson, and R. S. Donnan, “Terahertz spectroscopy: a powerful new tool for the chemical sciences?,” *Chem. Soc. Rev.*, vol. 41, no. 6, pp. 2072–2082, 2012.

[25] S. W. Smye, J. M. Chamberlain, A. J. Fitzgerald, and E. Berry, “The interaction between terahertz radiation and biological tissue,” *Phys. Med. Biol.*, vol. 46, no. 9, p. R101, 2001.

[26] M. Van Exter, C. Fattinger, and D. Grischkowsky, “Terahertz time-domain spectroscopy of water vapor,” *Opt. Lett.*, vol. 14, no. 20, pp. 1128–1130, 1989.

[27] J. T. Kindt and C. A. Schmuttenmaer, “Far-infrared dielectric properties of polar liquids probed by femtosecond terahertz pulse spectroscopy,” *J. Phys. Chem.*, vol. 100, no. 24, pp. 10373–10379, 1996.

[28] K. S. Cole and R. H. Cole, “Dispersion and absorption in dielectrics I. Alternating current characteristics,” *J. Chem. Phys.*, vol. 9, no. 4, pp. 341–351, 1941.

[29] B. E. Cole, R. M. Woodward, D. A. Crawley, V. P. Wallace, D. D. Arnone, and M. Pepper, “Terahertz imaging and spectroscopy of human skin in vivo,” in *Photonics West 2001-LASE*, 2001, pp. 1–10.

[30] R. M. Woodward, V. P. Wallace, D. D. Arnone, E. H. Linfield, and M. Pepper, “Terahertz pulsed imaging of skin cancer in the time and frequency domain,” *J. Biol. Phys.*, vol. 29, no. 2–3, pp. 257–259, 2003.

[31] M. Bruehlmeier *et al.*, “Measurement of the extracellular space in brain tumors using 76Br-bromide and PET,” *J. Nucl. Med.*, vol. 44, no. 8, pp. 1210–1218, 2003.

[32] K. F. A. Ross and R. E. Gordon, “Water in malignant tissue, measured by cell refractometry and nuclear magnetic resonance,” *J. Microsc.*, vol. 128, no. 1, pp. 7–21, 1982.

[33] J. H. Chen, H. E. Avram, L. E. Crooks, M. Arakawa, L. Kaufman, and A. C. Brito, “In vivo relaxation times and hydrogen density at 0.063-4.85 T in rats with implanted mammary adenocarcinomas.,” *Radiology*, vol. 184, no. 2, pp. 427–434, 1992.

[34] E. K. Rofstad, E. Steinsland, O. Kaalhus, Y. B. Chang, B. Høvik, and H. Lyng, “Magnetic Resonance Imaging of Human Melanoma Xenografts in Vivo: Proton Spin—lattice and Spin—spin Relaxation Times Versus Fractional Tumour Water Content and Fraction of Necrotic Tumour Tissue,” *Int. J. Radiat. Biol.*, vol. 65, no. 3, pp. 387–401, 1994.

[35] P. Knobloch *et al.*, “Medical THz imaging: an investigation of histo-pathological samples,” *Phys. Med. Biol.*, vol. 47, no. 21, p. 3875, 2002.

[36] E. Berry *et al.*, “Multispectral classification techniques for terahertz pulsed imaging: an example in histopathology,” *Med. Eng. Phys.*, vol. 26, no. 5, pp. 423–430, 2004.

[37] W. Ab, “Skin anatomy, physiology, and pathophysiology.,” *Nurs. Clin. North Am.*, vol. 34, no. 4, p. 777–97, v, 1999 1999.

[38] P. A. Kolarsick, M. A. Kolarsick, and C. Goodwin, “Anatomy and physiology of the skin,” *J. Dermatol. Nurses Assoc.*, vol. 3, no. 4, pp. 203–213, 2011.

[39] “Skin physiology.” [Online]. Available: http://www.sciencedirect.com/science/article/pii/S0263931906701673. [Accessed: 26-Oct-2016].

[40] R. C. Eberhart and A. Shitzer, *Heat Transfer in Medicine and Biology: Analysis and Applications*. Springer Science & Business Media, 2012.

[41] J. A. McGrath, R. A. J. Eady, and F. M. Pope, “Anatomy and organization of human skin,” *Rooks Textb. Dermatol. Burns T B Cox N Al Eds*, vol. 8, 2004.

[42] W. Paul and C. P. Sharma, *Advances in Wound Healing Materials: Science and Skin Engineering*. Smithers Rapra Technology, 2015.

[43] R. R. Warner, M. C. Myers, and D. A. Taylor, “Electron probe analysis of human skin: determination of the water concentration profile,” *J. Invest. Dermatol.*, vol. 90, no. 2, pp. 218–224, 1988.

[44] H. Tagami, M. Ohi, K. Iwatsuki, Y. Kanamaru, M. Yamada, and B. Ichijo, “Evaluation of the skin surface hydration in vivo by electrical measurement,” *J. Invest. Dermatol.*, vol. 75, no. 6, pp. 500–507, 1980.

[45] R. L. Rietschel, “A method to evaluate skin moisturizers in vivo,” *J. Invest. Dermatol.*, vol. 70, no. 3, pp. 152–155, 1978.

[46] F. Mirrashed and J. C. Sharp, “In vivo quantitative analysis of the effect of hydration (immersion and Vaseline treatment) in skin layers using high-resolution MRI and magnetisation transfer contrast,” *Skin Res. Technol.*, vol. 10, no. 1, pp. 14–22, 2004.

[47] S. Aubry, C. Casile, P. Humbert, J. Jehl, C. Vidal, and B. Kastler, “Feasibility study of 3-T MR imaging of the skin,” *Eur. Radiol.*, vol. 19, no. 7, pp. 1595–1603, 2009.

[48] N. Sans, M. Faruch, H. Chiavassa-Gandois, C. L. C. de Ribes, C. Paul, and J.-J. Railhac, “High-resolution magnetic resonance imaging in study of the skin: normal patterns,” *Eur. J. Radiol.*, vol. 80, no. 2, pp. e176–e181, 2011.

[49] S. Richard *et al.*, “Characterization of the Skin In Vivo by High Resolution Magnetic Resonance Imaging: Water Behavior and Age-Related Effects,” *J. Invest. Dermatol.*, vol. 100, no. 5, pp. 705–709, May 1993.

[50] T. Ozawa and M. Takahashi, “Shin hydration: recent advances,” *Acta Derm. Venereol. Suppl. (Stockh.)*, no. 185, pp. 26–28, 1994.

[51] M. Lodén, “The increase in skin hydration after application of emollients with different amounts of lipids.,” *Acta Derm. Venereol.*, vol. 72, no. 5, pp. 327–330, 1992.

[52] E. Berardesca and H. I. Maibach, “Transepidermal water loss and skin surface hydration in the non invasive assessment of stratum corneum function.,” *Dermatosen Beruf Umw. Occup. Environ.*, vol. 38, no. 2, pp. 50–53, 1989.

[53] R. O. Potts, D. B. Guzek, R. R. Harris, and J. E. McKie, “A noninvasive, in vivo technique to quantitatively measure water concentration of the stratum corneum using attenuated total-reflectance infrared spectroscopy,” *Arch. Dermatol. Res.*, vol. 277, no. 6, pp. 489–495, 1985.

[54] M. G. Sowa, J. R. Payette, and H. H. Mantsch, “Near-infrared spectroscopic assessment of tissue hydration following surgery,” *J. Surg. Res.*, vol. 86, no. 1, pp. 62–69, 1999.

[55] A. Zemtsov and L. Dixon, “Magnetic resonance in dermatology,” *Arch. Dermatol.*, vol. 129, no. 2, pp. 215–218, 1993.

[56] J. Albers, A. Schroeder, R. de Simone, R. Möckel, C.-F. Vahl, and S. Hagl, “3D Evaluation of Myocardial Edema: Experimental Study on 22 Pigs Using Magnetic Resonance and Tissue Analysis*,” *Thorac. Cardiovasc. Surg.*, vol. 49, no. 4, pp. 199–203, Aug. 2001.

[57] N. J. Khoury, G. Y. El-Khoury, and M. H. Kathol, “MRI diagnosis of diabetic muscle infarction: report of two cases,” *Skeletal Radiol.*, vol. 26, no. 2, pp. 122–127, Feb. 1997.

[58] B. Querleux, M. M. Yassine, L. Darrasse, H. Saint-Jalmes, M. Sauzade, and J. L. Leveque, “Magnetic resonance imaging of the skin. A comparison with the ultrasonic technique,” *Bioeng. Skin*, vol. 4, no. 1, pp. 1–14, 1988.

[59] S. Ablett, N. G. Burdett, T. A. Carpenter, L. D. Hall, and D. C. Salter, “Short echo time MRI enables visualisation of the natural state of human stratum corneum water in vivo,” *Magn. Reson. Imaging*, vol. 14, no. 4, pp. 357–360, 1996.

[60] J. Bittoun *et al.*, “In vivo high-resolution MR imaging of the skin in a whole-body system at 1.5 T.,” *Radiology*, vol. 176, no. 2, pp. 457–460, 1990.

[61] S. Richard *et al.*, “In Vivo Proton Relaxation Times Analysis of the Skin Layers by Magnetic Resonance Imaging,” *J. Invest. Dermatol.*, vol. 97, no. 1, pp. 120–125, Jul. 1991.

[62] E. Durand and others, “Enhanced spatial resolution for skin magnetic resonance imaging in vivo,” in *13th annual meeting of ESMRMB, Prague. 1 (2)*, 1996, pp. 125–126.

[63] H. K. Song, F. W. Wehrli, and J. Ma, “In vivo MR microscopy of the human skin,” *Magn. Reson. Med.*, vol. 37, no. 2, pp. 185–191, 1997.

[64] R. H. Demling, “The burn edema process: current concepts,” *J. Burn Care Res.*, vol. 26, no. 3, pp. 207–227, 2005.

[65] J. M. Still, E. J. Law, K. G. Klavuhn, T. C. Island, and J. Z. Holtz, “Diagnosis of burn depth using laser-induced indocyanine green fluorescence: a preliminary clinical trial,” *Burns*, vol. 27, no. 4, pp. 364–371, 2001.

[66] S. Monstrey, H. Hoeksema, J. Verbelen, A. Pirayesh, and P. Blondeel, “Assessment of burn depth and burn wound healing potential,” *burns*, vol. 34, no. 6, pp. 761–769, 2008.

[67] D. M. Jackson, “The diagnosis of the depth of burning,” *Br. J. Surg.*, vol. 40, no. 164, pp. 588–596, 1953.

[68] S. Monstrey, H. Hoeksema, J. Verbelen, A. Pirayesh, and P. Blondeel, *Burns*, vol. 33, p. 761, 2008.

[69] A. D. Jaskille, J. W. Shupp, M. H. Jordan, and J. C. Jeng, “Critical review of burn depth assessment techniques: Part I. Historical review,” *J. Burn Care Res.*, vol. 30, no. 6, pp. 937–947, 2009.

[70] L. Devgan, S. Bhat, S. Aylward, and R. J. Spence, “Modalities for the assessment of burn wound depth,” *J Burns Wounds*, vol. 5, p. e2, 2006.

[71] B. H. Park, C. Saxer, S. M. Srinivas, J. S. Nelson, and J. F. de Boer, “In vivo burn depth determination by high-speed fiber-based polarization sensitive optical coherence tomography,” *J. Biomed. Opt.*, vol. 6, no. 4, pp. 474–479, 2001.

[72] M. C. Pierce, R. L. Sheridan, B. H. Park, B. Cense, and J. F. de Boer, “Collagen denaturation can be quantified in burned human skin using polarization-sensitive optical coherence tomography,” *Burns*, vol. 30, no. 6, pp. 511–517, 2004.

[73] A. G. Hargroder, J. E. Davidson Sr, D. G. Luther, and J. F. Head, “Infrared imaging of burn wounds to determine burn depth,” in *AeroSense’99*, 1999, pp. 103–108.

[74] J. Ruminski, M. Kaczmarek, A. Renkielska, and A. Nowakowski, “Thermal parametric imaging in the evaluation of skin burn depth,” *IEEE Trans. Biomed. Eng.*, vol. 54, no. 2, pp. 303–312, 2007.

[75] J. E. GATTI, D. LAROSSA, D. G. SILVERMAN, and C. E. HARTFORD, “Evaluation of the burn wound with perfusion fluorometry.,” *J. Trauma Acute Care Surg.*, vol. 23, no. 3, pp. 202–206, 1983.

[76] T. Gambichler, G. Moussa, M. Sand, D. Sand, P. Altmeyer, and K. Hoffmann, “Applications of optical coherence tomography in dermatology,” *J. Dermatol. Sci.*, vol. 40, no. 2, pp. 85–94, 2005.

[77] S. M. Srinivas *et al.*, “Determination of burn depth by polarization-sensitive optical coherence tomography,” *J. Biomed. Opt.*, vol. 9, no. 1, pp. 207–212, 2004.

[78] J. C. Jeng *et al.*, “Laser Doppler imaging determines need for excision and grafting in advance of clinical judgment: a prospective blinded trial,” *Burns*, vol. 29, no. 7, pp. 665–670, 2003.

[79] H. Hoeksema *et al.*, “Accuracy of early burn depth assessment by laser Doppler imaging on different days post burn,” *Burns*, vol. 35, no. 1, pp. 36–45, 2009.

[80] R. H. Demling, “Burn Edema. Part I: Pathogenesis. [Review],” *J. Burn Care*, vol. 3, no. 3, pp. 138–149, Jun. 1982.

[81] R. H. Demling, R. A. Gunther, B. Harms, and G. Kramer, “Burn Edema Part II: Complications, Prevention, and Treatment.,” *J. Burn Care Res.*, vol. 3, no. 4, p. 799, 1982.

[82] M. P. Kinsky, S. C. Guha, B. M. Button, and G. C. Kramer, “The role of interstitial starling forces in the pathogenesis of burn edema.,” *J. Burn Care Res.*, vol. 19, no. 1, pp. 1–9, 1998.

[83] O. Cope and F. D. Moore, “A study of capillary permeability in experimental burns and burn shock using radioactive dyes in blood and lymph,” *J. Clin. Invest.*, vol. 23, no. 2, p. 241, 1944.

[84] A. G, “Microvascular permeability to macromolecules in thermal injury.,” *Acta Physiol. Scand. Suppl.*, vol. 463, pp. 111–122, Dec. 1978.

[85] T. Lund, H. Onarheim, and R. K. Reed, “Pathogenesis of edema formation in burn injuries,” *World J. Surg.*, vol. 16, no. 1, pp. 2–9, Jan. 1992.

[86] C. R. Baxter, “Fluid volume and electrolyte changes of the early postburn period,” *Clin. Plast. Surg.*, vol. 1, no. 4, pp. 693–703, Oct. 1974.

[87] C. R. Baxter and T. Shires, “Physiological response to crystalloid resuscitation of severe burns,” *Ann. N. Y. Acad. Sci.*, vol. 150, no. 3, pp. 874–894, 1968.

[88] “Escharotomy and Decompressive Therapies in Burns : Journal of Burn Care & Research.” [Online]. Available: http://journals.lww.com/burncareresearch/Abstract/2009/09000/Escharotomy_and_Decompressive_Therapies_in_Burns.1.aspx. [Accessed: 26-Oct-2016].

[89] J. P. Remensnyder, “Topography of tissue oxygen tension changes in acute burn edema,” *Arch. Surg.*, vol. 105, no. 3, pp. 477–482, 1972.

[90] H. F. Carvajal, H. A. Linares, and B. H. Brouhard, “Relationship of burn size to vascular permeability changes in rats.,” *Surg. Gynecol. Obstet.*, vol. 149, no. 2, pp. 193–202, 1979.

[91] B. H. Brouhard, H. F. Carvajal, and H. A. Linares, “Burn edema and protein leakage in the rat: I. Relationship to time of injury,” *Microvasc. Res.*, vol. 15, no. 2, pp. 221–228, 1978.

[92] H. J. Granger, “Role of the interstitial matrix and lymphatic pump in regulation of transcapillary fluid balance,” *Microvasc. Res.*, vol. 18, no. 2, pp. 209–216, 1979.

[93] L. L. LEAPE, “Initial changes in burns: tissue changes in burned and unburned skin of rhesus monkeys.,” *J. Trauma Acute Care Surg.*, vol. 10, no. 6, pp. 488–492, 1970.

[94] H. Onarheim and R. K. Reed, “Thermal skin injury: effect of fluid therapy on the transcapillary colloid osmotic gradient,” *J. Surg. Res.*, vol. 50, no. 3, pp. 272–278, 1991.

[95] H. Sakurai, M. Nozaki, L. D. Traber, H. K. Hawkins, and D. L. Traber, “Microvascular changes in large flame burn wound in sheep,” *Burns*, vol. 28, no. 1, pp. 3–9, 2002.

[96] R. H. DEMLING, R. B. MAZESS, R. M. WITT, and W. H. WOLBERG, “The study of burn wound edema using dichromatic absorptiometry.,” *J. Trauma Acute Care Surg.*, vol. 18, no. 2, pp. 124–128, 1978.

[97] R. H. Demling, M. Smith, R. Gunther, T. Wandzilak, and N. C. Pederson, “Use of a chronic prefemoral lymphatic fistula for monitoring systemic capillary integrity in unanesthetized sheep,” *J. Surg. Res.*, vol. 31, no. 2, pp. 136–144, 1981.

[98] E. M. Renkin, W. L. Joyner, C. H. Sloop, and P. D. Watson, “Influence of venous pressure on plasma-lymph transport in the dog’s paw: convective and dissipative mechanisms,” *Microvasc. Res.*, vol. 14, no. 2, pp. 191–204, 1977.

[99] W. W. L. Glenn, D. K. Peterson, and C. K. Drinker, “The flow of lymph from burned tissue, with particular reference to the effects of fibrin formation upon lymph drainage and composition,” *Surgery*, vol. 12, no. 685–693, p. 191, 1942.

[100] B. A. Harms, B. I. Bodai, M. Smith, R. Gunther, J. Flynn, and R. H. Demling, “Prostaglandin release and altered microvascular integrity after burn injury,” *J. Surg. Res.*, vol. 31, no. 4, pp. 274–280, 1981.

[101] N. B. Pillar, “A comparison of the effectiveness of antiinflammatory drugs on thermal edema,” *Br J Exp*, vol. 56, pp. 554–60, 1975.

[102] L. L. Leape, “Early burn wound changes,” *J. Pediatr. Surg.*, vol. 3, no. 2, pp. 292–299, Apr. 1968.

[103] I. L. Leape, “Kinetics of burn edema formation in primates.,” *Ann. Surg.*, vol. 176, no. 2, pp. 223–226, Aug. 1972.

[104]"AO Surgery Reference." [Online]. Available: https://www2.aofoundation.org/wps/portal/!ut/p/a0/04_Sj9CPykssy0xPLMnMz0vMAfGjzOKN_A0M3D2DDbz9_UMMDRyDXQ3dw9wMDAzMjfULsh0VAbWjLW0!/?bone=Foot&segment=Calcaneus&contentUrl=/srg/popup/further_reading/PFxM2/43_7_Soft-tissue_loss_repair_foot.jsp. [Accessed: 26-Oct-2016].

[105]J. R. Payette *et al.*, "Assessment of Skin Flaps Using Optically Based Methods for Measuring Blood Flow and Oxygenation:," *Plast. Reconstr. Surg.*, vol. 115, no. 2, pp. 539–546, Feb. 2005.

[106]M. Bergkvist, J. Henricson, F. Iredahl, E. Tesselaar, F. Sjöberg, and S. Farnebo, "Assessment of microcirculation of the skin using Tissue Viability Imaging: A promising technique for detecting venous stasis in the skin," *Microvasc. Res.*, vol. 101, pp. 20–25, 2015.

[107]L. Di Sieno *et al.*, "Toward noninvasive assessment of flap viability with time-resolved diffuse optical tomography: a preclinical test on rats," *J. Biomed. Opt.*, vol. 21, no. 2, pp. 025004–025004, 2016.

[108]Q. Yang *et al.*, "The effect of early detection of anterolateral thigh free flap crisis on the salvage success rate, based on 10 years of experience and 1072 flaps," *Int. J. Oral Maxillofac. Surg.*, vol. 43, no. 9, pp. 1059–1063, 2014.

[109]K.-T. Chen *et al.*, "Timing of presentation of the first signs of vascular compromise dictates the salvage outcome of free flap transfers," *Plast. Reconstr. Surg.*, vol. 120, no. 1, pp. 187–195, 2007.

[110]"Free Flap Reexploration: Indications, Treatment, and Outcome... : Plastic and Reconstructive Surgery." [Online]. Available: http://journals.lww.com/plasreconsurg/Abstract/2007/06000/Free_Flap_Reexploration__Indications,_Treatment,.18.aspx. [Accessed: 26-Oct-2016].

[111]L. Di Sieno *et al.*, “Toward noninvasive assessment of flap viability with time-resolved diffuse optical tomography: a preclinical test on rats,” *J. Biomed. Opt.*, vol. 21, no. 2, pp. 025004–025004, 2016.

[112]G. S. Lazarus *et al.*, “Definitions and guidelines for assessment of wounds and evaluation of healing,” *Wound Repair Regen.*, vol. 2, no. 3, pp. 165–170, Jul. 1994.

[113]C. Holm, M. Mayr, E. Höfter, A. Becker, U. J. Pfeiffer, and W. Mühlbauer, “Intraoperative evaluation of skin-flap viability using laser-induced fluorescence of indocyanine green,” *Br. J. Plast. Surg.*, vol. 55, no. 8, pp. 635–644, 2002.

[114]I. A. Pestana, B. Coan, D. Erdmann, J. Marcus, L. S. Levin, and M. R. Zenn, “Early Experience with Fluorescent Angiography in Free-Tissue Transfer Reconstruction:,” *Plast. Reconstr. Surg.*, vol. 123, no. 4, pp. 1239–1244, Apr. 2009.

[115]M. F. Stranc, M. G. Sowa, B. Abdulrauf, and H. H. Mantsch, “Assessment of tissue viability using near-infrared spectroscopy,” *Br. J. Plast. Surg.*, vol. 51, no. 3, pp. 210–217, 1998.

[116]F. Arnold, C. F. He, C. Y. Jia, and G. W. Cherry, “Perfusion imaging of skin island flap blood flow by a scanning laser-Doppler technique,” *Br. J. Plast. Surg.*, vol. 48, no. 5, pp. 280–287, 1995.

[117]Y.-S. Lee, *Principles of terahertz science and technology*, vol. 170. Springer Science & Business Media, 2009.

[118]B. Ferguson and X.-C. Zhang, “Materials for terahertz science and technology,” *Nat. Mater.*, vol. 1, no. 1, pp. 26–33, 2002.

[119]G. Zhao, R. N. Schouten, N. Van der Valk, W. T. Wenckebach, and P. C. M. Planken, “Design and performance of a THz emission and detection setup based on a semi-insulating GaAs emitter,” *Rev. Sci. Instrum.*, vol. 73, no. 4, pp. 1715–1719, 2002.

[120]N. Katzenellenbogen and D. Grischkowsky, “Efficient generation of 380 fs pulses of THz radiation by ultrafast laser pulse excitation of a biased metal-semiconductor interface,” *Appl. Phys. Lett.*, vol. 58, no. 3, pp. 222–224, 1991.

[121]“Phys. Rev. Lett. 9, 446 (1962) - Optical Rectification.” [Online]. Available: http://journals.aps.org/prl/abstract/10.1103/PhysRevLett.9.446. [Accessed: 26-Oct-2016].

[122]N. Karpowicz, H. Zhong, J. Xu, K.-I. Lin, J.-S. Hwang, and X. C. Zhang, “Comparison between pulsed terahertz time-domain imaging and continuous wave terahertz imaging,” *Semicond. Sci. Technol.*, vol. 20, no. 7, p. S293, 2005.

[123]M. Tonouchi, “Cutting-edge terahertz technology,” *Nat. Photonics*, vol. 1, no. 2, pp. 97–105, Feb. 2007.

[124]K. P. Cheung and D. H. Auston, “Excitation of coherent phonon polaritons with femtosecond optical pulses,” *Phys. Rev. Lett.*, vol. 55, no. 20, p. 2152, 1985.

[125]B. B. Hu, X.-C. Zhang, and D. H. Auston, “Terahertz radiation induced by subband-gap femtosecond optical excitation of GaAs,” *Phys. Rev. Lett.*, vol. 67, no. 19, p. 2709, 1991.

[126]M. B. Ketchen *et al.*, “Generation of subpicosecond electrical pulses on coplanar transmission lines,” *Appl. Phys. Lett.*, vol. 48, no. 12, pp. 751–753, 1986.

[127]M. Y. Frankel, J. F. Whitaker, G. A. Mourou, F. W. Smith, and A. R. Calawa, “High-voltage picosecond photoconductor switch based on low-temperature-grown GaAs,” *IEEE Trans. Electron Devices*, vol. 37, no. 12, pp. 2493–2498, 1990.

[128]Z. D. Taylor *et al.*, “Reflective terahertz imaging of porcine skin burns,” *Opt. Lett.*, vol. 33, no. 11, pp. 1258–1260, 2008.

[129]Z. D. Taylor *et al.*, “Active THz medical imaging using broadband direct detection,” 2013, vol. 8624, pp. 862403-862403–10.

[130]R. S. Singh *et al.*, “THz imaging of skin hydration: motivation for the frequency band,” in *BiOS*, 2010, pp. 755513–755513.

[131]R. S. Singh *et al.*, “Terahertz sensing of corneal hydration,” in *2010 Annual International Conference of the IEEE Engineering in Medicine and Biology*, 2010, pp. 3021–3024.

[132]S. Sung *et al.*, “Fast-scanning THz medical imaging system for clinical application,” 2012, vol. 8496, p. 84960S–84960S–7.

[133] Bajwa, N., Tewari,P., Garritano,J., Sung,S., Nowroozi, B., Sayre, J., Grundfest, G., Taylor,Z., “Reflective THz Sensing of Skin Burns: In vivo Imaging Results,” *IEEE Trans Terahertz Sci Technol*, Submitting in 2016.

[134] E. R. Brown *et al.*, “THz imaging of skin tissue—Exploiting the strong reflectivity of liquid water,” in *35th International Conference on Infrared, Millimeter, and Terahertz Waves*, 2010, pp. 1–2.

[135] D. Mittleman, *Appl Phys B Lasers Opt*, vol. 68, p. 1085, 1999.

[136] Z. D. Taylor, R. S. Singh, M. O. Culjat, J. Y. Suen, W. S. Grundfest, and E. R. Brown, “THz imaging based on water-concentration contrast,” in *SPIE Defense and Security Symposium*, 2008, p. 69490D–69490D.

[137] J. P. Dougherty, G. D. Jubic, and W. L. Kiser Jr, “Terahertz imaging of burned tissue,” in *Integrated Optoelectronic Devices 2007*, 2007, p. 64720N–64720N.

[138] D. D. Arnone *et al.*, “Applications of terahertz (THz) technology to medical imaging,” 1999, vol. 3828, pp. 209–219.

[139] T. Kleine-Ostmann *et al.*, “Continuous-wave THz imaging,” *Electron. Lett.*, vol. 37, no. 24, p. 1, 2001.

[140] K. J. Siebert *et al.*, “All-optoelectronic continuous wave THz imaging for biomedical applications,” *Phys. Med. Biol.*, vol. 47, no. 21, p. 3743, 2002.

[141] B. B. Hu and M. C. Nuss, “Imaging with terahertz waves,” *Opt. Lett.*, vol. 20, no. 16, p. 1716, Aug. 1995.

[142] A. J. Fitzgerald, E. Berry, N. N. Zinovev, G. C. Walker, M. A. Smith, and J. M. Chamberlain, “An introduction to medical imaging with coherent terahertz frequency radiation,” *Phys. Med. Biol.*, vol. 47, no. 7, p. R67, 2002.

[143] A. J. Fitzgerald, E. Berry, N. N. Zinovev, G. C. Walker, M. A. Smith, and J. M. Chamberlain, “An introduction to medical imaging with coherent terahertz frequency radiation,” *Phys. Med. Biol.*, vol. 47, no. 7, p. R67, 2002.

[144]M. H. Arbab, T. C. Dickey, D. P. Winebrenner, A. Chen, M. B. Klein, and P. D. Mourad, “Terahertz reflectometry of burn wounds in a rat model,” *Biomed. Opt. Express*, vol. 2, no. 8, pp. 2339–2347, 2011.

[145]M. H. Arbab, T. C. Dickey, D. P. Winebrenner, A. Chen, and P. D. Mourad, “Characterization of burn injuries using terahertz time-domain spectroscopy,” in *SPIE BiOS*, 2011, p. 78900Q–78900Q.

[146]M. H. Arbab, D. Winebrenner, T. C. Dickey, M. B. Klein, A. Chen, and P. D. Mourad, “A Noninvasive Terahertz Assessment of 2nd and 3rd Degree Burn Wounds,” 2012, p. CTu3B.3.

[147]W. A. Dorsett-Martin, “Rat models of skin wound healing: A review,” *Wound Repair Regen.*, vol. 12, no. 6, pp. 591–599, Nov. 2004.

[148]R. L. Bronaugh, R. F. Stewart, and E. R. Congdon, “Methods for in vitro percutaneous absorption studies II. Animal models for human skin,” *Toxicol. Appl. Pharmacol.*, vol. 62, no. 3, pp. 481–488, 1982.

[149]F. P. Schmook, J. G. Meingassner, and A. Billich, “Comparison of human skin or epidermis models with human and animal skin in in-vitro percutaneous absorption,” *Int. J. Pharm.*, vol. 215, no. 1, pp. 51–56, 2001.

[150]W. Meyer, R. Schwarz, and K. Neurand, “The Skin of Domestic Mammals as a Model for the Human Skin, with Special Reference to the Domestic Pig1,” in *Skin-Drug Application and Evaluation of Environmental Hazards*, Karger Publishers, 1978, pp. 39–52.

[151]T. N. Meyer and A. L. da Silva, “A standard burn model using rats,” *Acta Cirúrgica Bras.*, vol. 14, no. 4, pp. 0–0, 1999.

[152]R. K. Cribbs, M. H. Luquette, and G. E. Besner, “A standardized model of partial thickness scald burns in mice,” *J. Surg. Res.*, vol. 80, no. 1, pp. 69–74, 1998.

[153]T. Kaufman, S. N. Lusthaus, U. Sagher, and M. R. Wexler, “Deep partial skin thickness burns: a reproducible animal model to study burn wound healing,” *Burns*, vol. 16, no. 1, pp. 13–16, 1990.

[154]J. S. Knabl *et al.*, “Controlled partial skin thickness burns: an animal model for studies of burnwound progression,” *Burns*, vol. 25, no. 3, pp. 229–235, 1999.

[155]A. Wagner-Gentner, U. U. Graf, D. Rabanus, and K. Jacobs, “Low loss THz window,” *Infrared Phys. Technol.*, vol. 48, no. 3, pp. 249–253, Aug. 2006.

[156]“IEEE Xplore Document - Effects of window index and thickness on hydration sensitivity and probing depth of THz imaging systems.” [Online]. Available: http://ieeexplore.ieee.org/document/6956003/?arnumber=6956003&tag=1. [Accessed: 26-Oct-2016].

[157]“IEEE Xplore Document - THz hydration sensitivity: Dielectric substrate window considerations.” [Online]. Available: http://ieeexplore.ieee.org/document/6928148/?arnumber=6928148. [Accessed: 26-Oct-2016].

[158]H. Hoshina, A. Hayashi, N. Miyoshi, F. Miyamaru, and C. Otani, “Terahertz pulsed imaging of frozen biological tissues,” *Appl. Phys. Lett.*, vol. 94, no. 12, p. 123901, 2009.

[159]A. J. Fitzgerald *et al.*, “Terahertz pulsed imaging of human breast tumors 1,” *Radiology*, vol. 239, no. 2, pp. 533–540, 2006.

[160]M. Sajadi, M. Wolf, and T. Kampfrath, “Terahertz-field-induced optical birefringence in common window and substrate materials,” *Opt. Express*, vol. 23, no. 22, pp. 28985–28992, 2015.

[161]B. Ung, A. Dupuis, K. Stoeffler, C. Dubois, and M. Skorobogatiy, “High-refractive-index composite materials for terahertz waveguides: trade-off between index contrast and absorption loss,” *JOSA B*, vol. 28, no. 4, pp. 917–921, 2011.

[162] D. B. Bennett, W. Li, Z. D. Taylor, W. S. Grundfest, and E. R. Brown, “Stratified media model for terahertz reflectometry of the skin,” *IEEE Sens. J.*, vol. 11, no. 5, pp. 1253–1262, 2011.

[163] R. M. Woodward, V. P. Wallace, D. D. Arnone, E. H. Linfield, and M. Pepper, “Terahertz pulsed imaging of skin cancer in the time and frequency domain,” *J. Biol. Phys.*, vol. 29, no. 2–3, pp. 257–259, 2003.

[164] “IEEE Xplore Document - A Feasibility Study of Burn Wound Depth Assessment Using Terahertz Pulsed Imaging.” [Online]. Available: http://ieeexplore.ieee.org/document/4338310/?arnumber=4338310&tag=1. [Accessed: 26-Oct-2016].

[165] M. Dutta, A. S. Bhalla, and R. Guo, “THz Imaging of Skin Burn: Seeing the Unseen—An Overview,” *Adv. Wound Care*, Apr. 2016.

[166] H. J. Liebe, G. A. Hufford, and T. Manabe, “A model for the complex permittivity of water at frequencies below 1 THz,” *Int. J. Infrared Millim. Waves*, vol. 12, no. 7, pp. 659–675, 1991.

[167] E. Pickwell, B. E. Cole, A. J. Fitzgerald, V. P. Wallace, and M. Pepper, “Simulation of terahertz pulse propagation in biological systems,” *Appl. Phys. Lett.*, vol. 84, no. 12, pp. 2190–2192, 2004.

[168] Z. D. Taylor *et al.*, “THz and mm-Wave Sensing of Corneal Tissue Water Content: Electromagnetic Modeling and Analysis,” *IEEE Trans. Terahertz Sci. Technol.*, vol. 5, no. 2, pp. 170–183, Mar. 2015.

[169] A. Maccabi *et al.*, “Reflectivity measurements of water and dioxane mixtures using a 100 GHz Gunn diode source,” 2013, vol. 8585, p. 85850X–85850X–7.

[170] M. Ney and I. Abdulhalim, “Modeling of reflectometric and ellipsometric spectra from the skin in the terahertz and submillimeter waves region,” *J. Biomed. Opt.*, vol. 16, no. 6, p. 67006, 2011.

[171] A. J. Fitzgerald, E. Berry, R. E. Miles, N. N. Zinovev, M. A. Smith, and J. M. Chamberlain, "Evaluation of image quality in terahertz pulsed imaging using test objects," *Phys. Med. Biol.*, vol. 47, no. 21, p. 3865, 2002.

[172] C. Reid, A. P. Gibson, J. C. Hebden, and V. P. Wallace, "The use of tissue mimicking phantoms in analysing contrast in THz pulsed imaging of biological tissue," in *2007 Joint 32nd International Conference on Infrared and Millimeter Waves and the 15th International Conference on Terahertz Electronics*, 2007, pp. 567–568.

[173] E. L. Madsen, J. A. Zagzebski, R. A. Banjavie, and R. E. Jutila, "Tissue mimicking materials for ultrasound phantoms," *Med. Phys.*, vol. 5, no. 5, pp. 391–394, 1978.

[174] J. C. Blechinger, E. L. Madsen, and G. R. Frank, "Tissue-mimicking gelatin–agar gels for use in magnetic resonance imaging phantoms," *Med. Phys.*, vol. 15, no. 4, pp. 629–636, 1988.

[175] B. Ferguson, S. Wang, D. Gray, D. Abbott, and X.-C. Zhang, "Identification of biological tissue using chirped probe THz imaging," *Microelectron. J.*, vol. 33, no. 12, pp. 1043–1051, Dec. 2002.

[176] G. C. Walker, E. Berry, S. W. Smye, and D. S. Brettle, "Materials for phantoms for terahertz pulsed imaging," *Phys. Med. Biol.*, vol. 49, no. 21, p. N363, 2004.

[177] Y. Shi and L. Wang, "Collective vibrational spectra of α-and γ-glycine studied by terahertz and Raman spectroscopy," *J. Phys. Appl. Phys.*, vol. 38, no. 19, p. 3741, 2005.

[178] C. Zhang and S. M. Durbin, "Hydration-induced far-infrared absorption increase in myoglobin," *J. Phys. Chem. B*, vol. 110, no. 46, pp. 23607–23613, 2006.

[179] K. M. Quan, G. B. Christison, H. A. MacKenzie, and P. Hodgson, "Glucose determination by a pulsed photoacoustic technique: an experimental study using a gelatin-based tissue phantom," *Phys. Med. Biol.*, vol. 38, no. 12, p. 1911, 1993.

[180] M.-C. Vackier, B. P. Hills, and D. N. Rutledge, "An NMR relaxation study of the state of water in gelatin gels," *J. Magn. Reson.*, vol. 138, no. 1, pp. 36–42, 1999.

[181] J. W. Lamb, “Miscellaneous data on materials for millimetre and submillimetre optics,” *Int. J. Infrared Millim. Waves*, vol. 17, no. 12, pp. 1997–2034, 1996.

[182] F. Franconi *et al.*, “Measurement of epidermal moisture content by magnetic resonance imaging: assessment of a hydration cream,” *Br. J. Dermatol.*, vol. 132, no. 6, pp. 913–917, 1995.

[183] T. F. Budinger and P. C. Lauterbur, “Nuclear magnetic resonance technology for medical studies,” *Science*, vol. 226, no. 4672, pp. 288–298, Oct. 1984.

[184] J. F. Wang, M. E. Olson, C. R. Reno, W. Kulyk, J. B. Wright, and D. A. Hart, “Molecular and Cell Biology of Skin Wound Healing in a Pig Model,” *Connect. Tissue Res.*, vol. 41, no. 3, pp. 195–211, Jan. 2000.

[185] I. Joris and G. Majno, *Cells, tissues, and disease: principles of general pathology*. Oxford University Press, USA, 2004.

[186] M. J. Koruda *et al.*, “Assessing burn wound depth using in vitro nuclear magnetic resonance (NMR),” *J. Surg. Res.*, vol. 40, no. 5, pp. 475–481, May 1986.

[187] I. L. Cameron, V. A. Ord, and G. D. Fullerton, “Characterization of proton NMR relaxation times in normal and pathological tissues by correlation with other tissue parameters,” *Magn. Reson. Imaging*, vol. 2, no. 2, pp. 97–106, Jan. 1984.

[188] P. A. WARD and G. O. TILL, “Pathophysiologic events related to thermal injury of skin.,” *J. Trauma Acute Care Surg.*, vol. 30, pp. 75–79, 1990.

[189] D. Heimbach, L. Engrav, B. Grube, and J. Marvin, “Burn depth: a review,” *World J. Surg.*, vol. 16, no. 1, pp. 10–15, 1992.

[190] A. M. I. Watts, M. P. H. Tyler, M. E. Perry, A. H. N. Roberts, and D. A. McGrouther, “Burn depth and its histological measurement,” *Burns*, vol. 27, no. 2, pp. 154–160, 2001.

[191] V. Singh, L. Devgan, S. Bhat, and S. M. Milner, “The pathogenesis of burn wound conversion,” *Ann. Plast. Surg.*, vol. 59, no. 1, pp. 109–115, 2007.

[192] B. A. Harms, B. I. Bodai, G. C. Kramer, and R. H. Demling, “Microvascular fluid and protein flux in pulmonary and systemic circulations after thermal injury,” *Microvasc. Res.*, vol. 23, no. 1, pp. 77–86, 1982.

[193] R. R. Anderson and J. A. Parrish, “The Optics of Human Skin,” *J. Invest. Dermatol.*, vol. 77, no. 1, pp. 13–19, Jul. 1981.

[194] A. B. BJORNSON, H. S. BJORNSON, N. A. LINCOLN, and W. A. ALTEMEIER, “Relative roles of burn injury, wound colonization, and wound infection in induction of alterations of complement function in a guinea pig model of burn injury.,” *J. Trauma Acute Care Surg.*, vol. 24, no. 2, pp. 106–115, 1984.

[195] J. Yuan *et al.*, “Assessment of cooling on an acute scald burn injury in a porcine model,” *J. Burn Care Res.*, vol. 28, no. 3, pp. 514–520, 2007.

[196] T. A. Brans, R. P. Dutrieux, M. J. Hoekstra, R. W. Kreis, and J. S. Du Pont, “Histopathological evaluation of scalds and contact burns in the pig model,” *Burns*, vol. 20, pp. S48–S51, 1994.

[197] R. M. McFarlane, G. DeYoung, R. A. Henry, and R. M. McFarlane, “The design of a pedicle flap in the rat to study necrosis and its prevention.,” *Plast. Reconstr. Surg.*, vol. 35, no. 2, pp. 177–182, 1965.

[198] P. N. Manson, R. M. Anthenelli, M. J. Im, G. B. Bulkley, and J. E. Hoopes, “The role of oxygen-free radicals in ischemic tissue injury in island skin flaps.,” *Ann. Surg.*, vol. 198, no. 1, pp. 87–90, Jul. 1983.

[199] Y.-S. Jin, G.-J. Kim, and S.-G. Jeon, “Terahertz dielectric properties of polymers,” 2006.

[200] G. M. Gordillo and C. K. Sen, “Revisiting the essential role of oxygen in wound healing,” *Am. J. Surg.*, vol. 186, no. 3, pp. 259–263, Sep. 2003.

[201] “SKIN GRAFT SURVIVAL ON AVASCULAR DEFECTS. : Plastic and Reconstructive Surgery,” *LWW*. [Online]. Available:

http://journals.lww.com/plasreconsurg/Fulltext/1975/01000/SKIN_GRAFT_SURVIVAL_ON_AVASCULAR_DEFECTS_.10.aspx. [Accessed: 12-Jun-2016].

[202] J. Burge, “Essentials of Plastic Surgery – Second Edition. Edited by J. E. Janis. St. Louis, MO/Boca Raton, FL: PB - QMP/CRC Press , 2014. 1336 pages. Paperback. ISBN: 978-1-57626-385-3. Price: $AUD132.00.,” *ANZ J. Surg.*, vol. 84, no. 12, pp. 981–982, Dec. 2014.

[203] M. Attas, M. Hewko, J. Payette, T. Posthumus, M. Sowa, and H. Mantsch, “Visualization of cutaneous hemoglobin oxygenation and skin hydration using near-infrared spectroscopic imaging,” *Skin Res. Technol.*, vol. 7, no. 4, pp. 238–245, Nov. 2001.

[204] J. M. Converse, J. Smahel, J. Smahel, D. L. Ballantyne, and A. D. Harper, “Inosculation of vessels of skin graft and host bed: A fortuitous encounter,” *Br. J. Plast. Surg.*, vol. 28, no. 4, pp. 274–282, Oct. 1975.